Alma Mater Studiorum - Università di Bologna

in cotutela con Sorbonne Université

DOTTORATO DI RICERCA IN

MATEMATICA

Ciclo 35

Settore Concorsuale: 01/A3 - ANALISI MATEMATICA, PROBABILITÀ' E STATISTICA
MATEMATICA

Settore Scientifico Disciplinare: MAT/05 - ANALISI MATEMATICA

NEUROGEOMETRY OF REACHING

Presentata da: Caterina Mazzetti

Coordinatore Dottorato

Valeria Simoncini

Supervisore

Giovanna Citti

Supervisore

Alessandro Sarti

Esame finale anno 2023

UNIVERSITÀ DI BOLOGNA
SORBONNE UNIVERSITÉ

Dipartimento di Matematica (Università di Bologna)

et

École Doctorale 386 (Sorbonne Université), Unité de rattachement UM 8557
Centre d'analyse et de mathématique sociales (CAMS), EHESS (Paris)

Thèse pour obtenir le grade de
DOCTEUR

Discipline: Mathématiques appliquées

Présentée et soutenue par:
Caterina Mazzetti

NEUROGEOMETRY OF REACHING

Sous la direction de :

Giovanna Citti   DM, Bologne, Italie
Alessandro Sarti   CAMS (EHESS-CNRS), Paris, France

Abstract

The purpose of the thesis is to develop a model for the functional behaviour of neurons in the primary motor cortex (M1) responsible for arm reaching movements. From Georgopoulos neurophysiological data, we provide a first bundle structure compatible with the hypercolumnar organization and with the position-direction selectivity of motor cortical cells. We then extend this model to encode the direction of arm movement which varies in time, as experimentally measured by Hatsopoulos by introducing the notion of movement fragments. We provide a sub-Riemannian model which describes the time-dependent directional selectivity of cells though integral curves of the geometric structure we set up. The sub-Riemannian distance we define allows to implement a grouping algorithm able to detect a set of hand motor trajectories. These paths, identified by using a kernel defined in terms of kinematic variables, are compatible with the motor primitives obtained from neurophysiological results by spectral analysis applied directly on cortical variables. In a second part of the work, we propose geodesics in this space as an alternative model of models for arm movement trajectories. We define a special class of curves, called admissible, on which to study the geodesics problem: we provide a connectivity property in terms of admissible paths and the existence of normal length minimizers. Admissible geodesics are used as a model of reaching paths, finding a first validation through Flash and Hogan minimizing trajectories.

Résumé

L'objectif de la thèse est de développer un modèle pour le comportement fonctionnel des neurones du cortex moteur primaire (M1) responsables des mouvements d'atteinte du bras. A partir des données neurophysiologiques de Georgopoulos, nous fournissons une première structure de fibré compatible avec l'organisation en hypercolonnes et avec la sélectivité position-direction des cellules corticales. Nous étendons ensuite ce modèle pour encoder la direction du mouvement du bras qui varie dans le temps, comme mesuré expérimentalement par Hatsopoulos en introduisant la notion de fragments de mouvement. Nous fournissons un modèle sous-riemannien décrivant la sélectivité directionnelle des cellules en fonction du temps via des courbes intégrales de la structure géométrique que nous avons développée. La distance sous-riemannienne que nous définissons permet ensuite d'implémenter un algorithme de clustering capable d'identifier un ensemble de trajectoires de mouvements du bras. Ces trajectoires, identifiées à l'aide d'un kernel défini en termes de variables cinématiques, s'avèrent compatibles avec les états de cohérence de groupes de neurones détectés par des données neurophysiologiques. Ces derniers sont représentés par des séquences de trajectoires obtenues au moyen d'un modèle d'analyse en composantes principales appliqué directement à l'activité neuronale. Dans une seconde partie du travail, nous proposons une classe des géodésiques dans cet espace comme un modèle alternatif de modèles pour les trajectoires des mouvements du bras. Nous définissons une classe spéciale de courbes, dites admissibles, sur lesquelles étudier le problème des géodésiques: nous fournissons une propriété de connectivité en termes de chemins admissibles et l'existence de minimiseurs de longueur normale. Les géodésiques admissibles sont utilisées comme modèle de trajectoires d'atteinte, trouvant une première validation à travers les trajectoires minimisant du Flash et Hogan.

Introduction

The objective of the thesis is to study a model for the functioning of motor cortical cells responsible for arm reaching movements. The model relies on empirical data existing literature and gets inspiration from existing models of the visual cortex (e.g. [42], [131], [130]). Our model focuses on the major areas responsible for controlling arm reaching movements, mainly the arm area of the primary motor cortex (M1) and the premotor area.

The work is essentially composed of two main parts. The first part introduces a model of the motor cortex expressed via sub-Riemannian geometry. In the second part, trajectories of movements are modelled as geodesics in this space.

A fundamental problem regarding the study of motor cortex deals with the information conveyed by the discharge pattern of motor cortical cells. This is a quite difficult topic if we compare it to sensory areas, indeed, for any specific sensory stimulus, there are many inputs captured by photoreceptors and one output signal processed in the cortex. In the motor system the flow of information is intricate, as inputs come from basal ganglia, cerebellum and fronto-parietal cortex and there are as many output signals directed to interneurons and motorneurons of the spinal cord ([157], [32], [52]). Moreover, unlike the sensory areas, in the motor system the existence of a notion of receptive profiles, or in this case, of "actuator profiles", is not established nor well understood. Nevertheless, it is recognized that the cortex, including the motor area itself, has a modular structure (see [89], [54], [118], [68]) and whose constituent modules, linked together simultaneously or in series in time, are considered to be responsible for the broad domain of voluntary movements ([59], [119]). With regard to the arm area of primates motor cortex, several studies reveal how neuronal activity involves the processing of the spatial-motor information (see for example [137], [71], [100], [31]). Starting from 1978, a pioneering work has been developed by A. Georgopoulos, whose experiments allow to recognize at least two main features of the arm area functional architecture. First, he discovered that cells of this area are sensible to the position and direction of the hand movement (see [64, 100] and [70, 137]): cells response is maximal when hand position and direction coincide with a position and direction, characteristic of the cell. Secondly, the columnar structure, which organizes motor cortical cells in columns corresponding to movement

directions (see [72], [7], [68]). After the work of Georgopoulos, other experiments proved that activity of neurons in the primary motor cortex correlates with a broader variety of movement-related variables, including endpoint position, velocity, acceleration (see for example [100], [116], [136]), as well as joint angles (see [6], [146]), endpoint force [69], muscle tensions ([54], [147], [85]). It is also proved that the tuning for movement parameters is not static, but varies with time ([11], [116], [38], [125]) and for this reason Hatsopoulos et al. ([81, 133]) argue that individual motor cortical cells rather encode "movement fragments", i.e. movement trajectories.

Aim of the first part of the thesis is to propose a model inspired by the functional architecture of the arm area of M1 referred to a set of cortical tuning parameters in response to point-to-point reaching movements. We will start with a static model expressing the A. Georgopoulos' data of directional selectivity and columnar organization. We propose a first fiber bundle structure compatible with the hypercolumnar organization of directionally tuned cells: to every point on the cortical surface coding for hand's position in the plane $(x, y) \in \mathbb{R}^2$ is associated a full fiber of possible movement directions. As a result, a motor neuron can be represented by a point $(x, y, \theta) \in \mathbb{R}^2 \times S^1$, where (x, y) denotes hand's position in a two dimensional plane and θ denotes a movement direction at position (x, y). The directional selectivity of motor cortical cells induces the vanishing of the one-form

$$\omega = -\sin\theta dx + \cos\theta dy \qquad (1)$$

over the tangent bundle of $\mathbb{R}^2 \times S^1$. The contact form (1) induces a sub-Riemannian geometry whose horizontal space is the kernel of ω. Here, there is a remarkable analogy between the structure of external features selected by the neurons in this area and the the ones in the primary visual cortex (V1): both are characterized by the presence of a hypercolumnar structure coding for position and orientation (see [90, 87]). We also refer to differential models of these structures, starting with Hoffmann [83], Petitot and Tondut [131], Bressloff and Cowan [27], Citti and Sarti [41], just to name a few of the main ones.

In addition to hand's position (x, y) and hand's movement direction $\theta \in S^1$, motor cortical cells are selective of kinematic parameters evolving over time t, including hand's speed and acceleration, denoted by (v, a) ([65, 100], [11], [116], [136], [154], [150], [81, 133]). All of these variables give rise to the features space

$$\mathcal{M} = \mathbb{R}^3_{(x,y,t)} \times S^1_\theta \times \mathbb{R}^2_{(v,a)}. \qquad (2)$$

The choice of these variables and their differential constraints induce to consider the following one-forms

$$\omega_1 = \cos\theta dx + \sin\theta dy - vdt, \quad \omega_2 = -\sin\theta dx + \cos\theta dy, \quad \omega_3 = dv - adt. \qquad (3)$$

We denote by $D^{\mathcal{M}}$ the horizontal distribution belonging to the kernel of the above 1-

forms. The vector fields generators of $D^{\mathcal{M}}$ are given by

$$X_1 = v\cos\theta\frac{\partial}{\partial x} + v\sin\theta\frac{\partial}{\partial y} + a\frac{\partial}{\partial v} + \frac{\partial}{\partial t}, \quad X_2 = \frac{\partial}{\partial\theta}, \quad X_3 = \frac{\partial}{\partial a} \tag{4}$$

with the metric which makes them orthonormal. In this model, we describe the cortical selectivity of movement-related variables through integral curves of the sub-Riemannian space $\mathcal{M}$, in agreement with the coding of time dependent movement fragments experimentally measured by Hatsopoulos et al. [81] and Churchland and Shenoy [38]. We also compare our model with the area of V1 responsible for movement coding, which exhibits analogous time-dependent receptive profiles [43].

We then validate the model as follows. We define the connectivity kernel

$$\omega_{\mathcal{M}}\left(\eta_i, \eta_j\right) = e^{-d^{\mathcal{M}}(\eta_i,\eta_j)^2}, \tag{5}$$

where $(\eta_i, \eta_j) \in \mathcal{M}$ and $d^{\mathcal{M}}$ is the sub-Riemannian metric of the space. Equation (5) is an estimate of the heat kernel, and we propose it as a model of the local connectivity between the cortical tuning points η_i and η_j. We use this kernel, expressed in terms of kinematic variables, and a spectral clustering algorithm to detect a set of hand trajectories. These resulting paths are well in accordance with the ones obtained by Hatsopoulos et al. [81] and by Kadmon Harpaz et al. [95] with a clustering algorithm applied directly on cortical variables.

In the second part of our work, we study a model for arm reaching movements inspired by phenomenological models of movement planning. The natural idea is to exploit the sub-Riemannian metrics previously set up and look at geodesic models for arm movement trajectories. The primary motor cortex is in fact one of the main brain areas involved in voluntary movements, nevertheless the question on how the central nervous system selects one specific trajectory of movement is not fully understood (we refer to [77], [138] [96], [80], [124] for a general analysis of the problem). E. Todorov [148] argued that, among all possible movements, the brain selects those that meet appropriate optimality criteria. Currently, many models for goal-directed movements are based on optimality principles, so that movements are selected to minimize a particular cost function (see [84], [60], [152], [99], [57], [18], [16] and [61] as a review). One of the best-known model is the minimum hand jerk criteria, developed by Flash and Hogan [60]. The cost function to be minimized is the square of the rate of change of hand acceleration integrated over the movement execution time:

$$\frac{1}{2}\int_0^T \left(\dddot{x}^2 + \dddot{y}^2\right) dt, \tag{6}$$

where x and y are the time-varying hand positions in a Cartesian coordinate system. Finding the minimum of the functional (6) is equivalent to assuming that one of the main goals of reaching tasks is to produce the smoothest possible hand motion. The model produces horizontal arm movements that globally fit well with experimental data and

with the invariant patterns found in [2, 117]. Many phenomenological models have been developed by inferring the cost function from behavioural data (see [9], [10], [16],[12], [33], [91], [34]). The approach followed in these articles is the setting of a nonholonomic sub-Riemannian control system (see F. Jean's book [92] for a complete overview of sub-Riemannian geometry and its applications to motion planning problems). Similar instruments have been applied also for visual areas ([22], [21], [20], [50], [62]): illusory contours and perceived curves elaborated in the cortical areas V1/V2 have been described as geodesics of the neurogeometrical model of Petitot-Citti-Sarti [128], [41]. Geodesics are minima of the length functional in the set of curves with fixed extrema. Their existence in sub-Riemannian setting is a well known fact (see Chow's Theorem [36]), however they present properties completely different from the Riemannian ones, due to the existence of abnormal geodesics (see [114]). Extensive literature is devoted to the study of geodesics in the sub-Riemannian setting, we mention the work of Beals, Gaveau and Greiner who solved the geodesic problem with explicit formulas for the Heisenberg group [13], the works of Sachkov and Moiseev [110] and of Duits et al. [51] for geodesics in the group of motions of a plane $SE(2)$ and within $SE(d)$, Ardentov and Sachkov [8] for geodesics in the Engel group and Bravo-Doddoli and Montgomery [25] for geodesics in jet space. Abnormal geodesics are isolated geodesics that do not satisfy the differential equation canonically associated with the geodesic variational problem ([114, 111], [29], [144], [19], [115], [35]). Montgomery first provided an example showing the existence of such abnormal minimizers ([111, 112]), also called as singular in this case. For distribution of rank 2, Liu and Sussmann [108] introduced a class of abnormal extremals which are always locally length minimizing (see also [29] for the rigidity phenomena of singular curves). Engel manifolds [113], which are 4-dimensional manifold together with a rank-2 distribution of growth $(2, 3, 4)$, are foliated by abnormal geodesics [144] (see also the works [8], [17], [25] for a deepened study of geodesics in Engel group).

The purpose of the second part of our work is to propose a model of reaching via sub-Riemannian geodesics inspired by the minimum-jerk model (6) and by a model of functional architecture of the arm area of primary motor cortex M1. The energy functional defined by Flash and Hogan (6) can be expressed as a first-order functional in the space $\mathcal{J}^2 = \mathcal{J}^2(\mathbb{R}, \mathbb{R})$ of 2-jets. Geodesics in distributions of rank 2 have been extensively studied (see e.g. the works [108], [8], [17]), but the space $(\mathcal{M}, D^{\mathcal{M}}, \langle \cdot, \cdot \rangle_g)$ introduced in the first part of the thesis contains the $\mathcal{J}^2$ space as a subgroup. Therefore, we study the length functional in this space $\mathcal{M}$, whose restriction to the $\mathcal{J}^2$ space reduces to the expression of the functional (6) in the $\mathcal{J}^2$ space. We define a special class of curves, named as admissible, on which to study the geodesics problem. Since Hörmander condition is no more guaranteed for admissible curves, we prove a connectivity property and the existence of a minimum path joining two arbitrary points of the space in terms of admissible curves. Finally, we prove that admissible geodesics are regular (in the sense of Definition 5.2 of [40], from [86]). To prove this result, we exploit the holonomy

map introduced by Hsu [86] and the variational formulas for horizontal curves in graded manifolds (we mainly refer to [74] and [40]). The regularity of admissible geodesics implies that they are normal [114], so that they can be actually found as solutions of the geodesics equations. We then presented a qualitative analysis of admissible geodesics, showing how admissible curves allow to represent a wide variety of task-related reaching movements.

The thesis is organized as follows. The first two chapters contain an overview of the existing literature. Namely, the first chapter contains an outline of the structure of the motor cortex, starting from neurophysiological data to phenomenological models of movement. The second chapter deals with the main mathematical instruments on which it is based our model. Chapter 3 describes our model for the functional architecture of motor cortical cells expressed via sub-Riemannian geometry. In Chapter 4 we perform a quantitative validation of the model comparing the proposed kernel with neurophysiological data of motor primitives. Finally, Chapter 5 presents a model for arm reaching trajectories as geodesics of the sub-Riemannian space.

Contents

Chapter 1

Neurophysiology and phenomenology of arm movements

The objective of this Chapter is to recall some of the main aspects of the neurophysiological and phenomenological literature of the arm area of motor cortex that will be relevant to the formulation of our model. We start by providing some background on the motor circuits, with a particular focus on the primary motor cortex. We will present the problem of neural coding, first highlighting the properties of individual neurons (see section 1.2), and then providing a more general perspective by including the activities of cell populations (see section 1.3).

1.1 The motor areas

Movement is the result of information processing by a complex organization of motor centers within the nervous system. There are four levels of motor control: the spinal cord, the brainstem, the motor cortex and the associative cortex [97], [32]. As can be seen in Figure 1.1, the hierarchy also contains two side loops: the basal ganglia and the cerebellum, which interact with the hierarchy through connections with the thalamus. In this way, the flow of information through the motor system has both a serial organization, which enables communication between levels, and a parallel organization, which consists of multiple pathways between each level. Damage to higher levels results in deficits in motor planning, initiation, coordination, and so forth, but movement is still possible. Because of the parallel nature of processing, paralysis is a relatively rare outcome, produced by damage to the lowest level of the hierarchy.

Descending motor pathways arise from multiple regions of the brain and send axons down the spinal cord that innervate alpha motor neurons, gamma motor neurons, and interneurons. The corticospinal tract is the main pathway for control of voluntary movement in humans and it is composed of over a million of fibers. The fibers descend
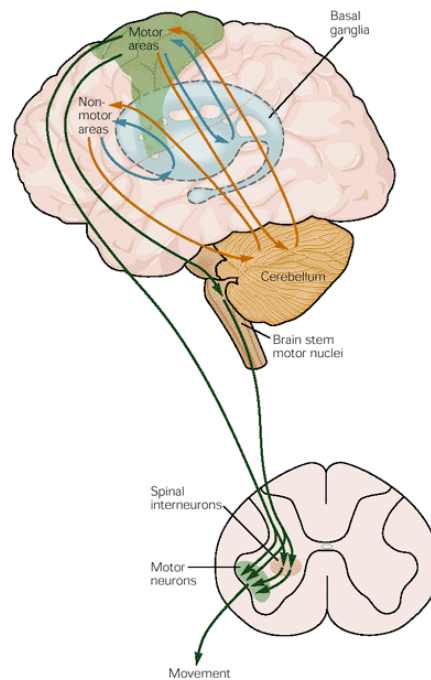
Figure 1.1: Schematic representation of motor circuits. Source: [97]

through the brainstem where the majority of them cross over to the opposite side of the body. After crossing, the fibers continue to descend through the spine, terminating at the appropriate spinal levels [79]. Voluntary movements require the participation of the motor cortex and the association cortex. These areas are involved in the strategy, the goal of the movement and the movement strategy that best achieves the goal, and in the tactics, i.e. the sequences of muscle contractions, arranged in space and time, required to smoothly and accurately achieve the strategic goal [14].

The motor cortex comprises three different areas of the frontal lobe: the primary motor cortex (Brodmann's area 4 or M1), the premotor cortex (PM), and the supplementary motor area (SMA). Figure 1.2 shows a schematic representation.

The primary motor cortex is located on the precentral gyrus and immediately anterior to the central sulcus. Of the three motor cortex areas, stimulation of the primary motor cortex requires the least amount of electrical current to elicit a movement. The premotor cortex sends axons to the primary motor cortex as well as to the spinal cord directly; it appears to be involved in the selection of appropriate motor plans for voluntary movements, whereas the primary motor cortex is involved in the execution of these voluntary movements. Anyway, a strict distinction between these areas seems quite difficult to analyze, moreover, the transition from premotor to primary motor cortex is gradual and it is object of discussion in [78]. The supplementary motor area is involved in programming complex sequences of movements and coordinating bilateral movements.
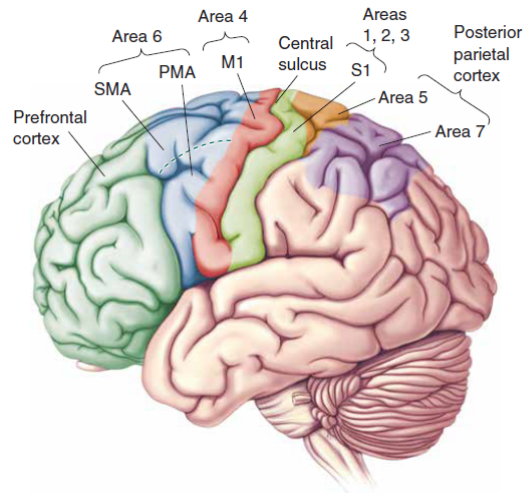
Figure 1.2: Principal cortical domains involved in the control of voluntary movement. Areas 4 and 6 form the motor cortex. Source: [14].

Whereas the premotor cortex appears to be involved in selecting motor programs based on visual stimuli or on abstract associations, the supplementary motor area appears to be involved in selecting movements based on remembered sequences of movements.

1.2 The problem of motor coding

1.2.1 Role of the movement direction information

A pioneering work in the study of motor cortex was developed by A. Georgopoulos. His experiments allowed to recognize that one of the key functions of the motor cortex consists on the control of the direction of movement trajectory (see [70, 137]). Neuronal activity was recorded and analyzed while monkeys moved their hands in uniformly distributed directions starting from the same point. These movements are called center-out tasks. The intensity of a single cell discharge varied with the direction of movement and it was highest for movements in a specific direction, called preferred direction (PD), and progressively decreased while moving in direction far from the PD (see Figure 1.3 as a reference). This single cell behaviour is modelled in [70, 137] through a sinusoidal function of the movement direction:

$$f(\theta) = b + k \cos(\theta - \theta_{\mathrm{PD}}), \tag{1.1}$$

where θ_{PD} represents the preferred direction of the cell, and the coefficient k denotes the increase in discharge over the overall mean b at the preferred direction θ_{PD}. Equation (1.1) is called directional tuning curve. Since PDs differed from different cells and a

(a)   (b)

Figure 1.3: (a) Variations in the frequency discharge of a motor cortical cell with the movement directions. Rasters represent the impulse activity during five repetitions of movements made in each of the eight directions indicated by the center diagram. Source: [70]. (b) Clusters repre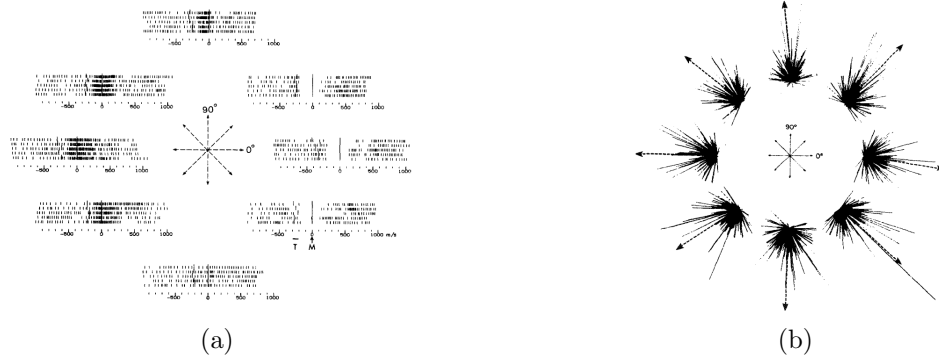sentation of the same cellular population with respect to eight movement directions in 2D space. The neuronal population vector (broken arrow) points approximately in the direction of the movement. Source: [67].

large proportion of arm-related cells were active during reaching movements, it was hypothesized that the specification of a movement direction in space were due to the engagement of a population of cells activity. Indeed, Georgopoulos et al. ([67], [71]) proposed to estimate the direction of movement via a weighted vectorial sum of cells PDs

$$P\left(\theta\right) = \sum_{i=1}^{N} \theta_{\mathrm{PD}}^{i}\, w_i\left(\theta\right),$$ (1.2)

where N is the number of cells in the population and w_i is a symmetric function with respect to the preferred direction θ_{PD}^{i} of the i-th cell. It was found that the sum (1.2), called neuronal population vector [73], approximates the direction of movement not only during movement execution, but even before the movement start. Best predictions for the upcoming direction of movement (see Table 2 of [71]) were made with weights of the form

$$w_{\theta_{\mathrm{PD}}}\left(\theta\right) = \left(f\left(\theta\right) - b\right)/k = \cos\left(\theta - \theta_{\mathrm{PD}}\right).$$ (1.3)

Furthermore, two central articles published in 1984 [64] and 1988 [100] focused on how motor cortical cells activity was also related with the position at which the hand is actively maintained in space, supporting the importance of the arm area of motor cortex in the coding of the spatial-motor information. In [64] a positional gradient tuning curve was presented as

$$g\left(x, y\right) = b + \alpha x + \beta y,$$ (1.4)

where the value of $g\left(x, y\right)$ denotes cell's discharge rate at position $\left(x, y\right)$ with respect to

an origin located at the central button of the center-out reaching apparatus; the quantity b is the discharge rate in the origin and α, β are expressions of the slopes of cell discharge per unit length along the x and y axes of the plane.

1.2.1.1   Columnar organization

The first studies regarding the anatomical columnar organization of the neocortex are due to Mountcastle [118]. Inspired by these results, Georgopoulos [68] proved the existence of a functional columnar organization also for the arm area of motor cortex (see Figure 1.4 and 1.5). Precisely the movement PD of cells is approximatively constant for a penetration parallel to anatomical cortical columns and varies in the perpendicular direction [63].

(a)   (b)
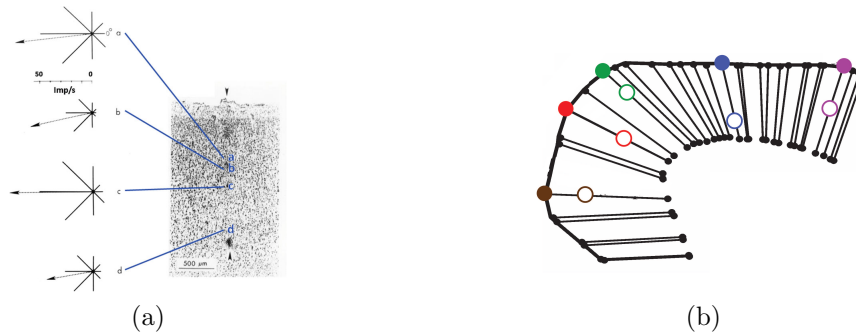
Figure 1.4: (a) Movement direction selectivity of four neurons recorded along the histologically identified penetration. The similarity of preferred directions for a penetration parallel to the cortical columns is shown. Source: [68]. (b) Schematic illustration of the projection of recording sites onto the cortical surface along anatomical columns. Open and slashed circles denote recording and projected sites, respectively. Source: [72].

In [7], [122] and [72], the authors clarified that cells PDs arrangement had a periodic structure (see Figure 1.5). More precisely, it was recorded a continuum of 500 μm in depth with cells of similar preferred directions and it was measured a repeating columnar pattern of similar PDs with a width of 50 to 100 μm and a repetition distance of almost 200 μm (see Figure 1.5a for a schematic representation). A fundamental aspect of the above organization is that within each hypercolumn (i.e. assemblage of columns) of radius 120 μm, the diversity of cells PDs was sufficient to represent any given direction of reach ([122, 72]).

1.2.1.2   Heterogeneity of movement parameters

Subsequent proved that the arm area of the motor cortex is related to a more complex and heterogeneous set of movement variables (see [96], [139] for a general review). John

(a)   (b)

Figure 1.5: (a) Schematic lattice model of the repeated, regular mapping of the preferred directions in motor cortex. Adapted from [72]. (b) Motor cortical map of preferred directions: each color denotes a cell's PD within the unit circle. Image adapted from [122].

F. Kalaska in [96] pointed out that the primary motor cortex acts as a controller that specifies a particular parameter of the desired output. Then, the descending output from M1 translates such a command signal into the resulting motor response. A fundamental class is formed by "extrinsic" 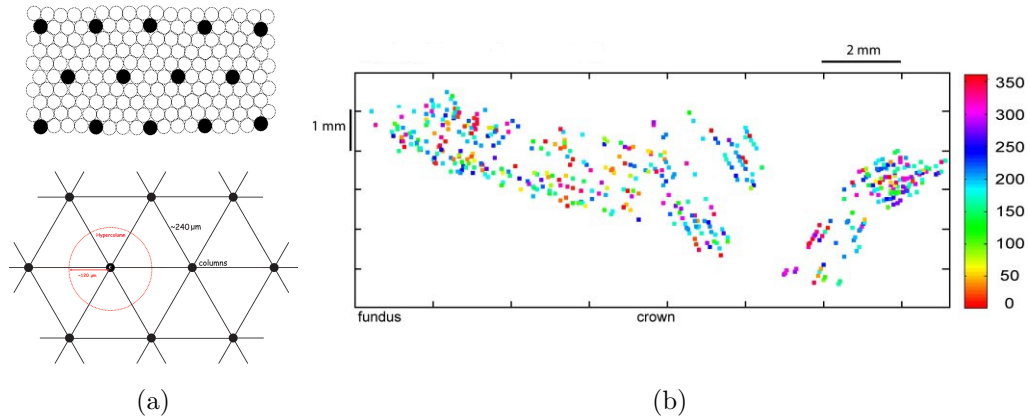or "hand-centered" parameters which typically describe cortical activity with respect to hand's movement. These variables mainly refer to endpoint position, velocity and acceleration of the hand both in two-dimensional and three-dimensional space (see [11], [64], [100],[116], [143]), in addition to the movement direction variable. This class of parameters has been broadly used for the characterization of the spatio-temporal form of movement (see for example the work of Flash and Hogan [60] and [58], [84]). There also exists a class of movement parameters which relates cells activity to an "intrinsic" corporeal frame of reference, which can be for example "joint-centered" or "muscle-centered" and which enables to describe cortical activity with respect to events occurring at specific parts of a limb. These variables often concern the dynamic aspects of movement or its causal forces, such as muscle tensions or force limbs (see for example [141], [140], [147]).

Nevertheless, there is experimental evidence indicating some functional properties of neurons across M1: cells activity recorded in the rostral part of primary motor cortex appears to be more related to kinematic variables , whereas neural activity recorded caudally on the precentral gyrus is thought to correlate with the temporal pattern of force production and motor output (see [145], [81] and [96]). We specify that our work will be focused on a space of kinematic parameters whose relation with cortical activity is assumed to be well verified (see for instance [136]) and from which we will formulate a neurogeometric model for the description of motor cortical cells organization.

1.2.2   The coding of movement fragments

A seminal work of Graziano in 2002 [77] showed that complex and coordinated time-evolving movements can be elicited by electrical stimulation even of a single neuron of the motor cortex. Hence, beyond the wide spectrum of parameters that are encoded within the motor cortex, there exists also a temporal dimension to which each neuron results to be sensitive with respect to motor information ([11], [116], [125], [38],[133, 81]).

In particular, Hatsopolous [81] (see also [133]) highlighted that tuning to movement parameters varies with time and proposed to describe the activity of neurons through a trajectory encoding model. In his model, the probability of spiking of a neuron is expressed as the exponential of the inner product between the "preferred velocity trajectory" $\vec{k}$ and the normalized velocity trajectory of the hand $\vec{v}^{t_0}$ of duration 400 ms, as follows

$$p\left(\text{spike}\,(t_0)\,|\vec{v}^{t_0}\right) = \exp\left(\vec{k}^{t_0} \cdot \vec{v}^{t_0} + \gamma^{t_0}\right). \tag{1.5}$$

The vector $\vec{k}$ is named as "preferred velocity" since it maximizes the spike probability when it is aligned to $\hat{v}^{t_0}$, whereas the parameter γ is an offset parameter of the model. Note how for fixed instant of time t_0 equation (1.5) reduces to equation (1.1) of Georgopolous model. Indeed if $k = |k|\cos\theta_{\text{PD}}$, $v = |v|\cos\theta$, then

$$k \cdot v + \gamma = |k|\,|v|\cos(\theta - \theta_{\text{PD}}) + \gamma.$$

Consequently the argument of the exponential in equation (1.5) is exactly the function f in (1.1). The main difference is that now the same expression is considered at different instants of time t_0. In addition, equation (1.5) evaluates the output of a single cell in response to a trajectory fragment as the probability of spiking a neuron. The preferred path of the neuron is then obtained by integrating $\vec{k}$ over a time window which precedes and follows the spike time t_0. In the same work, it is also provided an extension to (1.5) by including the average speed $\bar{v}^{t_0}$, and average position $(\bar{x}^{t_0}, \bar{y}^{t_0})$ of the hand trajectory:

$$p\left(\text{spike}\,(t_0)\,|\vec{v}^{t_0}, \bar{v}^{t_0}, \bar{x}^{t_0}, \bar{y}^{t_0}\right) = \exp\left(\vec{k}^{t_0} \cdot \vec{v}^{t_0} + a\bar{v}^{t_0} + b\bar{x}^{t_0} + c\bar{y}^{t_0} + \gamma^{t_0}\right). \tag{1.6}$$

Overall, Hatsopoulos [81] argues that M1 neurons are selective to a preferred "movement fragment": a short trajectory describing a combination of parameters evolving in time (see also [133] and [124]). Figure 1.6a (from [81]) shows the temporal evolution of preferred directions for two neurons where each direction of movement (being an unit vector in $\mathbb{R}^2$) is represented by an angle in polar coordinates. Hence, in [81], the temporal behaviour of directionally tuned cells is represented by a function

$$t \mapsto (\cos(\theta(t)), \sin(\theta(t))) \in \mathbb{R}^2. \tag{1.7}$$

At the bottom of Figure 1.6a, vectors of preferred directions are added together giving rise to the movement fragment.

Churchland and Shenoy [38] proposed an analogous model which describes the temporal properties of motor cortical responses. Figure 1.6b displays the temporal variation of the preferred directions of twelve M1 neurons during an instructed center-out reaching task. In this paper, each direction of movement is expressed as a graph over a temporal interval, as follows

$$t \mapsto \theta\left(t\right) \in \mathbb{R}. \tag{1.8}$$

Through different representations of movement direction tuning, Hatsopoulos [81] and Churchland and Shenoy [38] stressed the importance of time dependence on cell sensitivity. In addition, both groups exploit a principal component analysis on a space of trajectory templates allowing a finite dimensional basis over the heterogeneity of neuronal patterns. In other words, even though neurons in M1 encode elementary movements, thank to the intrinsic connectivity of the cortex, they can generate the rich variety of complex motor behaviours.

In this thesis, we will provide a model able to describe the temporal dependence of the selective tuning of motor cortical cells with a finite number of kinematic variables. The differential constraints which relate these variables will be fundamental to give the structure of the space.

1.3   Neural states and movement output

Until now we have provided an overview of the properties of individual neurons in response to movement. Below we report the results of the work of Kadmon Harpaz et al. [95] which analyzes the structure of the output of reaching movements in relation to the dynamics of a cell population. The study showed that the neural activity reveals coherent patterns represented in terms of movement trajectories, similar to the response properties of individual neurons.

1.3.1   Movement decomposition in the primary motor cortex

In 2019, N. Kadmon Harpaz, D. Ungarish, N. Hatsopoulos and T. Flash [95] studied the activity of neural populations in the primary motor cortex of macaque monkeys during the performance of a random-target pursuit (RTP) task and a center-out reaching task.

The authors processed neural activity by identifying sequences of coherent behaviours, called neural states, by means of a Hidden Markov model, i.e. a model which describes a system transitioning between distinct states, related by a Markov process. The states are hidden and can only be observed through the observations that are a probabilistic process of the hidden states. In this article, the recorded spike trains are observations, dependent on the hidden states that are assumed to reflect global changes in cortical activity.
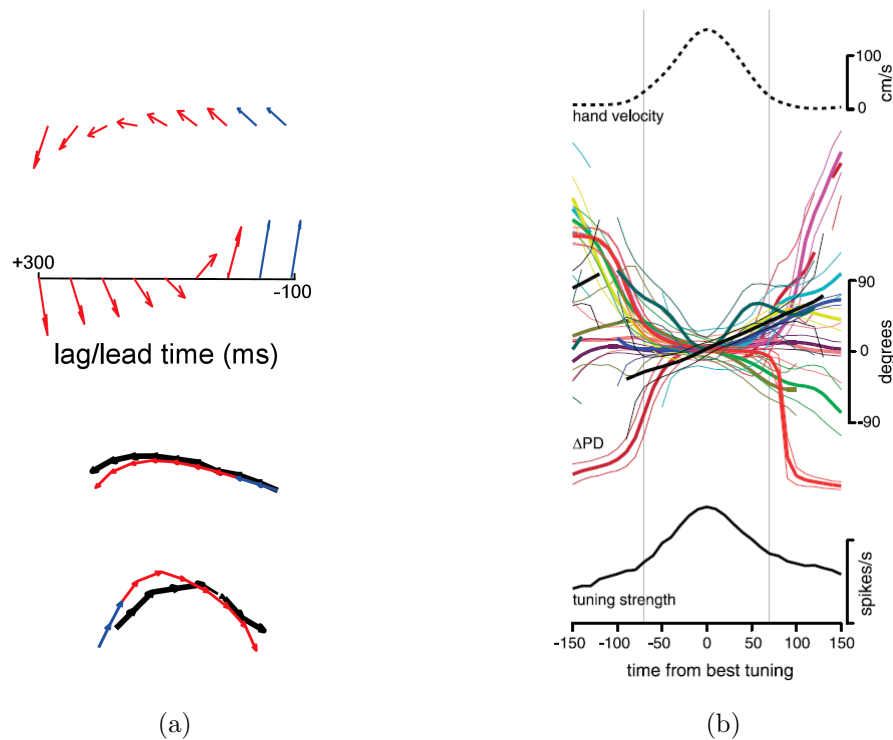
Figure 1.6: Temporal evolution of cells PDs through different representations. (a) Red and blue arrows show the encoded PDs for movements before and after the measured neuron firing rate, respectively. Below, the vectors of preferred directions added together give rise to the preferred trajectories. The black directional paths show the similarity of the encoded trajectories computed during a different task. Image adapted from [81]. (b) In the middle, change in PD expressed as continuous graphs for twelve M1 neurons. Below is shown the mean strength of direction tuning, where time 0 is assumed to be the strongest tuning instant. Above is represented the mean hand velocity profile whose peak is aligned at time $t = 0$. Image adapted from [38].

The neural states identified were found to be associated with motion trajectories, coinciding with acceleration and deceleration phases with directional selectivity of the entire reaching movement (see Figure 1.10). Trying to be clear, the following are some key points of their analysis.

1. During center-out reaching movements, two neural states (color-coded in Figure 1.7) emerge by decomposing the bell-shaped speed profile at the maximum of the tangential velocity.
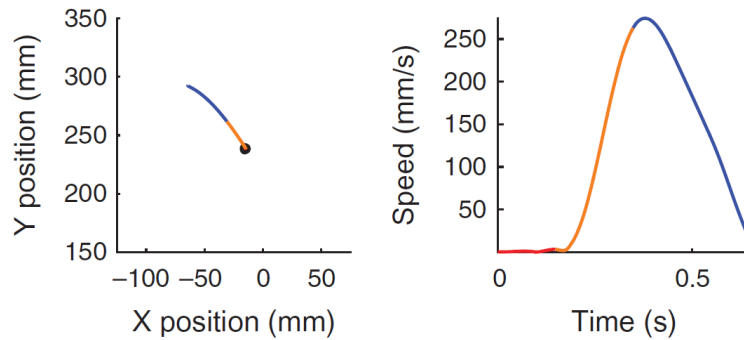
Figure 1.7: Examples of a center-out task, with position (left) and speed profile (right) colored according to the identified neural states. Black dot represents the starting position [95].

2. During consecutive reaching tasks (displayed in Figures 1.8 and 1.9), each neural state was associated with either accelerating or decelerating movement segments executed towards a certain direction within the workspace. The obtained neural states did not show selectivity to movement speed and amplitude (see in particular Figure 1.8).

3. Transitions between neural states (color-coded in Figures 1.7, 1.8, 1.9) systematically coincided with minima and maxima points of the tangential velocity of the end-effector, decomposing the movement into accelerating and decelerating phases (see Figure 1.9).

Recently, studies of neural dynamics in the primate parietal cortex during arm movements revealed three main states temporally coupled to the planning, execution and target holding epochs and, strikingly, execution was subdivided into distinct, arm acceleration- and deceleration-related, states [49].

We stress that the observed segmentations in M1 were not directly predicted by previously proposed models of kinematic parameters, such as for example the one of Georgopoulos (see eq. (1.1)). Precisely, the authors tested six models that included
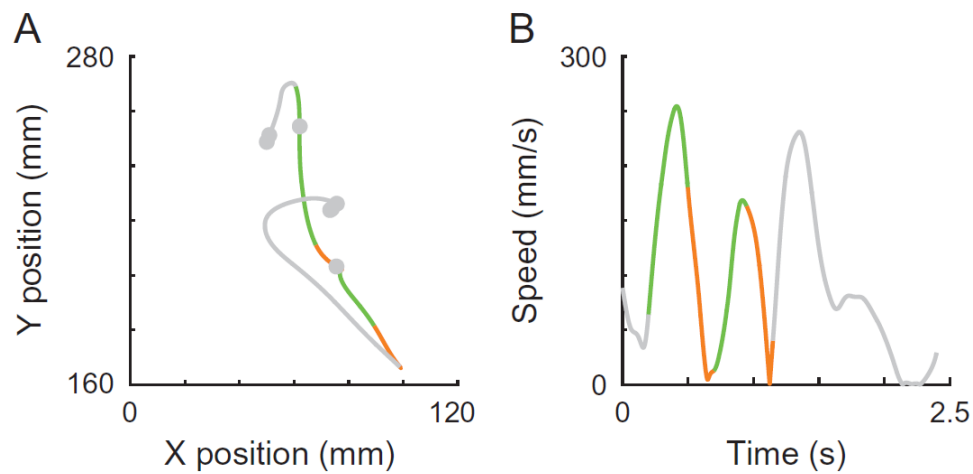
Figure 1.8: Invariance of neural states to movement speed and amplitude [95].
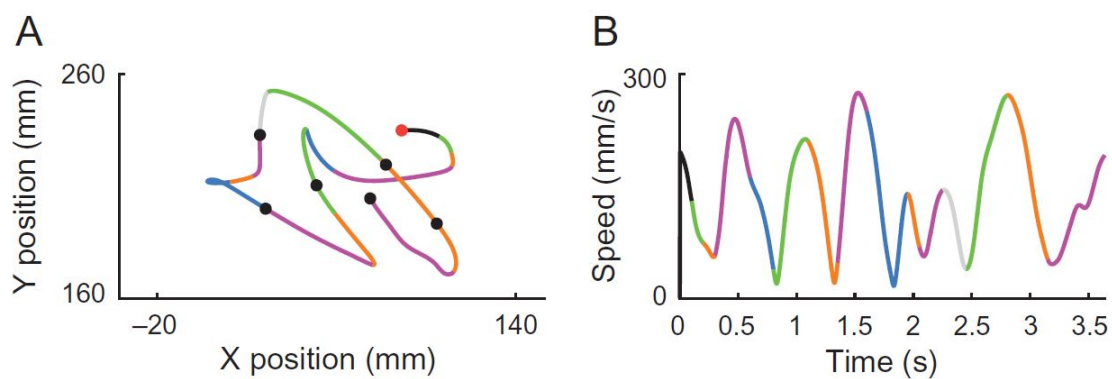
Figure 1.9: (A) Position data of a RTP task segmented and colored according to the decoded neural states. Each color represents a single state. (B) Corresponding speed profiles, colored as in A. Filled circles represent the target locations, first target is colored in red. Image taken from [95].

tuning for: movement direction; movement direction gain modulated by speed; direction of the acceleration vector; direction of the acceleration vector gain modulated by the magnitude of the acceleration vector; both movement direction and direction of the acceleration vector; or both movement direction and direction of the acceleration vector, each gain modulated by the magnitude of the corresponding vector:

$$fr_i(t - \tau) = B_{0_i} + B_{1_i} \cos(\theta(t) - \theta_{\mathrm{PD}_i}); \tag{1.9}$$

$$fr_i(t - \tau) = B_{0_i} + B_{1_i} \|\vec{v}(t)\| \cos(\theta(t) - \theta_{\mathrm{PD}_i}); \tag{1.10}$$

$$fr_i(t - \tau) = B_{0_i} + B_{1_i} \cos\left(\theta_a(t) - \theta_{a_{\mathrm{PD}_i}}\right); \tag{1.11}$$

$$fr_i(t - \tau) = B_{0_i} + B_{1_i} \|\vec{a}(t)\| \cos\left(\theta_a(t) - \theta_{a_{\mathrm{PD}_i}}\right); \tag{1.12}$$

$$fr_i(t - \tau) = B_{0_i} + B_{1_i} \cos(\theta(t) - \theta_{\mathrm{PD}_i}) + B_{2_i} \cos\left(\theta_a(t) - \theta_{a_{\mathrm{PD}_i}}\right); \tag{1.13}$$

$$fr_i(t - \tau) = B_{0_i} + B_{1_i} \|\vec{v}(t)\| \cos(\theta(t) - \theta_{\mathrm{PD}_i}) + B_{2_i} \|\vec{a}(t)\| \cos\left(\theta_a(t) - \theta_{a_{\mathrm{PD}_i}}\right). \tag{1.14}$$

In the numbered list above (taken from [95]), fr_i denotes the instantaneous firing rate of neuron i, τ the time lag between neural activity and kinematic output (taken to be 100ms), B_{0_i} the baseline firing rate, B_{1_i} and B_{1_i} modulation depths, whereas $\|\vec{v}(t)\|$ and $\|\vec{a}(t)\|$ represent the magnitude of the velocity and acceleration vectors, respectively, θ and θ_a are the directions of the velocity and acceleration vectors, and θ_{PD} and $\theta_{a_{\mathrm{PD}}}$ are the preferred velocity and acceleration angles of neuron i. Nevertheless, the kinematic tuning models used were not found to be significant in explaining the observed decomposition, hence Kadmon Harpaz et al. [95] obtained a movement segmentation at the neural level, but failed to recover the same decomposition by using existing models that incorporated tuning kinematic variables.

In our thesis, in Chapters 3 and 4, we will provide a geometric structure which is in agreement with both neural models incorporating kinematic variables and both the above movement decomposition.

1.3.2   A topographic map of movements

Starting from 2000s, M.S.A. Graziano elaborated a very general perspective for the comprehension of the cortical control of movement. As we briefly mentioned in section 1.2.2, in 2002 [77] he discovered that electrical stimulation of the motor cortex caused monkeys to make coordinated, complex movements. The obtained results led him to reconsider the traditional nature of the body map arranged across the cortical surface. Indeed, he found that motor cortex topographic organization (see [4] and [76]) not only included a somatotopic map of the body, but also a map of hand location in space and a map of relevant actions. In particular, the last type of mapping revealed a partitioning
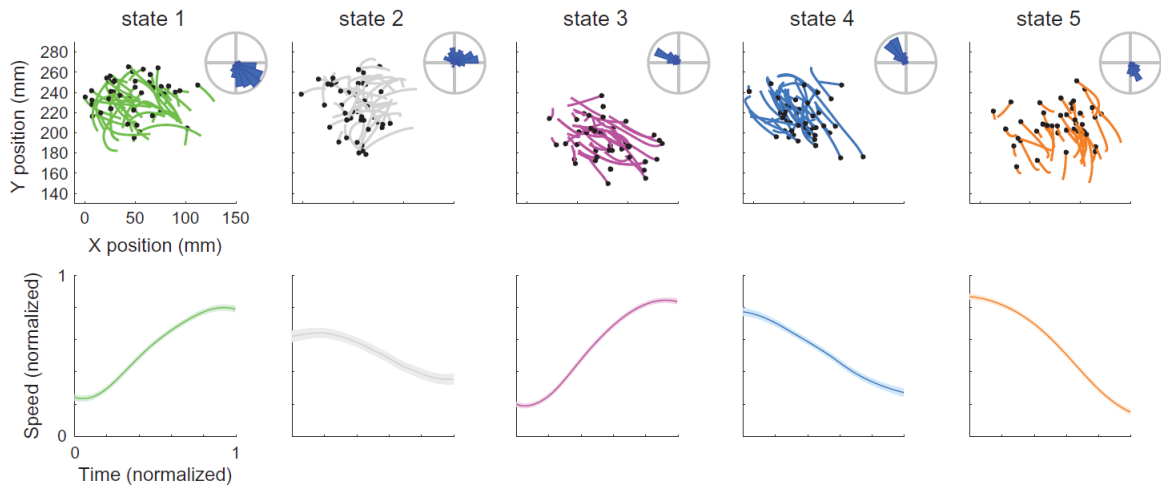
Figure 1.10: Directional and acceleration selectivity of neural states in the RTP task. Each column shows the position and normalized speed profiles of movement trajectories corresponding to each of the neural states. Radial histograms show the mean directions of all the trajectories within each state. Source: [95].

of regions dealing with different complex, ethologically relevant movements. This means that the motor cortex organization reflects the complexity of a movement related to a specific task. In Figure 1.11 (from [76]) we showed hand and arm representation and a scheme of behavioural actions mapped into the motor cortex area. For the somatotopic map of hand and arm, warm colors correspond to map locations in which the body part is more strongly represented. Note how the hand and arm somatotopic maps overlap in the reaching zone of action categories.

We point out that Graziano's research allowed to extend previous neurophysiological results, not to contrast them. In agreement with Hatsopoulos, he proved [3] that tuning to a single movement parameter is too a simple model to account for the behaviour of motor cortical neurons (see also Figure 1.12). More in detail, he verified that given different tasks and different movement sets, different types of tuning are obtained. For example, it was analyzed how during free arm movements, when many movement parameters presumably contribute to the activity of neurons, the movement direction tuning made a vanishing small contribution. However, when movements where tested on a center-out task, directional tuning played a central role in the variation of neuronal activity, as it was found in Georgopoulos experiments (see section 1.2.1 and [70, 73]). Graziano also agreed with the work of E. Todorov [149], who claimed that the motor system adopts an optimal control method: the cortex optimizes the control of task-relevant parameters (see also [147] and [148] as a review). In this hypothesis, there is no single, preferred parameter used for all tasks, but instead the parameters being specified by the optimal
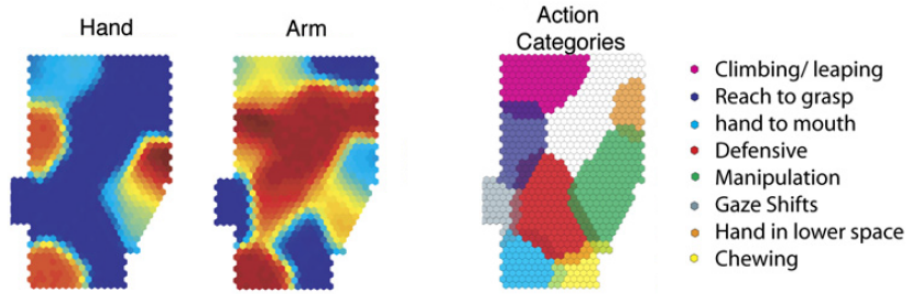
Figure 1.11: Overlapping motor cortical map organization. From left to right, somato-topic representation of hand and arm onto the surface and action categories map. Source: [76].

control strategy depend on the task being performed. As Scott reported in the review [138], a crucial objective for understanding motor function is to connect the three levels of the motor system: motor behaviour, limb mechanics and neural control. A very large literature is present for all three distinct aspects, beginning with the authors cited so far for neural models. In this thesis, for simplicity we will totally avoid the question of limb mechanics, but we will attempt to provide a geometrical interpretation of phenomelogical aspects of arm reaching movements, based on neural behaviour data.

1.4   Models of arm reaching movements

In this section, we give an overview on some mathematical models describing the phenomenology of arm movements. We briefly outline the model constructed by T. Flash and N. Hogan [60], which we will later recover as a special case of our model.

1.4.1   An overview

The motor cortex is one of the principal brain areas involved in voluntary movements, nevertheless the question on how the central nervous system selects one specific trajectory of movement is not fully understood (see [138] as a review). Movement planning and control strategies are indeed not directly measurable, yet the observation of certain invariant characteristics has provided many modelling insights on this topic (see also [77], [96], [80], [124] for a general analysis of the problem). For example, for two-dimensional arm reaching tasks, Abend et al. [2] and Morasso [117] found stereotypical patterns of movement based on straight paths and bell-shaped velocity profiles, suggesting that the central command for reaching gestures is formulated in terms of hand trajectories in space. More generally, E. Todorov [148] argued that, among all possible movements,
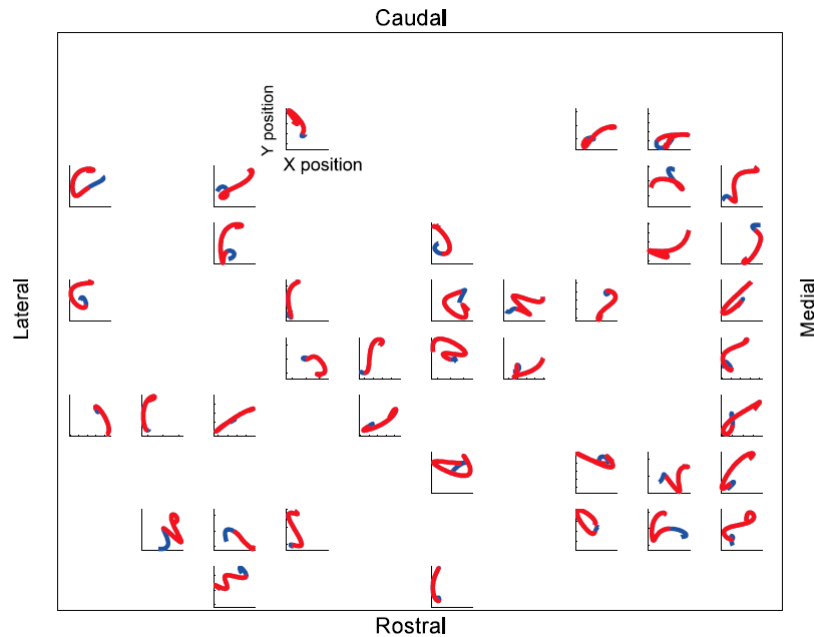
Figure 1.12: The map of movement fragments computed over a set of simultaneously recorded M1 neurons by a multielectrode array placement. From [81].

the brain selects those that meet appropriate optimality criteria. Currently, there is a wide variety of models of arm reaching trajectories based on optimality principles, so that movements are selected to minimize a particular cost function (see [84], [60], [152], [99], [57], [18], [16] and [61] as a review). One of the most well-known models in the field of movement planning is the minimum hand jerk criterion, which was developed by Flash and Hogan [60]. This model will be reviewed in the next section 1.4.2. The minimum hand jerk criterion proposes that during the execution of arm movements, the rate of change of acceleration of the hand should be minimized, resulting in smoother and more efficient movements. Shortly after this article, Uno, Kawato and Suzuki [152] proposed the minimum torque-change model, consisting of an objective function given by the square of the rate of change of torque generated by muscles. Here, the cost function depends on the nonlinear dynamics of the musculoskeletal system. In a model of 2007, Biess, Liebermann and Flash [18] defined geometric properties (path and posture) for three-dimensional pointing movements in terms of geodesic paths with respect to a kinetic energy in a Riemannian configuration space. In this setting, they were able to separately determine the geometrical and temporal movement features, allowing a unification of previous computational models. Although for the following cases the main modelling subject is human locomotion, many phenomenological models have been developed by inferring the cost function from behavioural data (see [9], [10], [16],[12], [33],

[91], [34]). The approach followed in these articles is the setting of a nonholonomic control system, whose underlying structure is defined in terms of sub-Riemannian geometry (see F. Jean's book [92] for a complete overview of sub-Riemannian geometry and its applications to motion planning problems). The authors showed the existence of optimal solutions, applied the Pontryagin maximum principle ([132]) to the control problem, and finally compared the minimizing trajectories with the experimental data. In the present work, following a procedure similar to [91], we will deduce an energy functional from neurophysiological data (see [136] as a review) and provide a phenomenological model of reaching arising from the sub-Riemannian geometry we set up.

1.4.2   The minimum jerk model

Flash and Hogan assume that movements are planned in terms of hand trajectories rather than joint rotations. Their model is expressed by finding a minimum of an energy function which takes into account the kinematic features of the motion: in moving from an initial to a final position in a given time T, the criterion function to be minimized is expressed by

$$\frac{1}{2} \int_0^T \left(\dddot{x}^2 + \dddot{y}^2 \right) dt, \tag{1.15}$$

where x and y represent the Cartesian coordinates of hand position. To find an extremum of the unconstrained cost function, they exploited Euler-Poisson equation whose resulting solution consists on a fifth order polynomial. They also applied Pontryagin maximum principle for defining the necessary conditions for a minimum to exist [132].
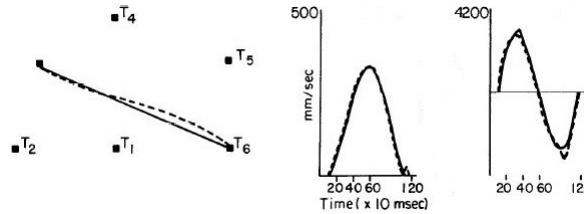
Figure 1.13: Representation example of hand paths, speed and acceleration for unconstrained point-to-point movement. Dashed lines are the kinematic movements measured. Source: [60].

Assuming that the motion begins and ends with zero velocity and acceleration, the minimum of (1.15) is given by

$$x(t) = x_0 + (x_T - x_0) \left(6\tau^5 - 15\tau^4 + 10\tau^3 \right), \quad y(t) = y_0 + (y_T - y_0) \left(6\tau^5 - 15\tau^4 + 10\tau^3 \right), \tag{1.16}$$

where (x_0, y_0) and (x_T, y_T) are the initial and final hand positions at $t = 0$ and $t = T$, and $\tau = \left(\frac{t}{T}\right)$.

The model produces straight paths and smooth symmetric velocity profiles that are in accordance with the experimentally observations made by Abend et al. [2] and Morasso [117] (see Figure 1.13 as an example). The solution trajectories depend only on the initial and final positions of the hand and movement time, therefore the optimal trajectory is determined only by the kinematics of the hand in the task-oriented coordinates and is independent of the physical system which generates the motion.

Chapter 2

Notions of Sub-Riemannian Geometry

In this Chapter we give the mathematical definitions and theorems required to develop our study (we refer to [94, 106] and [5, 114] for a general presentation of the topic).

2.1 Background

2.1.1 Fiber bundles

Definition 2.1. A *fiber bundle* is a structure (E, M, F, π), where:

- E and M are manifolds, called respectively *total space* and *base* of the fiber bundle;

- F can be a vector space or a group, called *fiber*;

- $\pi : E \to M$ is a smooth surjective map, called *projection*, such that, for all $p \in M$, the following properties hold:

  - $E_p := \pi^{-1}(p)$ is isomorphic to the set F, named as the fiber over p.
  - There exists a neighbourhood U of p in M and a diffeomorphism $\chi : \pi^{-1}(U) \to U \times F$ with the property that for every $q \in U$, $\chi_{|E_q} : E_q \to \{q\} \times F$ is an isomorphism. The map χ is called *local trivialization*.

If the fiber F constitutes a real vector space and the local trivialization is a bijective linear map, then the fiber bundle is called *vector bundle*.

By abuse of notation, sometimes the total space E is named as the *fiber bundle over M*.

Fiber bundles are by definition locally a product of bases and fibers, but globally they may have a more general structure.

Example 2.1. One of the most common example is the Möbius strip, which is a vector bundle of dimension 1 over the 1-sphere S^1. Locally, around every point in S^1, it looks like $U \times \mathbb{R}$, where U is an open arc including the point, but the total bundle is different from $S^1 \times \mathbb{R}$ (which is a cylinder instead).

The special case in which a fiber bundle is globally isomorphic to $M \times F$ is called *trivial*.

Definition 2.2. Let (E, M, F, π) be a fiber bundle. A *section* of E is a differential map $\sigma : M \to E$, such that $\pi \circ \sigma = id_M$.

Examples of vector bundles above are the tangent bundle TM and the cotangent bundle T^*M over the differentiable manifold M.

Definition 2.3. A section of the tangent bundle TM over M is called a *vector field* on M. A section of the tangent bundle T^*M over M is called a *1-form* on M.

2.1.2   Lie Algebras and Lie Groups

In this section we provide some basic definitions of the Lie group theory. All definitions can be found in standard mathematical textbooks (e.g. [94], [151] and [105]).

Definition 2.4. A *Lie algebra* (over $\mathbb{R}$) is a vector space $\mathfrak{b}$ equipped with a bilinear map $[\cdot, \cdot] : \mathfrak{b} \times \mathfrak{b} \to \mathfrak{b}$, the Lie bracket, satisfying:

1. $[X, Y] = -[Y, X]$, for all $X \in \mathfrak{b}$ (anti-commutativity);

2. $[[X, Y], Z] + [[Y, Z], X] + [[Z, X], Y] = 0$, for all $X, Y, Z \in \mathfrak{b}$ (Jacobi identity).

Lemma 2.1. *The space of vector fields $\Gamma(M)$ on a differentiable manifold M, equipped with the Lie bracket defined by*

$$[X, Y] = XY - YX, \text{ for all } X, Y \in \Gamma(M),$$

is a Lie Algebra.

Definition 2.5. If $\mathfrak{b}$ is a Lie algebra, a linear subspace $\mathfrak{a} \subset \mathfrak{b}$ is called a Lie subalgebra of $\mathfrak{b}$ if it is closed under Lie brackets.

A Lie subalgebra $\mathfrak{a}$ is itself a Lie algebra with the same bracket operation of the Lie algebra $\mathfrak{b}$.

Definition 2.6. A *Lie group G* is a differentiable manifold endowed with a group structure, such that the maps

$$G \times G \to G \quad \text{(multiplication)}$$
$$(g, h) \mapsto g \cdot h$$

and

$$G \to G \quad \text{(inverse)}$$
$$g \mapsto g^{-1}.$$

are smooth. If G and H are Lie groups, a *Lie group homomorphism* from G to H is a smooth map $F : G \to H$ that is also a group homomorphism.

Definition 2.7. A Lie group G *acts on a differentiable manifold M from the left* if there is a differentiable map

$$G \times M \to M$$
$$(g, x) \mapsto gx,$$

such that $g\,(hx) = (g \cdot h)\,x, \ \forall g, h \in G, \forall x \in M$. An action from the right is defined analogously.

Definition 2.8. Let G be a Lie group. For $g \in G$, we have the *left translation*

$$L_g : G \to G$$
$$h \mapsto g \cdot h$$

and the *right traslation*

$$R_g : G \to G$$
$$h \mapsto h \cdot g.$$

L_g and R_g are diffeomorphism of G, $(L_g)^{-1} = L_{g^{-1}}$.

Definition 2.9. A vector field X on a Lie group G is called *left invariant* if

$$L_{g*}\,(X_h) = X_{g \cdot h}, \text{ for all } g, h \in G.$$

Lemma 2.2. *Let G be a Lie Group, and let $\mathfrak{g}$ be the set of all left invariant vector fields on G. Then $\mathfrak{g}$ is a Lie subalgebra of $\Gamma\,(G)$.*

Definition 2.10. The Lie subalgebra $\mathfrak{g}$ of all left invariant vector fields is called the *Lie algebra of the Lie group G* and it is denoted by $\text{Lie}\,(G)$.

Theorem 2.3. *Let G be a Lie Group, and let $\mathfrak{g} = Lie\,(G)$. The evaluation map*

$$\mathfrak{g} \longrightarrow T_e G$$
$$X \longmapsto X_e$$

is a vector space isomorphism.

Therefore, for each Lie Group G finite dimensional, there is a finite dimensional Lie algebra intrinsically associated with it, with dimension equal to $\dim\,(G)$.

Definition 2.11. Let G be a Lie Group. A *one-parameter subgroup* of G is a Lie group homomorphism $F : \mathbb{R} \to G$.

There are one-to-one correspondences among

$$\{\text{one-parameter subgroups of } G\} \longleftrightarrow \text{Lie}\,(G) \longleftrightarrow T_e G$$

In particular, a one-parameter subgroup is uniquely determined by its initial tangent vector in $T_e G$. Let us recall the following definition (which is valid in general for manifolds, not only for Lie groups)

Definition 2.12. Fixed a point $g \in G$, an *integral curve of* X is a smooth curve $\gamma : I \to G$, where I is an open real interval, such that $\gamma'\,(t) = X_{\gamma(t)}$ for all $t \in I$. In the following, we will assume that $0 \in I$. In this case, if $\gamma\,(0) = g$, we say that γ is an *integral curve starting at* g.

In other words, an integral curve of a vector field X solves a system of first order ordinary differential equations with initial condition:

$$\begin{cases} \dfrac{d\gamma}{dt}\,(t) = X\,(\gamma\,(t)) \ , \text{for } t \in I \\ \gamma\,(0) = g. \end{cases} \tag{2.1}$$

Theorem 2.4. *Every one parameter subgroup of a Lie Group is an integral curve of a left invariant vector field.*

Definition 2.13. Let G be a Lie group G with Lie algebra $\mathfrak{g}$. We define the *exponential map* by

$$\exp : \mathfrak{g} \longrightarrow T_e G$$
$$X \longmapsto F\,(1)\,,$$

where F is the one-parameter subgroup generated by X, or equivalently the integral curve of X starting at the identity.

The exponential map is a diffeomorphism from some neighbourhood of 0 in $\mathfrak{g}$ to a neighbourhood of e in G. If G is simply connected, the exponential map is a global diffeomorphism.

2.2 Sub-Riemannian manifolds

Sub-Riemannian manifolds are generalizations of Riemannian ones. We will give a brief overview to Riemannian metric structures on differentiable manifolds. The definitions we will provide lend themselves to be then well adapted to the sub-Riemannian case.

2.2.1 Riemannian metrics

Definition 2.14. A *Riemannian metric* on a differentiable manifold M is given by a scalar product on each tangent space $T_p M$ which depends smoothly on the base point p. A *Riemannian manifold* is a differentiable manifold, equipped with a Riemannian metric.

In local coordinates, if a point $p \in M$ is determined by $x(p) = (x^1, \ldots, x^n)$, then the metric $(g_{ij}(x))_{i,j=1,\ldots,n}$ is a positive definite symmetric matrix with components g_{ij} which depend smoothly on p. Hence the scalar product of two tangent vectors

$$v = \sum_{i=1}^{n} v^i \frac{\partial}{\partial x^i}, \quad w = \sum_{j=1}^{n} w^j \frac{\partial}{\partial x^j}, \quad v, w \in T_p M,$$

in terms of the metric components is defined as

$$\langle v, w \rangle := \sum_{i,j=1}^{n} g_{ij}(x(p)) v^i w^j = \sum_{i,j=1}^{n} \left\langle \frac{\partial}{\partial x^i}, \frac{\partial}{\partial x^j} \right\rangle v^i w^j \tag{2.2}$$

and the length of $v \in T_p M$ is given by

$$|v| := \langle v, v \rangle^{\frac{1}{2}}.$$

As for the length of a curve, let $[a, b]$ be a closed interval in $\mathbb{R}$ and $\gamma : [a, b] \to M$ be a $\mathcal{C}^1$ curve. The length of γ is defined by

$$L(\gamma) := \int_a^b \left| \frac{d\gamma}{dt}(t) \right| dt,$$

which in local coordinates $x(\gamma(t)) = (x^1, \ldots, x^n)$ can be computed by

$$L(\gamma) := \int_a^b \sqrt{\sum_{i,j=1}^{n} g_{ij}(x(\gamma(t))) \dot{x}^i(t) \dot{x}^j(t)} dt,$$

with the abbreviation $\dot{x}^i(t) := \dfrac{d}{dt}(x^i(\gamma(t)))$.

On a connected Riemannian manifold, any couple of $p, q \in M$ can be connected by a piecewise smooth curve.

Hence, on a Riemannian manifold, the *distance* between two points p, q can be defined:

$$d(p, q) := \inf\{L(\gamma) : \gamma \text{ is a piecewise smooth curve with } \gamma(a) = p, \gamma(b) = q\}.$$

Due to the connectivity assumption, the distance function $d(p, q)$ is always well defined and it satisfies the usual axoms:

(i) $d(p, q) \geqslant 0$ for all p, q and $d(p, q) > 0$ for all $p \neq q$,

(ii) $d(p, q) = d(q, p)$,

(iii) $d(p, q) \leqslant d(p, r) + d(r, q)$ (triangle inequality) for all points $p, q, r \in M$.

2.2.2   Hörmander vector fields and sub-Riemannian structures

A sub-Riemannian manifold is a Riemannian manifold together with a constrain on allowed directions over the tangent space (see for example Le Donne [104]). Such constrain is referred as a distribution of the tangent bundle.

Definition 2.15. Let M be a differentiable manifold of dimension n. We call *distribution* Δ a subbundle of the tangent bundle. Δ is a *regular distribution* if at every point $q \in M$ there exists a neighbourhood $U_q \subset M$ of q and m linearly independent smooth vector fields $X_1, \cdots, X_m$ defined on U_q such that for any point $p \in U_q$

$$Span\left(X_{1_{|p}}, \ldots, X_{m_{|p}}\right) = \Delta_p \subseteq T_p M.$$

If the distribution is regular, the vector space Δ_p, is called *horizontal tangent space* at the point p. The distribution Δ defined in this way is called *horizontal tangent bundle* of rank m.

In the sequel we will always consider the following generalization of Riemannian manifolds.

Definition 2.16. We will call *degenerate Riemannian manifold* a triple (M, Δ, g), where

1. M is a differentiable manifold,

2. Δ is an horizontal tangent bundle of rank m

3. g is a metric defined on Δ

Definition 2.17. The metric g induces on the space a scalar product and a norm called respectively *horizontal scalar product* and *horizontal norm*, as in definition (2.2).

Remark 2.1. Let us explicitly note that in order to give the analogous definition of scalar product in this setting, we have used the regularity of the distribution.

We stress the fact that in a Riemannian manifold the scalar product is defined on the whole tangent space of each point of the manifold, whereas in a degenerate Riemannian manifold the scalar product is defined in a precise subset of the tangent space.

For each ξ and each vector field X_j defined on U_ξ will be represented as

$$X_j := \sum_{k=1}^{n} a_{jk} \partial_k, \quad j = 1, \ldots, m, \tag{2.3}$$

in U_ξ with $m < n$ and a_{jk} of class $\mathcal{C}^\infty$.

Remark 2.2. Since we are interested in local properties of the vector fields, we will often assume that the vector fields $X_1, \cdots, X_m$ are defined on the whole manifold M. If the metric is not explicitly defined, we will implicitly choose the metric g which makes the basis $X_1, \ldots, X_m$ an orthonormal basis.

As we recalled in Lemma 2.1, the horizontal tangent bundle is naturally endowed with a structure of Lie algebra through the bracket. Moreover, the commutator is a first order vector field obtained as a difference of second order derivatives, so that there is a kind of homogeneity on the second derivative that we will soon analyze.

Definition 2.18. We call *Lie Algebra generated by* $X_1, \ldots, X_m$ and denoted as

$$\mathcal{L}(X_1, \ldots, X_m)$$

the linear span of the operators $X_1, \ldots, X_m$ and their commutators of any order.

Definition 2.19. By considering the following notations

$$\begin{aligned}
\Delta^0 &= \{0\} \\
\Delta &= Span(X_1, \ldots, X_m) \\
\Delta^2 &= Span(X_i, [X_j, X_s]), \quad X_i, X_j \in \Delta, \ X_s \in \Delta \\
&\cdots \\
\Delta^k &= Span(X_i, [X_j, X_s]), \quad X_i, X_j \in \Delta^{k-1}, \ X_s \in \Delta \\
&\cdots
\end{aligned}$$

We will say that a vector field X has degree k if $X \in \Delta^k \backslash \Delta^{k-1}$. In this case we write $deg(X) = k$.

Remark 2.3. The degree is unique, indeed, if we consider the following vector fields in $\mathbb{R}^2 \times S^1$ where points are denoted by $\xi = (x_1, x_2, \theta)$:

$$X_1 = \cos(\theta)\,\partial_1 + \sin(\theta)\,\partial_2, \quad X_2 = \partial_\theta$$

their Lie bracket is $[X_1, X_2] = \sin(\theta)\,\partial_1 - \cos(\theta)\,\partial_2$ and $X_1 = -[X_2, [X_2, X_1]]$. Thus, X_1 is both in Δ and Δ^3, but for our definition the degree is 1.

Remark 2.4. Since $m < n$, in general

$$\mathcal{L}(X_1, \ldots, X_m)$$

will not coincide with the Euclidean tangent plane. If these two spaces coincide, we will say that the Hörmander condition is satisfied as we will see in the next Definition.

Definition 2.20. Let M be a regular manifold of dimension n and let $(X_j)_{j=1,\ldots,m}$ be a family of smooth vector fields defined on M. If the condition

$$\mathcal{L}(X_1, \ldots, X_m)_{|\xi} = T_\xi M \simeq \mathbb{R}^n \quad , \ \forall \xi \in M$$

is satisfied, we say that the vector fields $(X_j)_{j=1,\ldots,m}$ satisfy the *Hörmander condition* and they are called *Hörmander vector fields*.

Remark 2.5. If this condition is satisfied at every point ξ we can find a number s such that $(X_j)_{j=1,\ldots,m}$ and their commutators of degree smaller or equal to s span the space at ξ. If s is the smallest of such natural numbers, we will say that *the space has step s at the point* ξ. At every point we can select a basis $\{X_j : j = 1, \ldots, n\}$ of the space made out of commutators of the vector fields $\{X_j : j = 1, \ldots, m\}$. In general the choice of the basis will not be unique, but we will choose a basis such that for every point

$$Q = \sum_{j=1}^{n} deg(X_j) \tag{2.4}$$

is minima. The value of Q is called *homogeneous dimension* of the space. In general it is not constant, but by simplicity in the sequel we will assume that s and Q are constant in the considered open set. This assumption is always satisfied in a Lie group.

Example 2.2. The simplest example of family of vector fields is the Euclidean one: $X_i = \partial_i$, $i = 1, \ldots, m$ in $\mathbb{R}^n$. If $m = n$, then the Hörmander condition holds, while it is trivially violated if $m < n$.

Example 2.3. Let us consider the following vector fields in $\mathbb{R}^3$ where the points are denoted as $\xi = (x, y, z)$ and

$$X_1 = \partial_x + z\partial_y, \quad X_2 = \partial_z.$$

Since $[X_1, X_2] = -\partial_y$, Hörmander condition is satisfied.

Example 2.4. If we consider the vector fields in $\mathbb{R}^2 \times S^1$ used in Remark 2.3 as the generators of the Lie algebra, namely

$$X_1 = \cos(\theta)\,\partial_1 + \sin(\theta)\,\partial_2 \ \text{ and } \ X_2 = \partial_\vartheta,$$

their commutator is
$$X_3 = [X_1, X_2] = \sin(\theta)\,\partial_1 - \cos(\theta)\,\partial_2,$$

which is linearly independent of X_1 and X_2. Therefore, even in this case, X_1, X_2 are Hörmander vector fields

Definition 2.21. A *sub-Riemannian manifold* is a degenerate Riemannian manifold (M, Δ, g) such that for every ξ in M there exists a basis $X_1, \cdots, X_m$ of the horizontal tangent bundle Δ in a neighborhood of the point ξ satisfying the Hörmander condition.

Remark 2.6. Let us note that if for every ξ in M there exists a basis $X_1, \cdots, X_m$ of the horizontal tangent bundle Δ in a neighborhood of the point ξ satisfies the Hörmander condition, any other basis satisfies the same condition.

The geometry of the space is described through objects whose tangent vectors belong to the fixed distribution Δ. In particular

Definition 2.22. Let (M, Δ, g) be a sub-Riemannian manifold. A curve $\gamma : [0, 1] \to M$ of class $\mathcal{C}^1$ is called *horizontal*, if and only if $\gamma'(t) \in \Delta_{\gamma(t)}$, $\forall t \in [0, 1]$.

Let us explicitly note that the dimension of the distribution will be in general strictly smaller than the dimension of its generated Lie algebra. We say that a distribution is of type (m, n) if the horizontal distribution has dimension m and its generated Lie algebra has dimension n. We also recall that the distribution Δ generated by Hörmander vector fields is called bracket-generating. Under this assumption, a connectivity properties holds true,

Theorem 2.5. *(Chow–Rashevskii [36]). If a subbundle Δ of the tangent bundle of a connected manifold M is bracket generating, then any couple of points can be joined by a horizontal path.*

If the connectivity property is satisfied, it is possible to give a definition of distance of the space. If we choose the Euclidean metric on the horizontal tangent bundle, we can call length of any horizontal curve γ

$$L\left(\gamma\right) = \int_0^1 \left|\gamma'\left(t\right)\right| dt, \tag{2.5}$$

where $\left|\cdot\right|$ denotes the horizontal norm introduced in Definition 2.17. Consequently, we can define a distance as:

$$d\left(\xi, \xi_0\right) = \inf\{L\left(\gamma\right) : \gamma \text{ is an horizontal curve connecting } \xi \text{ and } \xi_0\}. \tag{2.6}$$

This distance is also called *Carnot-Carathéodory distance*.

Let us now give a precise estimate of this distance.

As a consequence of Hörmander condition we can locally represent any vector in the form

$$X = \sum_{j=1}^n e_j X_j.$$

The norm $\sqrt{\sum_{j=1}^m \left|e_j\right|^2}$ is equivalent to the horizontal norm expressed in Definition 2.17. We can extend it as a homogeneous norm on the whole space setting:

$$\|e\| = \left(\sum_{j=1}^n \left|e_j\right|^{\frac{Q}{deg\left(X_j\right)}}\right)^{\frac{1}{Q}}, \tag{2.7}$$

where Q has been defined in Remark 2.5.

Let us explicitly note that for every real number α, the norm in (2.7) is equivalent to the norm

$$\|e\|_\alpha = \sum_{j=1}^n \left(\left|e_j\right|^{\frac{Q}{\alpha\, deg(X_j)}}\right)^{\frac{1}{\alpha Q}}. \tag{2.8}$$

A standard choice of the norm is to choose α as the largest number such that $\frac{Q}{\alpha\, deg(X_j)}$ is integer for every j.

Since the exponential mapping is a local diffeomorphism, we give the following

Definition 2.23. If $\xi_0 \in \Omega$ is fixed, we define *canonical coordinates of ξ around a fixed point ξ_0*, the coefficients e such that

$$\xi = \exp\left(\sum_{j=1}^n e_j X_j\right)\left(\xi_0\right). \tag{2.9}$$

We only enunciate that this representation can be used to give another characterization of the distance

Proposition 2.6. *The distance defined in* (2.6) *is locally equivalent to*

$$d_1\left(\xi, \xi_0\right) = \|e\|, \tag{2.10}$$

where e are the canonical coordinates of ξ around ξ_0 and $\|\cdot\|$ is the homogeneous norm defined in (2.7).

Distance (2.10) is called *homogeneous distance* of the space.

2.3   Sub-Riemannian geodesics

2.3.1   Normal geodesics

We will recall here the Hamiltonian system which governs the subriemannian geodesic flow (see also [114] section 1.5 and Appendix A for a more detailed description). Let us consider a local frame $\left(X_a\right)_{a=1}^m$ of vector fields for the distribution Δ and its dual on the cotangent bundle, given by $P_{X_a}\left(q, p\right) = p\left(X_a\left(q\right)\right),\ q \in M, p \in T_q^*M$.

If $g_{ab}\left(q\right) = \left\langle X_a\left(q\right), X_b\left(q\right)\right\rangle_q$ is the matrix of inner products defined by the horizontal frame, let us consider $g^{ab}\left(q\right)$ be its inverse matrix. Therefore g^{ab} is a $m \times m$ matrix-valued function defined in some open set of M.

Proposition 2.7. *If P_a and g^{ab} are the functions on T^*M that are induced by a local horizontal frame $\left(X_a\right)$ as just described, then the Hamiltonian is given by*

$$H\left(q, p\right) = \frac{1}{2}\sum g^{ab}P_a\left(q, p\right)P_b\left(q, p\right). \tag{2.11}$$

Since $X_a = \sum X_a^i\left(x\right)\frac{\partial}{\partial x^i}$ is the expression for X_a relative to coordinates x^i, then $P_{X_a}\left(x, p\right) = \sum X_a^i\left(x\right)p_i$, where $p_i := P_{\frac{\partial}{\partial x^i}}$.

In terms of the canonical coordinates $\left(x^i, p_i\right) \in T^*M$, the differential equations governing the geodesics flow, named normal geodesic equations, are given by

$$\dot{x}^i = \frac{\partial H}{\partial p_i} \quad , \quad \dot{p}_i = -\frac{\partial H}{\partial x^i}. \tag{2.12}$$

Definition 2.24. Solutions of (2.12) projected on M are called normal geodesics.

Normal geodesics are locally minimizing geodesics, indeed we recall the following

Theorem 2.8. *(Montgomery [114]). Let $\left(\gamma\left(s\right), p\left(s\right)\right)$ be a solution of system* (2.12) *on T^*M, where $\gamma\left(s\right)$ is its projection on M. Then every sufficiently short arc of γ is a minimizing subriemmannian geodesic. Moreover, γ is the unique minimizing geodesic joining its endpoint.*

2.3.2   Regular and singular curves

Unlike the Riemannian enivroment, in sub-Riemannian geometry there exist minimizing curves for the length functional which are not solutions of the corresponding geodesic equations (see for instance [111],[114], [29], [144]). This question motivates the following brief outline on regular and singular curves. Below we will adopt the approach developed by L. Hsu [86] (see also [39, 74]).

Let h be a Riemannian metric on the whole tangent bundle TM. We complete $X_1, \ldots, X_m$ be a basis of Δ_p, $p \in M$, by adding $X_{m+1}, \ldots, X_n$ that generates $\mathcal{V}_p = (\Delta_p)^\perp$. We can therefore express a vector field V in terms of $(X_i)_{i=1}^n$:

$$V = V_H + V_V = \sum_{i=1}^m v_{H_i} X_i + \sum_{j=m+1}^n v_{V_j} X_j. \tag{2.13}$$

According to the notations just provided, we express the notion of admissible vector field given by G. Giovannardi [39].

Definition 2.25. Given a curve $\gamma : I \to M$, a vector field V along γ with compact support in I is called admissible if it satisfies the following $(n-m)$ linear first order ordinary differential equations

$$V_V' = -BV_V - AV_H, \tag{2.14}$$

where $B(s)$ is a square matrix $(n-m) \times (n-m)$ and $A(s)$ is of order $(n-m) \times m$, with components

$$a_{ri} = \langle [\gamma', X_i], X_r \rangle, \quad b_{rj} = \langle [\gamma', X_j], X_r \rangle, \quad r, j = m+1, \ldots, n$$
$$i = 1, \ldots, m.$$

We now introduce the concept of holonomy map first showed by Hsu [86] in 1991.

Definition 2.26. Let $\gamma : I \to M$ be a horizontal curve and $[a, b] \subset I$. Fixed $V_H \in C^1((a,b), \Delta)$ and $V_V(a) = 0$, let us consider the solution $V_V(s)$ of ODE (2.14). The holonomy map is defined as

$$H_\gamma^{a,b} : C^1((a,b), \Delta) \to \mathcal{V}_{\gamma(b)}$$
$$V_H \mapsto V_V(b).$$

Definition 2.27. (Hsu [86]). In the above conditions, we say that γ restricted to $[a,b]$ is regular if the holonomy map $H_\gamma^{a,b}$ is surjective. If the holonomy map is not surjective, we say that γ is singular.

G. Giovannardi provided a useful criterion of non-regularity of curves, which consists on the following

Theorem 2.9. *([74]). The horizontal curve γ is singular restricted to $[a, b]$ if and only if there exists a row vector field $\Lambda(s) \neq 0$ for all $s \in [a, b]$ that solves the following system*

$$\begin{cases} \Lambda'(s) = \Lambda(s) B(s) \\ \Lambda(s) A(s) = 0. \end{cases} \tag{2.15}$$

Finally, we recall a theorem which clarifies some relations between the different types of geodesics.

Theorem 2.10. *([114]). Every regular minimizing curve (i.e. regular geodesic) is normal.*

As proved by Montgomery (see [114], section 5.3), the union between singular and regular geodesics is the whole set of minimizers. Moreover, as we have just stated in the previous theorem, regular minimizing geodesics are included in the normal ones. Nevertheless, the converse inclusion is false in general, since it may exists normal geodesics which are singular.

Chapter 3

A sub-Riemannian model of M1 cells encoding movement direction

The goal of this Chapter is to propose a neurogeometrical model for the behaviour of cells of the arm area of the primary motor cortex (M1). From Georgopoulos neural models outlined in sections 1.2.1 and 1.2.1.1 ([70, 68]), we will first introduce a fiber bundle structure which allows to describe the hypercolumnar organization of the cortical area. On this setting, we will consider the selective tuning of M1 neurons of kinematic variables of positions and directions of movement. We will then extend this model to encode the direction of arm movement which varies in time, as experimentally measured by Hatsopoulos [81] by introducing the notion of movement fragments (see section 1.2.2). This leads to consider a higher dimensional geometrical structure where fragments will be represented as integral curves. A fitting of parameters with neurophysiological data will be described, and a comparison with the curves obtained through numerical simulations and experimental data will be presented. Finally, we will compare our model with the area of V1 responsible for movement coding, which exhibits analogous time-dependent receptive profiles.

The Chapter is organized as follows. In section 3.1 we show a fiber bundle structure emerging from Georgopoulos neural models in terms of hand's position and movement direction in the plane (see section 1.2.1). In section 3.2 we extend the model in order to include other kinematic variables to which motor cortical cells are selective. In section 3.3, we integrate in a unified framework the preceding models by considering a 6D space which codes time, position, direction of movement, speed and acceleration of the hand in the plane. Finally, in section 3.4 we describe a fitting of parameters with neurophysiological data. In 3.4.2, we will compare our model with the area of V1 responsible for movement coding, which exhibits analogous time-dependent receptive profiles.

3.1   Fiber bundle of positions and movement directions

As briefly exposed in section 1.2.1, Georgopoulos neurophysiological studies [70, 64] experimentally verify that the basic functional properties of cellular activity in the arm area of M1 involve directional and positional tuning. We therefore consider that a motor cortical neuron can be represented by a point $(x, y, \theta) \in \mathbb{R}^2 \times S^1$, where (x, y) denotes cell's coding for hand's position in a two dimensional space and θ represents cell's preferred direction at position (x, y). Moreover, as it is represented in Figure 1.4, cells with similar preferred directions are organized in columns perpendicular to the cortical surface. Directional columns are in turn grouped into hypercolumns (see Figure 1.5), each of them coding for the full range of reaching directions. Hence, in this first model, we propose to describe directionally tuned cells organization as a fiber bundle (E, M, F, π) (see Definition 2.1), where

- $M \subset \mathbb{R}^2$ represents the cortical tuning for hand's position in the plane;

- $F = S^1$ represents the preferred directions of the cell in the plane;

- E is the total tuning space to which motor cortical cells are selective and it is locally described by the product $\mathbb{R}^2 \times S^1$;

- $\pi : E \to M$ is a projection on the (x, y) variables which acts as $\pi(x, y, \theta) = (x, y)$.

A section $\sigma : M \to E$ represents the selection of a point on a fiber of possible movement directions at position $(x, y) \in M$, namely, it associates the point (x, y) to a point $(x, y, \theta) = \sigma(x, y)$. A fiber $E_{(x,y)} = \pi^{-1}(x, y) \simeq S^1$ corresponds to an entire hypercolumn. A schematic representation of the fiber bundle structure is shown in the right side of Figure 3.1.

We recall that formula (1.1), which is equivalent of (1.5) for every fixed instant of time, selects the maximum of the scalar product in the direction of the trajectory of movement. This is equivalent to say that the spike probability is maximized if the scalar product in the direction orthogonal to that of motion vanishes. For our model it will be essential to consider this and to do so we will make use of the following definition. We call 1-form a function $\omega = a_1 dx + a_2 dy$ which acts on a vector v as a scalar product:

$$\omega(v) = \langle a, v \rangle. \tag{3.1}$$

In our case, to be compatible with equation (1.5), we will choose $a = k^\perp$, where k expressed cell's preferred movement trajectory.

To proceed in our fiber bundle model, we will exploit the main differential constraints which characterize the features selected by the single neurons of this area. The variable encoded, or *engrafted* (in the sense adopted by Petitot [127] and Hubel [87]), in the fiber

bundle is the angle of preferred movement direction, defined as $\theta = \arctan 2 \, (\dot{y}, \dot{x})$. From here, we deduce the equality $\tan \, (\theta) = \frac{\mathrm{d}y}{\mathrm{d}x}$ which can be expressed as $\sin \theta \, \mathrm{d}x = \cos \theta \, \mathrm{d}y$. This expression is equivalent to the vanishing of the following 1-form

$$\omega = - \sin \theta \, \mathrm{d}x + \cos \theta \, \mathrm{d}y, \qquad (3.2)$$

which selects the vector $k_\theta^\perp = (- \sin \theta, \cos \theta, 0)$ on the tangent space $\mathbb{R}^2 \times S^1$.
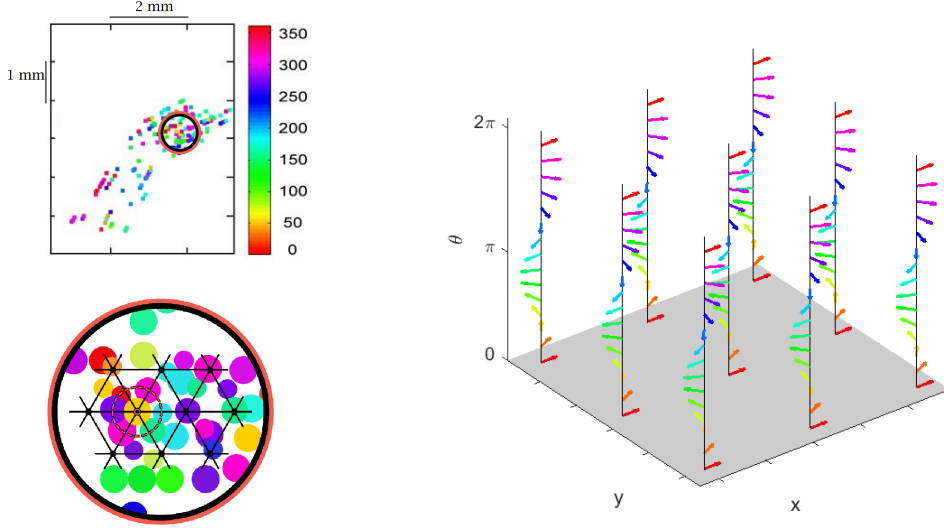

Figure 3.1: (Left) In the up, motor cortical map of preferred directions referred to movements on a two-dimensional space (adapted from [122]). Colors denote preferred directions within the interval $[0, 2\pi]$. A conventional zoom and a superimposition of the lattice model (see Figure 1.5) have been made in order to visualize the directional map referred to the size of the hypercolumns. (Right) Arm area of M1 modelled as a set of hypercolumns. Here, the angle θ lies in the interval $[0, 2\pi]$ and it is represented as an arrow.

3.1.1   Neuronal population vector and distance

As we clarified, we are interested in the set of vectors on which the 1-form (3.2) vanishes, or equivalently, on the orthogonal space to the one spanned by vector $k_\theta^\perp$. This set identifies a two-dimensional subset of the tangent space at every point, called the horizontal tangent space. It can be represented as

$$D_{(x,y,\theta)} = \{\alpha_1 \vec{X}_1 + \alpha_2 \vec{X}_2 : \alpha_1, \alpha_2 \in \mathbb{R}\}, \qquad (3.3)$$

where the generators are

$$\vec{X_1} = (\cos\theta, \sin\theta, 0) \quad , \quad \vec{X_2} = (0, 0, 1). \tag{3.4}$$

In terms of vector fields, they will be denoted respectively

$$X_1 = \cos\theta \frac{\partial}{\partial x} + \sin\theta \frac{\partial}{\partial y} \quad , \quad X_2 = \frac{\partial}{\partial \theta}. \tag{3.5}$$

According to Chow's Theorem (see [114] and [5] for a detailed analysis), vector fields (3.5) induce on the space $\mathbb{R}^2 \times S^1$ a distance d in terms of Definition 2.6.

We saw in section 1.2.1 (see also [73, 67, 71]) that one estimate concerning the output of a population of M1 cells is given by the neuronal population vector (1.2). Its formula describes an expectation value weighted by the w-functions with respect to all possible cells preferred directions $\theta' \in S^1$. Basically each cell assigns a contribution to the output given by its own preferred direction modulated by the distance between the actual direction of movement and cell's preferred direction itself. As reported in [122], within each hypercolumn the neuronal population vector ensures a good estimate of a reaching direction. These results suggest that within each hypercolumn of M1 there is a local and isotropic activity pattern characterized by the weight functions. We observe that the weight (1.3) can locally be approximated through Taylor expansion by

$$\cos(\theta - \theta') \simeq 1 - \frac{|\theta - \theta'|^2}{2} \simeq e^{-\frac{|\theta - \theta'|^2}{2}}.$$

Since for small values of θ the distance in the circumfrence is $|\theta - \theta'|$, this suggests approximating the discrete formula (1.2) with the continuous correspective in which the weight (1.3) is replaced with the exponential

$$P(\theta) = \int_0^{2\pi} e^{i\theta'} e^{-\frac{|\theta - \theta'|^2}{2}} d\theta'. \tag{3.6}$$

This formula can also be exploited in our case. Indeed, if we denote by d the distance induced by vector fields X_1 and X_2 (see Definition 2.6), we can provide an estimate of the collective behaviour of cells tuning with respect to a selective point (x, y, θ) within a hypercolumn of positions and directions of movement:

$$P(x, y, \theta) := \int_D \int_0^{2\pi} g_{x,y,\theta}(x', y', \theta') \, \omega\left((x, y, \theta), (x', y', \theta')\right) dx' dy' d\theta', \tag{3.7}$$

where $D \subset \mathbb{R}^2$ is a subset of a cortical module and the function $(x', y', \theta') \mapsto g_{x,y,\theta}(x', y', \theta')$ represents the single cell's spike probability density in response to (x, y, θ):

$$g_{x,y,\theta}(x', y', \theta') = e^{\langle (x,y,\theta), (x',y',\theta') \rangle}. \tag{3.8}$$

The above equation is the analogue of Hatsopoulos model (1.6) only in relation to the variables of position and direction of movement.

The new weighting function

$$\omega\left((x,y,\theta),(x',y',\theta')\right) = e^{-\frac{d^2((x,y,\theta),(x',y',\theta'))}{2}} \tag{3.9}$$

measures the closeness between the cellular selectivity of the points (x,y,θ) and (x',y',θ'). Therefore, formula (3.9) is intended to express a core of connectivity (local, since it is evaluated in a small cortical module) that is functional. We briefly mention that distance d expressed in terms of (2.6) can be locally estimated by

$$d\left((x,y,\theta),(x',y',\theta')\right) \simeq \left(e_1^4 + e_2^4 + e_3^2\right)^{\frac{1}{4}}, \tag{3.10}$$

where

$$e_1 = (\theta'-\theta)\left((x'-x)\sin\theta' - (y'-y)\cos\theta'\right), \qquad e_2 = \theta'-\theta$$

$$e_3 = (\theta'-\theta)\left((x'-x)\cos\theta' + (y'-y)\sin\theta'\right).$$

Formula (3.10) follows from (2.7) (see also [121] and [114]).

We will see that the analogous for this area of formula (3.9) is provided by Bressloff-Cowan [27] and Sarti-Citti [135] models in the visual cortex.

3.1.2 Comparison of the static model with primary visual cortex V1

An analogy on the selectivity behaviour of external features with neurons in the primary visual cortex area (V1) is evident. Briefly, simple cells of the primary visual cortex process the orientation of image contours and are organized in a hypercolumnar structure: Hubel and Wiesel [90, 87] discovered that to every retinal position (which is identified to the visual cortical space through a conformal map) is associated a set of cells (hypercolumn) sensible to all possible orientations. A simplified representation is shown in the right side of Figure 3.2. Since the early '70s, a large number of differential models were developed for visual cortex areas, starting with Hoffmann [83], Petitot and Tondut [131], Bressloff and Cowan [27], Citti and Sarti [41], just to name a few of the main ones. Their models describe the functional architecture of V1 trough geometric frameworks such as contact bundles, jet bundles or Lie groups endowed with a sub-Riemannian metric.

In particular, the model expressed through the one-form (3.2) matches the one proposed by Citti-Sarti in 2006 [41] for the description of image edge selectivity by V1 cells. Likewise the visual system, the fiber bundle structure underlying motor cortical organization represents a key aspect for the modelling since its local architecture results to be induced by neurophysiology ([68], [129]). Further, both for V1 and the arm area of
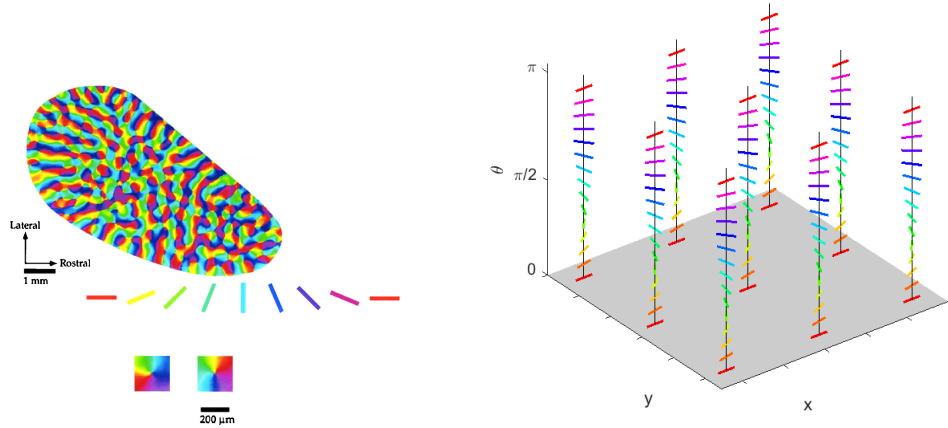
Figure 3.2: (Left) Layout of orientation preferences in the visual cortex. At singular points (pinwheels), all orientations meet. Source: [23]. (Right) V1 modelled as a set of hypercolumns.

M1, the total space of the fiber bundle is three-dimensional, whereas the cortical layers are of dimension two, so that a dimensional constraint has to be taken into account. This problem has been intensively studied for the visual system and in this case, the third dimension collapses onto the plane giving rise to orientation maps which have been experimentally observed with optical images techniques (see [23] and [127] for a detailed explanation). These maps typically contain regions where it is shown the distribution of orientation tuning over the cortical layer. In V1, at singular points all θ values are arranged like the spokes of a wheel, hence the name "pinwheel" maps. In Figure 3.2a, the orientation preferences of simple cells in V1 are color coded and every hypercolumn is represented by a pinwheel. For the motor cortex, a "directional map" is suggested from Figure 1.5, for which PDs are repeatedly arranged on the motor cortical layer in such a way that, within a given locale (hypercolumn), the full range of movement directions are represented. Moreover, as distance increases away from the center of the hypercolumn (black filled circle), up to the radius of the hypercolumn (120 μm), PDs diverge from that at the center of the circle (see Figures 3.2 and 3.1 for a direct comparison). We add that cells preferred directions in M1 are correlated across very small distances along the tangential dimension (see [7]) and this type of arrangement is consistent with the smooth variation of orientation preference observed in V1 (see [88]). Moreover, the radii of the hypercolumns of arm area M1 and V1 are of the same order size and are respectively of 240 and 200μm.

In the visual area, the retinotopic structure is a mapping between the retina and the primary visual cortices that preserves the retinal topology and it is mathematically

described by a logarithmic conformal mapping [131]. From the image processing point of view, the retinotopic mapping introduces a simple deformation of the stimulus image. Hence, in V1 there is a proved geometrical correspondence between the hypercolumnar structure of the area projected on its surface and the retinal plane. From this, not only the fiber bundle is a natural representation of the cortical area, but also the passage from the discrete hypercolumnar tiling to a continuous base plane can be justified to some extent (Petitot and Tondut [131]). In the M1 case these identifications are more complicate to achieve. In our model, we choose as a basis of the fiber bundle the cortical tuning of the position of the plane. Hence $M \subset \mathbb{R}^2$. There is wide neural literature supporting that M1 neurons encode hand positions (see e.g. [64], [100], [136], as well as sections 1.2.1 and 1.2), but the way that these positions are mapped on the cortical plane is not well understood. Possibly the position of the hand will be indirectly coded through the command to the specific group of muscles which will implement the movement [137, 66]. In particular, according to [76] (see also [77], [4], [75]) the topographic organization in motor cortex emerge from a competition among three mappings: somatotopic map of the body; a map of hand location in space; a map of movements organization. Since these maps preserve a principle of local similarity, and we are considering here very simple hand movements, a fiber bundle structure in the position-directions is not inconsistent with these data. On the other side, from a functional point of view, it is clear that at every point of the 2D space the hand can move in any direction, and this aspect is captured by a fiber bundle of directions on a 2D spatial bundle.

Another of the major difficulties and differences in modelling the functional architecture of M1 is the absence of an analogue of the simple cells receptive profiles, which we might call "actuator profiles". Simple cells of visual areas are indeed identified by their receptive field (RF) which is the domain, subset of the retinal plane, to which each cell is sensible in response to a visual stimulus. Activation of a cell's RF evokes the impulse response, which is called the receptive profile (RP) of the cell. A widely used model ([93], [46], [107]) for the RP representation of a simple cell located at the retinal position q and selective to the feature p, is in terms of Gabor filters $\psi_{(q,p)} : \mathbb{R}^2 \to \mathbb{C}$,

$$\psi_{(q,p)}(x) = e^{ip \cdot x} e^{-(x-q)^2}. \tag{3.11}$$

Although it is not well understood the presence or the definition of such functions for M1, we argue that the action of primary motor cortical cells occurs in a comparable way as in V1. This hypothesis is primarily supported by the tuning functions (1.1) and (1.4) expressed by Georgopoulos (see 1.2.1 and [70, 137]) and through the trajectory encoding model (1.6) provided by Hatsopoulos (see 1.2 and [81]). Their models share the selective tuning of neurons by evaluating the alignment between an external input variable and the individual cell's preferred feature via a scalar product. Analogously for V1, the linear term in (3.11) evaluates the aligning between cell's selective feature p with respect to the input x. Another fundamental contribution for the modelling of V1

was developed by Bressloff and Cowan [27] (see also [28, 156]). Indeed, they were able to prove the relationship between the local interactions within the hypercolumns of V1 and the generation of orientation tuning curves. More specifically, their model allows to represent the stationary state of a population of simple cells through equation

$$a\left(\phi, r\right) = \frac{\mu}{\alpha\pi} \int_0^\pi \omega_{\text{LOC}}\left(\phi, \phi'\right) \sigma\left(a\left(\phi, r\right)\right) \mathrm{d}\phi' + \frac{\mu\beta}{\alpha} \int_{\mathbb{R}} \omega_{\text{LAT}}\left(s\right) \sigma\left(a\left(\phi, r + se_\phi\right)\right) \mathrm{d}s, \quad (3.12)$$

where ω_{LOC} and ω_{LAT} correspond to the strength of connections from the iso-orientation patch within and between the hypercolumns of V1, respectively. The function $a\left(\phi, r\right)$ is the activity in an iso-orientation patch at the point r with orientation preference ϕ, whereas $\sigma\left(a\right)$ is a smooth sigmoidal function of the activity a and α, μ are time and coupling constants. The weight ω_{LOC} represents the isotropic pattern of activity within any one hypercolumn, and in [27], in the simplified case where the spatial frequencies are not taken into account, it is modelled by

$$\omega_{\text{LOC}}^{\phi'}\left(\phi\right) = \frac{1}{2}\left(\cos\left(\phi - \phi'\right) + \cos\left(\phi + \phi'\right)\right), \quad \phi, \phi' \in S^1. \quad (3.13)$$

Equation (3.13) is the analogous of the weighting function (1.3) assumed by Georgopoulos. In the work of Sarti and Citti [135] both contributions of ω_{LOC} and ω_{LAT} are modelled by means of a single connectivity kernel given by

$$\omega\left(\left(\phi, r\right), \left(\phi', r'\right)\right) = e^{-d_c^2\left(\left(\phi, r\right), \left(\phi', r'\right)\right)}, \quad \left(\phi, r\right), \left(\phi', r'\right) \in SE\left(2\right), \quad (3.14)$$

where d_c is the Carnot Carathéodory distance associated to the special Euclidean group $SE\left(2\right) \simeq \mathbb{R}^2 \times S^1$. Overall, both in V1 and M1 local interactions act as weighting functions in the activity of a population of cells within a single hypercolumn. For the motor area, this local connectivity gives rise to the neuronal population vector.

3.2   A 1D kinematic tuning model

In this section, we want to include to the previous model of positions and directions of movement the temporal aspect related to motor cortical cells behaviour (see section 1.2 and [81, 133, 38]).

First, the parameters to which primary motor cortical cells are sensible during reaching movements comprise a temporal variable (see 1.2 and also [65, 100]) together with the speed, acceleration and position of the hand ([11, 100, 116, 154, 150]). For simplicity, we will consider a one-dimensional space related only to one spatial variable, which we will denote by x. In this setting, we consider the set of kinematic variables

$$\mathcal{J}^2 = \{(t, x\left(t\right), \dot{x}\left(t\right), \ddot{x}\left(t\right)) \in \mathbb{R}^4 \mid t \mapsto x\left(t\right) \in \mathcal{C}^2\left(\mathbb{R}\right), t \in \mathbb{R}\}. \quad (3.15)$$

As a consequence, the space can be represented by the quadruple $(t, x, v, a) \in \mathbb{R}^4$. As in the previous section we will model the hypercolumnar organization ([118, 89]) through a fiber bundle structure. We will denote (t, x) the couple of time and specific hand's position. These variables will define the base space of the bundle; hand's velocity and acceleration tuning will be denoted as (v, a) and will be considered the engrafted variables on the fiber over the point (t, x). Hence, the resulting structure is described by means of a globally trivial fiber bundle represented by the product $\mathbb{R}^2_{(t,x)} \times \mathbb{R}^2_{(v,a)} \simeq \mathcal{J}^2$.

We refer to equation (1.6) to recall that the spike probability of a neuron is maximized in the direction of the movement fragment. Therefore, as in section 3.1, the choice of the variables with their differential constraints induce the vanishing of the following 1-forms

$$\begin{cases} v\, dt - dx = 0 \\ a\, dt - dv = 0. \end{cases} \tag{3.16}$$

The set where these forms vanishes is a subset of the tangent space to $\mathcal{J}^2$ and it is given by the vector fields which are orthogonal to both the 1-forms. This space is a distribution D spanned by

$$X_1 = \frac{\partial}{\partial t} + v\frac{\partial}{\partial x} + a\frac{\partial}{\partial v}, \quad X_2 = \frac{\partial}{\partial a}. \tag{3.17}$$

3.3   A 2D kinematic tuning model of movement directions

Now we aim at realizing a unified neurogeometrical framework that generalizes the preceding model of movement fiber bundle structures. We extend the one-dimensional model by involving the movement direction variable as fundamental tuning feature to which motor cortical neurons are selective. More specifically, we want to unify the fiber bundle structure relating positions and directions of movement with the two-jet geometry dealing with the selective behaviour of motor cortical cells to kinematic variables.

We will describe a sub-Riemannian model such that motor cortical cells selective behaviour can be represented through integral curves of the cortical features space of time, position, direction of movement, speed and acceleration. The resulting model will present time dependent variables, which seems particularly natural for a model of movement.

3.3.1   Integral curves and time dependent PD

We represent motor cortical cell tuning variables by the triple $(t, x, y) \in \mathbb{R}^3$, which accounts for a specific hand's position in time. We also consider the variable $\theta \in S^1$ which encodes hand's movement direction, and the variables v and a which represent

hand's speed and acceleration along θ. The triple $(t, x, y) \in \mathbb{R}^3$ is assumed to belong to the base space of the new fiber bundle structure, whereas the variables $(\theta, v, a) \in S^1 \times \mathbb{R}^2$ form the selected features on the fiber over the point (t, x, y). We therefore consider the 6D features set

$$\mathcal{M} = \mathbb{R}^3_{(t,x,y)} \times S^1_\theta \times \mathbb{R}^2_{(v,a)}, \tag{3.18}$$

where this time the couple $(x, y) \in \mathbb{R}^2$ represents the cortical tuning for hand's position in a two dimensional space.

We emphasize again that expression (1.6) modulates the increase in the cortical activity with respect to the movement trajectory. Therefore the differential constraints operating on the variables to which M1 neurons are selective can be expressed by putting together all the conditions already imposed in sections 3.1 and 3.2 by means of the vanishing of the 1-forms (3.2) and (3.16). As a result, we will get the following equalities

$$\omega_1 = \cos\theta \, dx + \sin\theta \, dy - v \, dt = 0, \quad \omega_2 = -\sin\theta \, dx + \cos\theta \, dy = 0, \quad \omega_3 = dv - a \, dt = 0. \tag{3.19}$$

The one-form ω_1 encodes the direction of velocity over time: the unitary vector $(\cos\theta, \sin\theta)$ is the vector in the direction of velocity, and its product with $(\dot{x}, \dot{y})$ yields the speed.

As we already noted, conditions above are equivalent to find vector fields orthogonal to ω_i. Consequently, the associated horizontal distribution $D^{\mathcal{M}}$ turns out to be spanned by the vector fields

$$X_1 = v\cos\theta \frac{\partial}{\partial x} + v\sin\theta \frac{\partial}{\partial y} + a\frac{\partial}{\partial v} + \frac{\partial}{\partial t}, \quad X_2 = \frac{\partial}{\partial \theta}, \quad X_3 = \frac{\partial}{\partial a}. \tag{3.20}$$

Horizontal curves of the space are integral curves of the vector fields X_1, X_2 and X_3 and are of the form

$$\gamma'(s) = \alpha_1(s) X_1(\gamma(s)) + \alpha_2(s) X_2(\gamma(s)) + \alpha_3(s) X_3(\gamma(s)), \tag{3.21}$$

where the coefficients α_i are not necessarily constants.

We recalled in section 1.2 that M1 cells are not selective to a single movement direction, but the preferred movement direction varies in time [38, 81]. In particular, in Figure 1.6b we reproduced data from [38], where the PD of a single M1 neuron was represented as a curve dependent on time.

We propose the curves expressed in (3.21) as a model of the integrated selective behaviour of M1 neurons. Note in particular that the t component of the horizontal curve γ satisfies $t' = \alpha_1$. This means that the coefficient α_1 is a modulation of the time, and can account for the difference between the external time and the perceived one. By simplicity, we will assume that the two times coincide, therefore we will assume $\alpha_1 = 1$ from now on. In the sequel we will see that it is possible to choose coefficients in equation (3.21) which allow to recover the full fan of curves reproduced in Figure 1.6.

The expression of $\dot{\theta}$ described in (3.31) is the coefficient of the vector field X_2 and the expression of $\dot{a}$ described in (3.33) is the coefficient of the vector field X_3:

$$\dot{\gamma}(t) = X_1(\gamma(t)) + \dot{\theta}(t) X_2(\gamma(t)) + \dot{a}(t) X_3(\gamma(t)). \qquad (3.22)$$

The functions $t \mapsto \dot{\theta}(t)$ and $t \mapsto \dot{a}(t)$ represent, respectively, the rate of change of the selective tuning to movement direction and acceleration variables.

3.3.2   Time-dependent neuronal population vector

By analyzing the following commutation relations

$$[X_1, X_2] = v \sin\theta \frac{\partial}{\partial x} - v \cos\theta \frac{\partial}{\partial y} =: X_4, \qquad [X_3, X_1] = \frac{\partial}{\partial v} =: X_5,$$

$$[X_5, X_1] = \cos\theta \frac{\partial}{\partial x} + \sin\theta \frac{\partial}{\partial y} =: X_6, \qquad (3.23)$$

we observe that $(X_i)_{i=1}^6$ are linearly independent. Therefore, all $(X_i)_{i=1}^3$ belonging to $D^{\mathcal{M}}$ together with their commutators span the whole tangent space at every point, meaning that Hörmander condition is fulfilled. As we recalled in Chapter 2, thanks to Hörmander condition it is possible to define a metric $d^{\mathcal{M}}$ in the whole cortical feature space $\mathcal{M}$ in terms of the Carnot-Carathéodory distance:

$$d^{\mathcal{M}}(\eta_0, \eta_1) = \inf\{l(\gamma) : \gamma \text{ is a horizontal curve connecting } \eta_0 \text{ and } \eta_1\}, \qquad (3.24)$$

where $\eta_0, \eta_1 \in \mathcal{M}$ and where the metric g defined on $D^{\mathcal{M}}$ is the one which makes X_1, X_2, X_3 an orthonormal basis. The definition of a distance (3.24) allows to formally consider the analogous of the population vector (3.7) defined in section 3.1.1. Indeed, we will call as time dependent neural population vector an estimate of the collective behaviour of cells tuning around a cortical module centered at point $\eta_0 \in \mathcal{M}$. We define it by means of the following

$$P_{\mathcal{M}}(\eta_0) := \int_E h_{\eta_0}(\eta) \, \omega_{\mathcal{M}}(\eta_0, \eta) \, \mathrm{d}\eta, \qquad (3.25)$$

where $E \subset \mathcal{M}$ is a neighbourhood of η_0 and the weighting function

$$\omega_{\mathcal{M}}(\eta_0, \eta) = e^{-d^{\mathcal{M}}(\eta_0, \eta)^2} \qquad (3.26)$$

encodes an estimate of the local connectivity between the cortical tuning points η_0 and η. The function $\eta \mapsto h_{\eta_0}(\eta)$ corresponds to the contribution provided by the variable η in the population coding. As in Hatsopoulos model (1.6), it is the spike probability of a neuron in response to the input variable η_0:

$$h_{\eta_0}(\eta) = e^{\langle \eta_0, \eta \rangle}. \qquad (3.27)$$

The definition of (3.26) embodies the same meaning as the weighting function (3.9) showed in the "static" model and in the models for visual areas (see equations (3.13), (3.14) in 3.1.2 defined in [27] and [135]). It represents the local interactions between cells within a cortical module by means of a distance of the cortical feature space.

3.4 Parameters fitting and numerical results

In this section, we validate our model through some numerical simulations compared with experimental data from [81] and [38]. We then compare our model with another model for motion encoding by V1 cells.

3.4.1 Time dependent direction selectivity as local integral curve

In section 3.3.1 we propose integral curves of vector fields (3.20) as a good model for the time dependent selected PD by M1 neurons. We will now validate the model by an ad hoc choice of the parameters.

An optimal time window for analyzing the shifts in preferred directions is approximately considered to be given by $\Delta T = 400$ msec [81]. In this temporal interval m observations have been made at instants of time $t_1, \cdots, t_m$ and the measured preferred directions can be denoted by

$$\Big(\theta(t_1), \cdots, \theta(t_m) \Big). \tag{3.28}$$

We can represent (3.28) through a continuous graph by representing the variable θ as a function of time (as it is shown in [38], see Figure 1.6b):

$$\theta : [-T, T] \to S^1. \tag{3.29}$$

This is equivalent of assuming that at every instant of time the preferred movement directions are respectively described by the unitary vectors

$$\Big(\big(\cos(\theta(t_1)), \sin(\theta(t_1)) \big), \cdots, \big(\cos(\theta(t_m)), \sin(\theta(t_m)) \big) \Big). \tag{3.30}$$

A movement fragment was visualized in Figure 1.6a taken by [81]. Here we display the same image ordering the temporal axis from left to right as it is more usual.

As for the temporal behaviour of the selective tuning of a single cell's PD, we observe that it can be linear, as it is shown for example by the black curve of Figure 1.6b. For this case we will model the function (3.29) through a polynomial of degree one (shown in Figure 3.4 left), which is identified through its first derivative. In Figure 1.6b we also see the presence of even curves, symmetric with respect to the interval where they are defined (as for example the green one). These will be described as polynomials of order two (see also Figure 3.4 middle). Finally there are odd curves, which will be represented
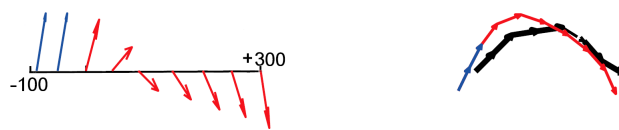
Figure 3.3: Change in cell's PD over time. Here, we ordered the temporal axis of Figure 1.6 (adapted from [81]).
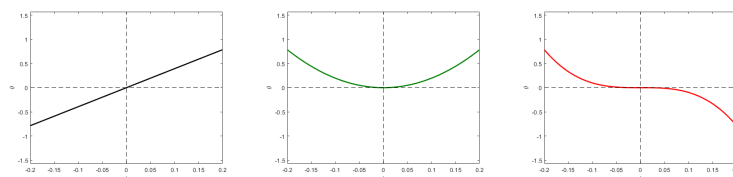

Figure 3.4: Linear, quadratic and cubic modelling functions (3.29) for the encoding of a cell's PD which spreads over time.

as third order polynomials (see also Figure 3.4 right). In this way, polynomials of degree 1, 2, 3, provide good models of the PD curves experimentally measured.

In Figure 3.5 we represent the temporal behaviour of the selective tuning of a single cell's PD through the third order polynomial function $\theta\left(t\right) = -\frac{\pi}{4}\left(\frac{t}{T}\right)^3$. On the right, we exhibit the associated unit vector $\left(\cos\theta\left(t_i\right), \sin\theta\left(t_i\right)\right)$, according to the visualization of [81]. Blue and red arrows depict the preferred movement directions before and after the time of strongest tuning, which we set to zero to be in accordance with the representation of [38].
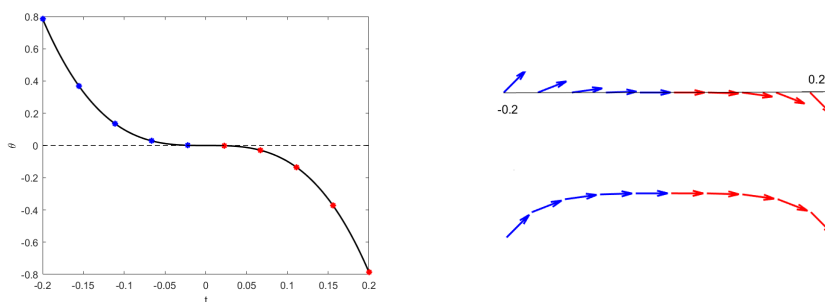

Figure 3.5: (Left) Modelling function $\theta\left(t\right) = -\frac{\pi}{4}\left(\frac{t}{T}\right)^3$, $t \in \left[-T, T\right]$ with $T = 0.2s$ for an example of a cortical cell's tuning PD in time. Red and blue dots indicate the PDs which are represented as arrows in the right plots. (Right) Associated vector representations by means of (3.30) over the temporal axis and over the (x, y) plane.

As a consequence, we assume there exist parameters k_i such that

$$\dot{\theta}(t) = k_0 + k_1 t + k_2 t^2, \tag{3.31}$$

and that all curves in the variable θ satisfying (3.22) will be characterized by these three parameters.

As briefly recalled in section 1.2 (see as well [11], [125], [143]), motor cortical cells activity is highly correlated to endpoint velocity. Since in the works of Morasso ([117],[2]) it is shown that for point-to-point movements (see also Flash and Hogan model [60]) hand's speed profile typically has a bell-shaped trend (as it is depicted also in the top of Figure 1.6b), we posit to characterize the function $t \mapsto v(t)$ by an even polynomial of fourth order. Hence, it is conceivable to characterize the speed profile by the setting of parameters j_i which identify the map $t \mapsto \dot{a}(t)$ in this way

$$\dot{a}(t) = j_0 + j_2 t^2. \tag{3.32}$$

Equation (3.32) is formulated so that the velocity profile is symmetrical with respect to the $y-$axis and the maximum speed is reached at time $t = 0$ aligning with that of the PD selection. In order to obtain a bell shape velocity profile, in which $v(-T) = v(T) = 0$ and $a(-T) = a(T) = 0$, we choose the expression of $t \mapsto \dot{a}(t)$ as

$$\dot{a}(t) = \frac{4v_0}{T^2}\left(3\left(\frac{t}{T}\right)^2 - 1\right) \tag{3.33}$$

Consequently that of the velocity is

$$v(t) = v_0 \left(\left(\frac{t}{T}\right)^4 - 2\left(\frac{t}{T}\right)^2 + 1\right). \tag{3.34}$$

To recover the fan in [38] (see Figure 1.6b), we note that the curves have been re-ordered in such a way to have the same direction and velocity at the point $t = 0$. The whole set of curves, with the prescribed initial condition $\eta_0 \in \mathcal{M}$ at time $t = 0$, represents more precisely the cortical cells selectivity with respect to position, direction of movement, speed and acceleration:

$$\begin{cases} \dot{\gamma}(t) = X_1(\gamma(t)) + (k_0 + k_1 t + k_2 t^2) X_2(\gamma(t)) + (j_0 + j_2 t^2) X_3(\gamma(t)) \\ \gamma(0) = \eta_0. \end{cases} \tag{3.35}$$

Figure 3.6 shows a family of integral curves in which we let vary the parameter k_2 and we set to zero k_0, k_1. All curves are characterized by a speed component having a bell-shaped profile, according to equation (3.34), whose maximum value occurs at time $t = 0$. This time is conceived to be the instant of a cell's strongest tuning with respect
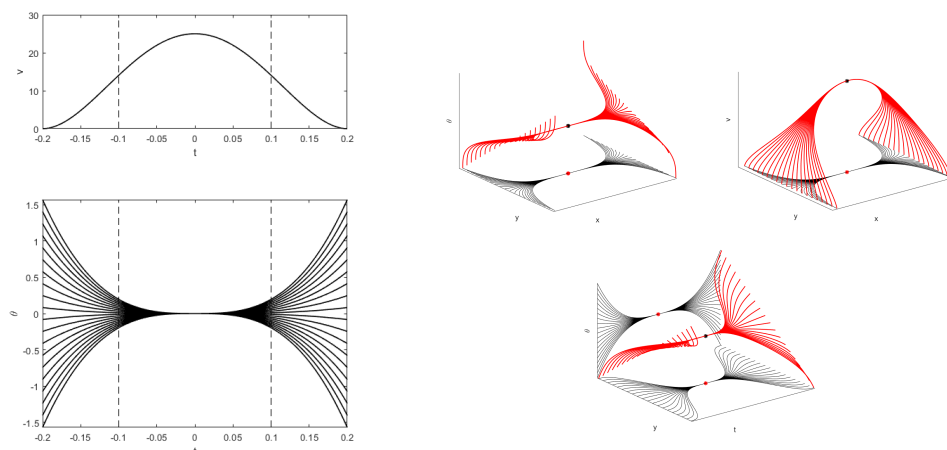
Figure 3.6: Model example of M1 cells temporal selective tuning as a family of 20 integral curves solutions of system (3.35). (Left). Above and below, speed and movement direction components solutions over the temporal window $[-0.2, 0.2]$s. Different curves correspond to different values of k_2, whereas k_0, k_1 are set to 0. The speed function is given by (3.34), with $v_0 = 25$ cm/s at time $t = 0$. (Right) Fan of curves projections over the variables (x, y, θ), (x, y, v) and (t, y, θ).

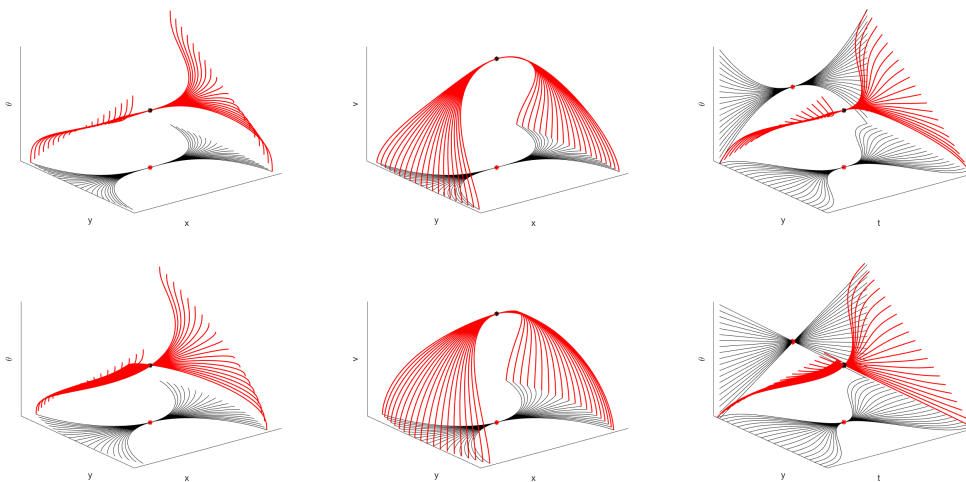Figure 3.7: Other model examples of M1 cells tuning patterns. In the top first row, the function $t \mapsto \dot{\theta}(t)$ is assumed to be a polynomial of degree one and each solution of (3.35) corresponds to a different value of the parameter k_1 of equation (3.31). In the second row, the temporal behaviour of the movement direction variable is assumed to be linear and we let vary the parameter k_0.

to the speed and movement direction variables, and, in correspondence of it, all curves meet at point $(x, y) = (0, 0)$ with tangent θ set to 0 (see red and black dots of the plots in Figure 3.6).

Let us emphasize that only curves with polynomial coefficients are considered, so that each of these trajectories can also be identified as a point in a higher dimensional space. Indeed, the initial tuning variable $\eta_0 \in \mathcal{M}$, the time threshold T, together with the coefficients $(k_0, k_1, k_2, j_0, j_2) \in \mathbb{R}^5$ which define the trend of the direction and velocity of motion with respect to η_0, form a space of dimension twelve. In particular, the dimension of the structure is of the same order as the one outlined by the principal components analysis performed in [38] and in [81]. We underline that in the "static" simplified model presented in section 3.1, a point of the space is assumed to be a neuron characterized by its positions and directions of movement. In this context, a point of the previous structure corresponds to an "instantaneous" cell selective movement parameter. Here, in the temporal bundle, the selective behaviour of a single neuron is represented by a whole trajectory expressed as a solution of (3.35). We show a simplified representation of the new fiber bundle in Figure 3.8, where we have depicted only the (x, y, θ) components to facilitate a comparison with Figure 3.1 and to directly observe the extension of the temporal model with respect to the static one. The central arrow in the left graph of Figure 3.8 has the same meaning as those depicted in the previous "static" fiber bundle, but now, as seen in the right part of the image, the fiber has a higher dimension representing the spread of time-selective behaviour.

3.4.2   Comparison with the time dependent receptive profiles in V1

We will now compare the model of movement in the arm area of cortex M1 with models of movement coded in the visual cortex V1. We stress that the analysis on the comparison between visual and motor cortical cells is not based on their functionality. Visual cells are indeed characterized by their receptive profiles which detect features of the visual stimulus; on the other hand, cells in M1 are characterized by "actuator profiles" and whose properties have been synthesized in 1.2.1 and 1.2. The analogy is based on the coding of their related features, and on the structure of the functional geometry of the two areas.

We briefly recalled in the Introduction and in 3.1.2 that simple cells in V1 detect positions, local orientations, however complex cells also encode parameters of movement via their receptive profiles ([48, 47]). For a given fixed position and orientation, cells receptive profiles sensible to movement are represented as a family of RPs varying in time (see [93], [47]):

$$\Big(RP(t_1), \cdots, RP(t_m) \Big). \tag{3.36}$$

This complex receptive profile can be modelled as a curve in the space of 2D profiles.
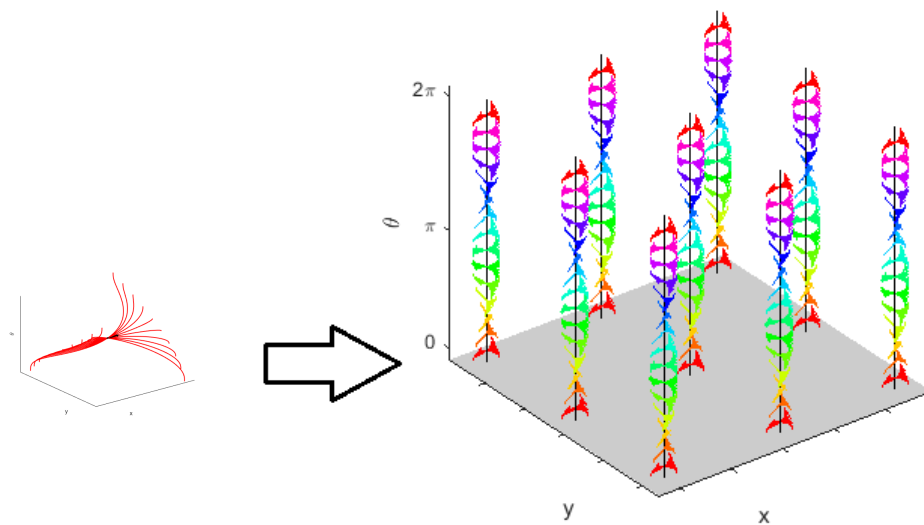
Figure 3.8: Kinematic model for time-dependent directionally tuned M1 cells. We only represent the (x, y, θ) components of system (3.35) applied for movement direction tuning which linearly changes over time. Left, fixed a PD at the central point, a solutions pattern which spreads over a temporal window is represented. Right, over each cell's selective tuning point (x, y) at time $t = 0$, there is a fiber of different patterns having strongest tuning for a preferred movement direction which spans the interval $[0, 2\pi]$.

The graph of a continuous curve of receptive profiles

$$RP : [-T, T] \to \mathbb{R}^2 \tag{3.37}$$

has been represented by G. Cocci [43] as a 3D volume defining a higher-dimensional profile selective of time frequency and velocity parameters (see Figure 3.9).
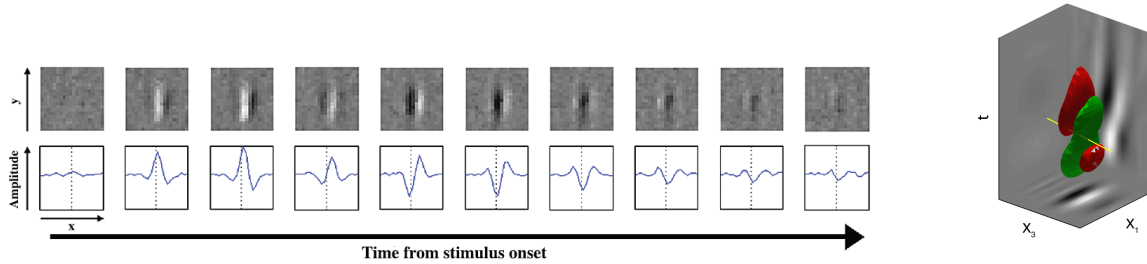

Figure 3.9: Time course of a simple cell's RP. (Left) A simple cell's RF, represented in the second row as a curve of 1D RP vaying in time. The representation is analogous to the one used for the analysis on PD vectors which vary over time in M1 (see Figure 3.3). (Right) Representation of a 3D-continuum receptive profile. It is the analogous of directionally tuned cells behaviour depicted in Figure 1.6b. Source: [43].

The variation of the RP from one frame to the next encodes the velocity of movement. Hence, we argue that the model of M1 (3.4.1) is analogous, but more general to the model of movement in V1, since we coded the variation of a cell's preferred movement direction not only via the first derivative, but via higher order derivatives. Accordingly, the movement-receptive profile family was represented in Cocci's model as a fiber bundle, with a base formed by position and time selective behaviour (q_1, q_2, t) and with engrafted variables (θ, v), accounting for the orientation and velocity tuning over the point (q_1, q_2, t). For θ fixed, there is therefore a one-parameter family of RPs depending on the velocity variable (as depicted in Figure 3.10 left). This is the analogous of the fan of curves with varying PDs we represented in Figure 3.8 left, for a given fixed central PD. Then, in the model of movement for V1, the entire fan is obtained by varying orientation and position variables (see Figure 3.10 right), from which a total space of dimension five arises.
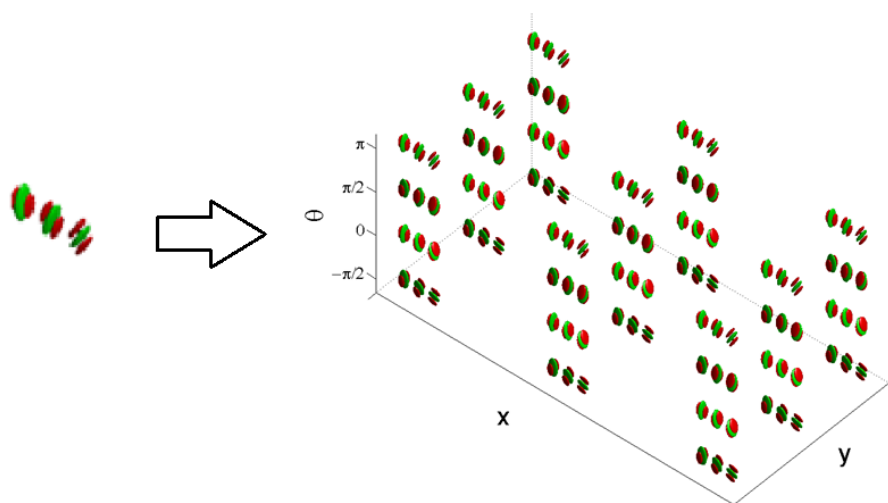
Figure 3.10: (Left) Representation of a cell's RP over time. (Right) Schematization of the spatio-temporal fiber bundle of V1. For each spatio-temporal point (x, y, t) there is a two dimensional fiber of possible local detected orientations θ and local velocity v. See Figure 3.8 for a direct comparison with M1. Images from [43].

Chapter 4

Spatio-temporal grouping model for M1

In this Chapter, we will proceed with the sub-Riemannian model for M1 cells by focusing on the coding of directional trajectories. Neural activity shows coherent behaviours represented in terms of movement trajectories pointing to a specific pattern of movement decomposition (see section 1.3.1 from [95] and Figures 1.7, 1.8, 1.9 as references). Here, we will test this pattern through the neurogeometrical model proposed in Chapter 3 applied to classical techiques of spectral clustering ([126]). By the use of a sub-Riemannian distance expressed in terms of kinematic variables, we will show how the set of movement trajectories extracted from the grouping algorithm are in accordance with the neural states obtained by Kadmon Harpaz et al. [95].

In this Chapter we consider the coherent behaviours of neural activity obtained in [95] directly on neural data and recover it in terms of kinematic parameters. As recalled in section 1.3.1, the authors clarified that they tried to obtain the neural decomposition in fragments using various distances proposed in literature. However, none of these distances were successful in yielding the desired neural decomposition. The authors recall a list of all the distances that were tried (found in equations (1.9)-(1.14)) and they all failed to produce the correct classification. This failure can have two explanations: either the considered kinematic parameters are not sufficient to recover the decomposition, and more parameters are coded in the brain, or a more complex distance is needed.

We show that with our distance which takes into account the differential relations between the variables exactly provides the same decomposition. The algorithm we apply here is a variant of k-means which considers the presence of this distance: first we perform a change of variables induced by the distance and then we apply the k-means in the new variables. This provides an answer to the problem we posed above, and clarifies that the set of kinematic variables considered up to now is sufficient to recover the cortical decomposition, and it is most probably the set of parameters to which this

area is sensible.

We have organized the Chapter as follows. In section 4.1, we will explain the results of movement decomposition from the perspective of a grouping problem. To do so, we will provide a brief overview of clustering methods in section 4.1.1. In section 4.2 we define an affinity matrix in the feature space $\mathcal{M}$ and we provide the main steps of the clustering algorithm. In 4.2.1 we give an estimate of the distance $d^{\mathcal{M}}$ defined in (3.24) which will characterize the affinity matrix. Finally, in 4.3 we present some results on the trajectories decomposition into movement fragments, comparing them with the work of Kadmon Harpaz et al. [95].

4.1   Movement decomposition as a grouping problem

In this section we will reinterpret the movement decomposition introduced by Hatsopoulos et al. [81] and Kadmon Harpaz et al. [95] as a grouping problem, with respect to a natural distance associated to the space introduced in the previous Chapter. Hatsopoulos et al. [81] and Churchland et al. [38] analyzed the response properties of single neurons, while Kadmon Harpaz et al. [95] examined the cell population in M1 at local population level, but proposed similar decompositions in fragments. The authors observed an abrupt change in population spike activity at changes in the properties of velocity differences: precisely, changes in direction of movement or changes in monotonicity (which can be captured by changes in the sign of acceleration). On the other hand, spike activity was consistent at the acceleration and deceleration phases. As a result, the movement trajectory is segmented into coherent patterns, which are short pattern trajectories, called fragments (see Figure 1.10 as a reference, from [95]). The authors also noted that the same decomposition into trajectories can not be obtained with any distance present in literature (see Equations (1.9)-(1.14)). The problem of identifying cortical activity patterns and the associated phenomenological primitives has been diffusively studied in the visual cortex for the identification of perceptual units. Starting from the Gestalt theory [101], it is clear that it is possible to express the grouping principles as geometrical rules. The same geometric features have been observed in the region of V1 where the grouping takes place. The most classical model describing the cortical activity is the mean field equation of Ermentrout and Cowan [53] and Bressloff and Cowan [26], [27]. This equation models the evolution of the cortical activity depending on a connectivity kernel and stationary states can be studied by means of eigenvalues methods (see section 3.1.2 and equation (3.12)). Sarti and Citti [135] proved a relation between the stable states of Bressloff and Cowan equation and perceptual units of the visual input in V1. We also refer to the works of Faugeras et al. [55], Cocci et al. [44], Favali et al. [56]. The main result is to relate emergent states of Bressloff and Cowan differential equation and visual perceptual units. In particular, the model in [135] provided a biological basis for the results of perceptual clustering in scene description through kernel principal component

analysis.

In perfect analogy, we will relate the neural states found in [95] to elementary trajectories obtained via a clustering algorithm. Following the approach of Citti and Sarti [135] and Cocci et al. [44], the decomposition of neural activity into movement fragments as in [95] will be recovered through a dimensionality reduction technique expressed in terms of the subriemannian distance defined in section 3.3.2. The considered distance will be used to define the kernel (3.26), which is related to the local connectivity of a neuron in response to the input variable η_0, but it is expressed only in terms of kinematic variables. In this way we strongly related the neural activity and a purely kinematic distance, and we justify the fact that the moving fragments in [95] are obtained via a clustering algorithm, only based on kinematic variables.

4.1.1   Spectral clustering and dimensionality reduction

Clustering methods based on graphs and spectral analysis have been applied successfully for data analysis in several science fields ranging from statistics, computer science, biology, social science, or psychology (e.g. [142], [1], [37]). A vast literature is available on the theoretical and practical aspects of several clustering algorithms (see e.g. [153] as a summary of the most known techniques). A key idea of these methods is that they partition the set of data in disjoint subsets: each one containing homogeneous data with respect to a suitable distance function. Precisely the given data $S = \{x_i\}_{i=1}^n \subset X$ will be partitioned in disjoint subset $S_i \subset S$ homogeneous with respect to the distance d, and such that $\bigcup_{i=1}^k S_i = S$. This partition induces a new lower dimensional representation induced by the chosen similarity criterion of the original data, where each element is an element S_i of the partition. A classical method is the k-means algorithm. The objective of k-means is to minimize the sum of squared Euclidean distances between each data point and its closest centroid, which is the representative point for the cluster it belongs to. The k-means assigns each data point to the closest centroid, based on the Euclidean distance between the data point and the centroid, and it iteratively updates the centroid for each cluster by taking the mean of all the data points assigned to that cluster. The final result is a partition of the objects into k clusters, with each object being assigned to a unique cluster [102].

Another typical example is a representation of the partition in terms of the first eigenvalues of the matrix containing distances of any couple of points, called affinity matrix ([155]). Precisely the elements a_{ij} of the affinity matrix A only depend on the similarity of point x_i to point x_j, and a possible expression of them will be

$$a_{ij} = e^{-d^2(x_i, x_j)}, \tag{4.1}$$

where d is a suitable distance over the considered space.

Principally, there exist two classes of spectral clustering techniques [103]: methods for

locality-preserving embeddings of large data sets, that project the data points onto the eigenspaces of the affinity matrices ([45], [15], [134]), and methods for data segregation and partitioning, that basically perform an additional clustering step taking as input the projected data set ([126], [155], [142], [109], [123]).

We briefly recall the work of Perona and Freeman [126] who addressed the problem of perceptual grouping by reducing the complexity of scene description, since we will apply a clustering technique inspired by their work. A visual scene composed by n points, can be analyzed via a distance d which gives rise to an affinity matrix A (4.1) with a complexity of order $O(n^2)$. They approximated the matrix A as a sum of matrices of rank 1 and complexity n, so as to drop the computational complexity from $O(n^2)$ to $O(n)$. More specifically, the considered approximation is the following

$$p = \mathrm{argmin}_{\hat{p}} \sum_{i,j=1}^{n} \left(a_{ij} - \hat{p}_i \hat{p}_j \right)^2 . \tag{4.2}$$

Perona and Freeman proved that the minimizer p (4.2) of the Frobenius norm is the first eigenvector v_1 of the matrix A with largest eigenvalue λ : $p = \lambda_1^{\frac{1}{2}} v_1$.

Then the same problem is applied to the vector space orthogonal to p_1: the minimizer will correspond to the second eigenvector, and iteratively the others eigenvectors are recovered. The dimensionality reduction is obtained by selecting only k eigenvectors, where $k < n$, and the salient objects in the scene correspond to the eigenvectors with the largest eigenvalues.

In order to obtain a more stable algorithm and to reduce error due to noise, the affinity matrix can be suitably normalized. Many normalizations have been proposed (e.g. [30], [123], [142]): one of the most widely applied is the one presented by Meila and Shi [109] since it reveals properties of the underlying affinity matrix by ways of the Markov chain, providing a probabilistic foundation of the clustering algorithm. Indeed, the authors defined a Markov-type matrix P as follows

$$P = D^{-1}A, \quad D \text{ diagonal matrix}, \quad d_i = \sum_{j=1}^{n} a_{ij}. \tag{4.3}$$

In general the matrix P will not be symmetric, but its eigenvalues are real, positive and smaller than one, while the eigenvectors have real components ([103], [45]). The clustering properties of the eigenvectors of P can be better understood in the following ideal case. Suppose the given data S can be represented as a disjoint union of k connected components S_i with the property that the distance between pairs of points in a set S_i is strictly less than the distance between points in different components. Let A be the affinity matrix A representing the similarity between pairs of points in S having distance d. The resulting normalized matrix P is a block diagonal matrix with k non-zero eigenvalues, each of which is equal to 1. The corresponding eigenvectors of these eigenvalues

are piecewise constant indicator functions of the partitions. This means that the eigenvectors indicate the presence or absence of each point in each connected component. If the affinity matrix A is already a block matrix, the improvement induced by the multiplication by D can be neglected. Further, the diffusion map theorem shows that the Euclidean distance in the coordinates induced by the projection onto the eigenspace is equivalent to the distance used to define the affinity matrix ([103], [45]). This means that the clustering result obtained by applying the k-means algorithm to the data projected onto the eigenspace will be the same as the result obtained by applying the k-means algorithm to the data directly in the affinity matrix space. For this reason, a k-means algorithm in this coordinates will provide the classification for our problem. In particular, a simple and efficient algorithm has been proposed in [98], which can be summarized as follows

1. Consider a data set S.

2. Build the affinity matrix A using definition (4.1). Define P as in (4.3) (if A is already a block matrix, $P = A$).

3. Solve the eigenvalue problem $PU = \lambda U$, where U is the matrix formed by the column eigenvectors $\{u_i\}_{i=1}^n$.

4. Order the couples $\{(\lambda_i, u_i)\}_{i=1}^n$ such that λ_i is decreasing.

5. Plot the first k-ordered eigenvectors ($k \leqslant n$) which will form the clusters for the decomposition.

4.2 The spectral clustering method in the feature space $\mathcal{M}$

In this section we apply the spectral clustering algorithm in the cortical feature space $\mathcal{M}$ defined in Chapter 3 in order to recover the classification presented in [95]. We will then study its applications to grouping the kinematic points along a series of movement trajectories through the spectral analysis related. We will introduce two main novelties. Firstly, we will provide a local estimate of the distance $d^{\mathcal{M}}$ (3.24) to define a connectivity kernel in terms of the kinematic space $\mathcal{M}$. Secondly, we will show that the salient groups obtained due to spectral clustering are in agreement with the neural results present in [95]. The eigenvectors of the affinity matrix will be short movement trajectories, coherently with the concept of movement fragments stated by Hatsopoulos et al. [81, 133].

In order to measure distances between points in $\mathcal{M}$, we use the connectivity kernel $\omega_{\mathcal{M}}(\eta_i, \eta_j)$ defined as in (4.1) as

$$\omega_{\mathcal{M}}\left(\eta_0, \eta\right) = e^{-d^{\mathcal{M}}(\eta_0, \eta)^2}, \quad \eta_0, \eta \in \mathcal{M}, \tag{4.4}$$

where $d^{\mathcal{M}}$ is defined in (3.24). As recalled before, this connectivity kernel is the same as the one we introduced in section 3.3.2 through Equation (3.26).

Hence, given a set of reaching paths, we discretize (4.4) by means of the real symmetric affinity matrix A:

$$A = \omega_{\mathcal{M}}\left(\left(x_i, y_i, \theta_i, v_i, a_i, t_i\right), \left(x_j, y_j, \theta_j, v_j, a_j, t_j\right)\right), \tag{4.5}$$

that contains the connectivity information between all the kinematic variables of the reaching trajectory. We obtain a data set, on which we apply the algorithm provided in section 4.1.1.

4.2.1   Local estimate of distance $d^{\mathcal{M}}$

In this section we will provide a local estimate of the distance $d^{\mathcal{M}}$ defined in (3.24), using an approximation result due to Nagel Stein Wainger [121], and recalled in (2.7).

The space $\left(\mathcal{M}, D^{\mathcal{M}}, d^{\mathcal{M}}\right)$ is defined in terms of the vector fields introduced in (3.20). According to Definition 2.19, we compute the degree of each of these vector fields and of their commutators (3.23):

$$X_1, \ X_2, \ X_3 \in D^{\mathcal{M}}, \text{ so that } \deg(X_1) = \deg(X_2) = \deg(X_3) = 1$$

$$X_4 = [X_1, X_2], \ X_5 = [X_3, X_1], \text{ so that } \deg(X_4) = \deg(X_5) = 2$$

$$X_6 = [X_5, X_1] = [[X_3, X_1], X_1], \text{ so that } \deg(X_4) = 3.$$

Applying equation (2.4), the homogeneous dimension is $Q = \sum_{j=1}^{n} deg\left(X_j\right) = 10$.

The homogeneous norm of a vector $X = \sum_{j=1}^{6} e_j X_j$ defined in (2.7) reduces in this case to $\|e\|_{\alpha} = \|(e_1, \cdots, e_6)\|$, with

$$\|e\|_{\alpha} = \sum_{j=1}^{6}\left(|e_j|^{\frac{10}{\alpha\, deg(X_j)}}\right)^{\frac{1}{\alpha 10}}, \quad \alpha = \frac{5}{3}. \tag{4.6}$$

In order to define a homogeneous distance in $\mathcal{M}$, according to (2.9), we have to express every point in terms of its canonical coordinates.

Equation (3.21) takes the explicit form

$$\begin{cases} \dot{\gamma}\left(s\right) = & e_1 X_1 + e_2 X_2 + e_3 X_3 + e_4 X_4 + e_5 X_5 + e_6 X_6 \\ \gamma\left(0\right) = & \left(x_0, y_0, \theta_0, v_0, a_0, t_0\right) \\ \gamma\left(1\right) = & \left(x_1, y_1, \theta_1, v_1, a_1, t_1\right). \end{cases} \tag{4.7}$$

If e_i are defined in this way, then by formula (2.10) the distance becomes

$$d^{\mathcal{H}}(\eta_0, \eta_1) = \|e\|_\alpha. \tag{4.8}$$

Remark 4.1. Given the expression of the family of constant positive coefficients $\{c_i\}_{i=1}^6$, the homogeneous distance between two points $\eta_0, \eta_1 \in \mathcal{M}$ reduces to

$$d^{\mathcal{H}}(\eta_0, \eta_1) = \left(\sum_{i=1}^3 c_i \, |e_i|^6 + \sum_{i=4}^5 c_i \, |e_i|^3 + c_6 \, |e_6|^2 \right)^{\frac{1}{6}}. \tag{4.9}$$

In our experiments, we will use the distance (4.9). However, to avoid complicating the notation, given the local equivalence of the distances $d^{\mathcal{M}}$ and $d^{\mathcal{H}}$, we will simply refer to $d^{\mathcal{M}}$.

Let us now provide an explicit expression of the coordinates e_i, by integrating system (4.7).

Remark 4.2. Using the explicit expression of the vector fields $(X_i)_{i=1}^6$ we obtain that the system (4.7) can be explicitly represented as

$$\dot{\gamma}(s) = e_1 X_1 + e_2 X_2 + e_3 X_3 + e_4 X_4 + e_5 X_5 + e_6 X_6 =$$

$$= e_1 \begin{pmatrix} v\cos\theta \\ v\sin\theta \\ 0 \\ a \\ 0 \\ 1 \end{pmatrix} + e_2 \begin{pmatrix} 0 \\ 0 \\ 1 \\ 0 \\ 0 \\ 0 \end{pmatrix} + e_3 \begin{pmatrix} 0 \\ 0 \\ 0 \\ 0 \\ 1 \\ 0 \end{pmatrix} + e_4 \begin{pmatrix} v\sin\theta \\ -v\cos\theta \\ 0 \\ 0 \\ 0 \\ 0 \end{pmatrix} + e_5 \begin{pmatrix} 0 \\ 0 \\ 0 \\ 1 \\ 0 \\ 0 \end{pmatrix} + e_6 \begin{pmatrix} \cos\theta \\ \sin\theta \\ 0 \\ 0 \\ 0 \\ 0 \end{pmatrix}.$$

In this way we get

$$\dot{\gamma}_1(s) = \dot{x} = e_1 v \cos\theta + e_4 v \sin\theta + e_6 \cos\theta$$
$$\dot{\gamma}_2(s) = \dot{y} = e_1 v \sin\theta - e_4 v \cos\theta + e_6 \sin\theta$$
$$\dot{\gamma}_3(s) = \dot{\theta} = e_2$$
$$\dot{\gamma}_4(s) = \dot{v} = e_1 a + e_5$$
$$\dot{\gamma}_5(s) = \dot{a} = e_3$$
$$\dot{\gamma}_6(s) = \dot{t} = e_1.$$

We immediately obtain

$$e_1 = t - t_0, \quad e_2 = \theta - \theta_0, \quad e_3 = a_1 - a_0, \quad e_5 = (v - v_0) - \frac{t - t_0}{2}(a + a_0). \tag{4.10}$$

Hence, by calling $\tilde{x} = x \cos(\theta) + y \sin(\theta)$ and $\tilde{y} = x \sin(\theta) - y \cos(\theta)$, we get

$$\dot{\tilde{\gamma}}_1(s) = e_1 v + e_6 - \tilde{y} e_2 \,, \quad \dot{\tilde{\gamma}}_2(s) = e_4 v + \tilde{x} e_2.$$

Therefore, by integrating $\dot{\tilde{\gamma}}_1$ and $\dot{\tilde{\gamma}}_2$ between 0 and 1 we obtain the expressions of $\tilde{x}_1 - \tilde{x}_0$ and $\tilde{y}_1 - \tilde{y}_0$, and subsequently e_4 and e_6.

In particular, if $e_2 = 0$ the two equation decouple. Since v is a polynomial, e_4 and e_6 turn out to be

$$e_4 = -\frac{12 \left(\tilde{y}_1 - \tilde{y}_0\right)}{6 \left(v_0 + v_1\right) - e_1 e_3} = \frac{12 \left(\left(x_1 - x_0\right) \sin \theta_0 - \left(y_1 - y_0\right) \cos \theta_0\right)}{6 \left(v_0 + v_1\right) - e_1 e_3},$$

$$\begin{aligned}
e_6 &= \left(\tilde{x}_1 - \tilde{x}_0\right) - \frac{e_1}{12} \left(6 \left(v_0 + v_1\right) - e_1 e_3\right) \\
&= \left(x_1 - x_0\right) \cos \theta_0 + \left(y_1 - y_0\right) \sin \theta_0 - \frac{e_1}{12} \left(6 \left(v_0 + v_1\right) - e_1 e_3\right).
\end{aligned}$$

If $e_2 \neq 0$, the system is a standard oscillator, with polynomial forcing term. Hence it can be directly integrated to find e_4 and e_6.

Remark 4.3. In the context of the grouping problem, it is important to assign meaning to the constant coefficients c_i of exponential coordinates (4.9). From a neural viewpoint, we know that neurons are selective of a restricted temporal window, typically around 400ms [81]. The experiments reported in [95] (see Figures 1.7, 1.8, 1.9) show that this temporal window captures neural state transitions. Hence, the use of a weighting factor c_i for the temporal increment in the exponential coordinates can capture this temporal organization and can help to separate the neural signals into coherent groups. To ensure this property, and also because the temporal variable includes information about velocity and acceleration, a good strategy is to weight the temporal increment more heavily. In the experiments we will present in section 4.3 we will use a large coefficient c_1 for the temporal increment e_1, while leaving the other coefficients equal to 1.

4.3   Results of movement decomposition into movement fragments

In this section we show some examples in which connectivity kernel (4.4) is applied to a set of movement paths and speed profiles. We will then analyze how the decomposition obtained through the spectral analysis of the corresponding affinity matrix (4.5) is in agreement with the neural states obtained by Kadmon Harpaz et. al [95].

4.3.1 Results

4.3.1.1 Test 1: Center-out tasks

As a first category of tests, we will analyze trajectories of movement performing a center-out task (see e.g. the one represented in Figure 1.7, from [95]). Motion paths are very simple, but also widely used for neural experiments and phenomenological models of reaching movements (recall Georgopoulos' results in 1.2.1 and the model of Flash et al. in 1.4.2).

We begin by presenting a "synthetic" example of a center-out task by making use of the equations of Flash and Hogan model (1.16).
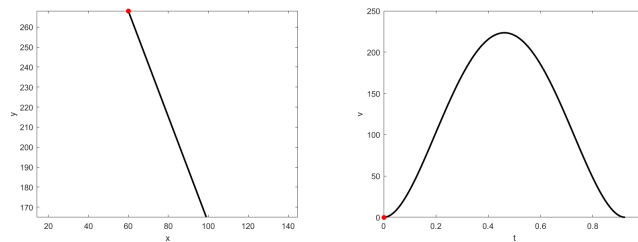

Figure 4.1: Reaching path and speed profile of a center-out task. (Left) Reaching path over the (x, y) plane. (Right) Speed profile over the (t, v) plane. The red dot represents the movement starting position.

The "idealized" movement trajectory, as in the representation of paper [95], is characterized by two graphs, one on the (x, y) plane, the reaching path, and one on the (t, v) plane, corresponding to the speed profile. The red dot identifies the starting point of the movement. In this very simple case, movement direction is constant with only one target point to be reached and just one maximum point of the speed profile.

The connectivity kernel (4.4) when applied to the kinematic variables of the task represented in Figure 4.1 forms an affinity matrix which is clearly divided into blocks (see Figure 4.2). These blocks are the eigenvectors associated to the two major eigenvalues of the affinity matrix and represent the clusters of the pattern of movement decomposition. By projecting the eigenvectors over the reaching trajectory, it turns out that these correspond precisely to the acceleration and deceleration phases of the movement task.

We show below another very similar example from the paper [95] (see Figure 1.7 as a reference).

This is again a center-out movement trajectory in which the only difference from the previous case is that the path on the (x, y) plane is almost constant, and the velocity profile is no longer perfectly symmetric. We provide an approximation of the image in Figure 4.3.

The decomposition results using kernel (4.4) are shown in Figures 4.4 and 4.5: acceleration-phase is orange-colored and deceleration-phase is blue-colored as the neural
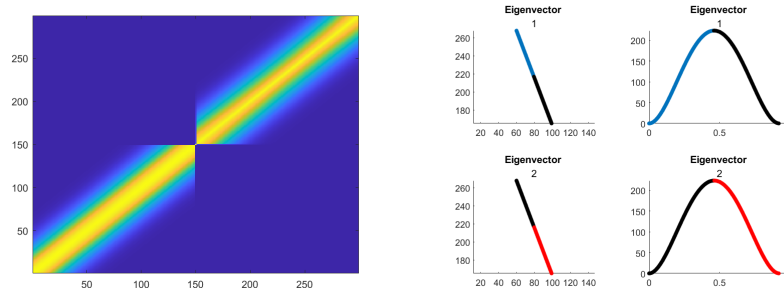
Figure 4.2: Spectral clustering on the trajectory movement of Figure 4.1 based on connectivity kernel (4.4). (Left) The Affinity matrix (4.5). Yellow-colored areas represent points of higher affinity. (Right) Eigenvectors projections over the reaching trajectory.

Figure 4.3: Reaching path and speed profile of a center-out task: approximation of Figure 1.7. (Left) Reaching path over the (x, y) plane. (Right) Speed profile over the (t, v) plane. The red dot represents the movement starting position.

Figure 4.4: Spectral clustering. (Left) The Affinity matrix (4.5). Yellow-colored areas represent points of higher affinity. (Right) Eigenvectors projections over the reaching trajectory.
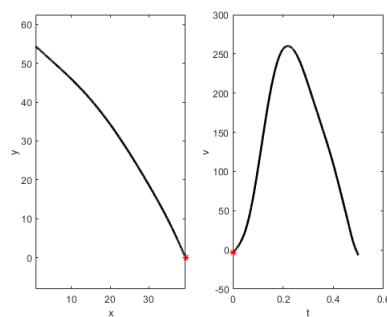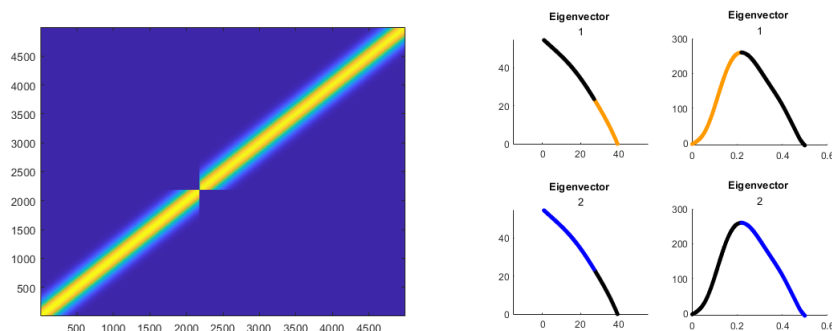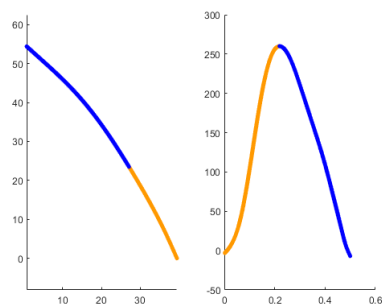
states represented in Figure 1.7.

Figure 4.5: Reaching trajectory segmentation according to the spectral analysis of (4.5) (see also Figure 4.4). Eigenvectors identify acceleration and deceleration trajectories according with the experimental results of [95]. See Figure 1.7 for a direct comparison.

4.3.1.2   Test 2: straight trajectories changing movement direction

In this test we again consider optimal and ideal movements that satisfy the equations of Flash and Hogan's model (see Equations (1.16)). Let us consider a movement of a hand that, starting from an initial point, reaches the targets shown in blue one by one, again by means of straight paths and bell-shaped velocity profiles. For each of the two targets to be reached, there is a change in direction of 150 and 135 degrees. We therefore re-test the kernel (4.4) on the kinematic points of the trajectory depicted in Figure 4.6.
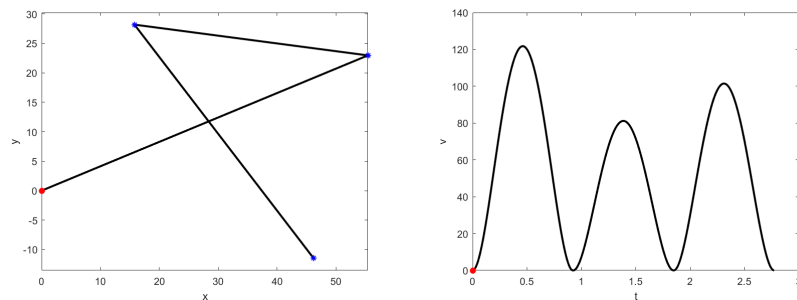
Figure 4.6: Three consecutive point-to-point reaching trajectories according to Flash and Hogan model. (Left) Reaching path over the (x, y) plane. (Right) Speed profile over the (t, v) plane. The red dot represents the movement starting position, and the blue ones the targets to be reached.

The corresponding affinity matrix is displayed in Figure 4.7 and on the right is the graph of the eigenvalues arranged in descending order. The affinity matrix is divided into six blocks, as are the larger eigenvalues.

Figure 4.7: Spectral clustering on the trajectory movement of Figure 4.6 based on connectivity kernel (4.4). (Left) The Affinity matrix (4.5). Same notations as Figures 4.2 and 4.4. (Right) Eigenvalues plot.

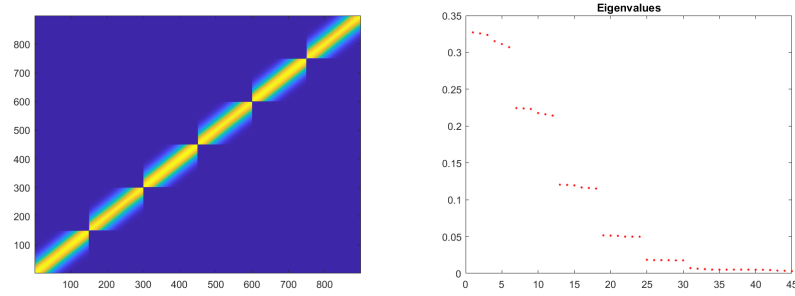Analogous to the previous case, we obtain a decomposition of the trajectory which splits velocity profiles in proximity to speed extrema: the eigenvectors extracted correspond to either accelerating or decelerating movement fragment coupled with a specific direction. Six distinct colours are used for the clusters identified by the eigenvectors (partly taken from the paper [95], Figure 5b). The eigenvectors identify a decomposition of movement into fragments consistent with the results expressed in [95] (Figure 4.8).
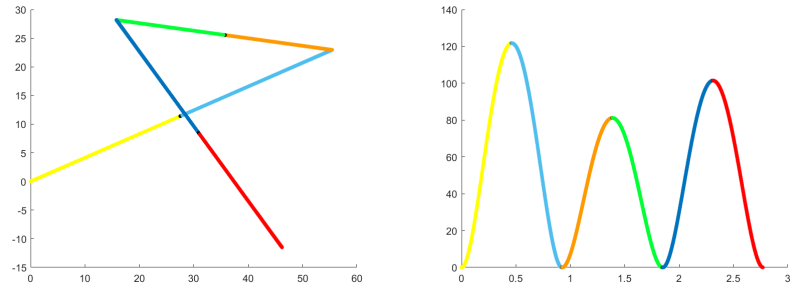
Figure 4.8: Global path and speed decomposition into fragments according to the spectral analysis of (4.5).

4.3.1.3   Test 3: simulation of Figure 1.8

In this test, we apply the spectral algorithm described in 4.2 on an approximate trajectory of Figure 1.8. The analyzed motion is represented in Figure 4.9.

In [95], the experiment performed by the monkey consists of reaching several targets one after the other. Here, a trajectory is extrapolated that starts from a fixed point (red point in Figure 4.9), arrives at a second target (blue point in Figure 4.9) and comes to an end. As before, the red dot identifies the starting point of the movement, but this

Figure 4.9: Reaching path and speed profile of a random target pursuit task: approximation of Figure 1.8. The red dot represents the movement starting position, while the blue one represents the first target to be reached.

time there is an intermediate target to be reached represented by a blue dot. This point corresponds in the velocity profile to a local minimum. There are also two local maxima having dist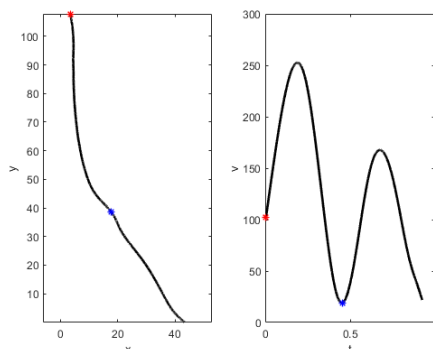inct velocity intensities. The kernel (4.4), which gives an estimate of the connectivity between the kinematic points of the trajectory, identifies an affinity matrix divided into four blocks (see Figure 4.10). Each block identifies an eigenvector that we project onto the motion trajectory (see Figure 4.11). The eigenvectors represented, are those associated with the largest eigenvalues shown in the right-hand graph of Figure 4.10.
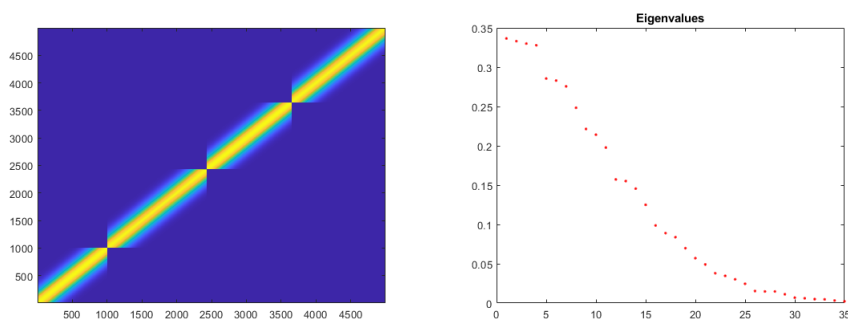
Figure 4.10: Spectral clustering. (Left) Affinity matrix over the simulated random target pursuit task of Figure 4.9. (Right) The eigenvalues plot. Note the first four eigenvalues: these are those associated with the eigenspaces of the four blocks of the affinity matrix.

This provides a partition of the trajectory into sub-trajectories, only using kinematic parameters. In order to compare these trajectories with trajectory fragments obtained in [95], we note that the values of movement direction θ and acceleration a are almost constant on the recovered sub-trajectories, and that neurons are invariant with respect
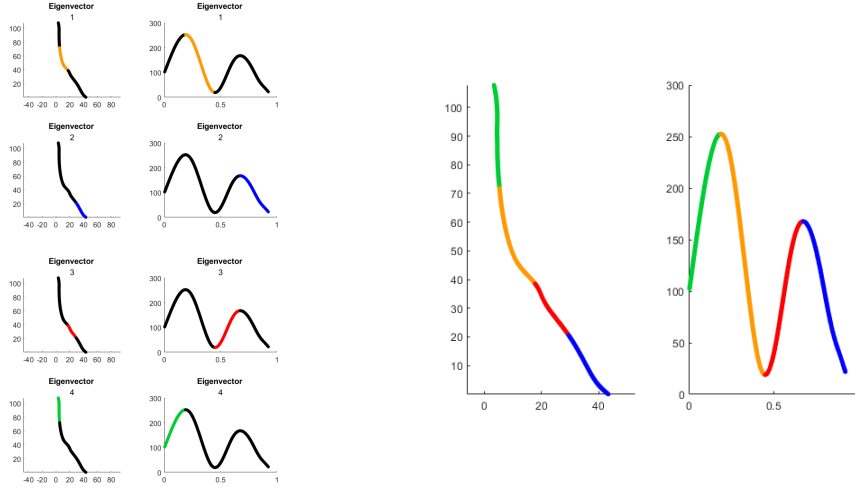
Figure 4.11: (a) Eigenvectors projections over the reaching trajectory. Eigenvectors identify acceleration and deceleration phases coupled with a movement direction within a specific time window. (b) Resulting movement decomposition into distinct trajectory fragments.

to time and position (e.g. [81], [95]). Hence we perform a new clustering with respect to the distance $d^{\mathcal{M}}$ restricted to the θ and a variables, in the space of sub-trajectories. The resulting clusters appropriately group acceleration and deceleration phases, as well as phases with constant direction. The eigenvectors colored in green denote the acceleration phase, those colored in orange the deceleration phase. The resulting decomposition pattern displayed in Figure 4.12 is in agreement with the experimental result of [95] shown in Figure 1.8.

In this test, we will also validate the choice of our distance by considering the same trajectory subjected to random noise. It is indeed common for neurons to be susceptible to changes in activity including errors. In Figure 4.13 we have represented random noise in terms of pairs of points and orientation, i.e. for each point (x, y) (outside the movement trajectory) we also represent its movement direction θ. The same applies to the plane (t, v), with orientation given by a. Despite the addition of noise, the clustering algorithm still recognizes the fragments encoded in the previous test. For simplicity, they were all colored red, but each represents a different cluster and the noise is considered a separate partition that does not affect the second space-time invariance grouping.

The usefulness of the sub-Riemannian distance lies in the fact that if two segments have different orientation angles, both in the (x, y) and (t, v) planes it succeeds in distinguishing them into two different clusters as the two segments belong to distinct parallel planes.

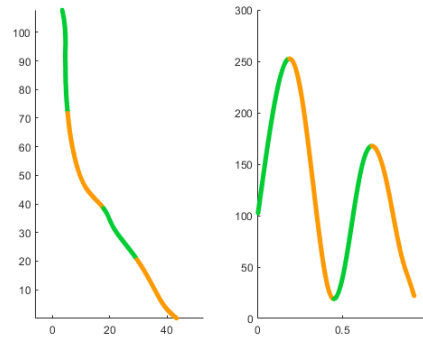Figure 4.12: Resulting reaching trajectory segmentation according to spatio-temporal invariant clusters. Acceleration and deceleration phases are respectively identified. . See Figure 1.8 for a direct comparison.
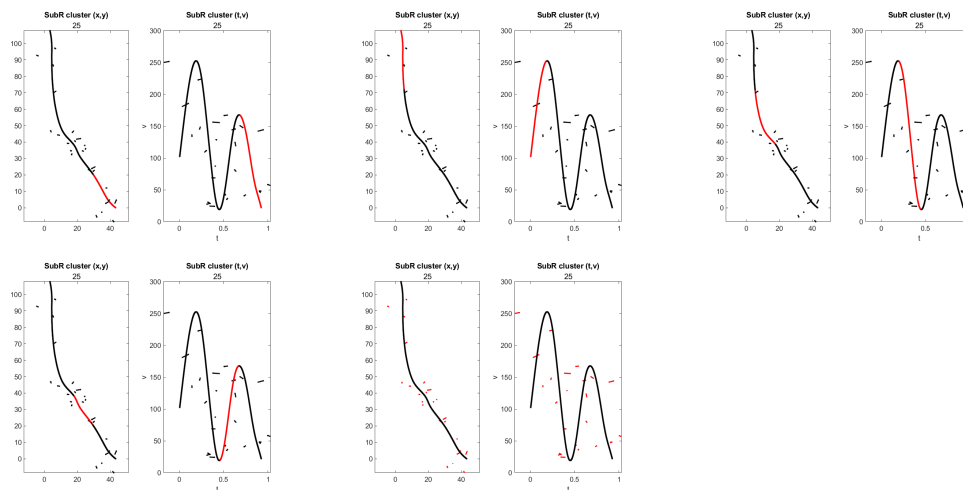
Figure 4.13: Spectral clustering over the reaching profile with the adding of noise. Each plot represents a cluster (red-colored) identified by the sub-Riemannian distance $d^{\mathcal{M}}$.

4.3.1.4   Test 4: simulation of Figure 1.9

Here we test the segmentation obtained through distance $d^{\mathcal{M}}$ over the random target pursuit task represented in Figure 1.9 (see [95]). This time, the path taken by the monkey's arm follows various changes in direction and speed, and the execution time is longer. Similarly to the previous test, we implement the clustering procedure on an approximation of Figure 1.9, shown in 4.14.
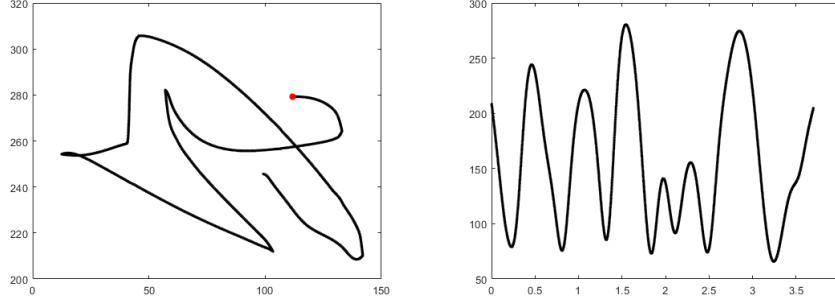
Figure 4.14: Reaching path and speed profile of a random target pursuit task: approximation of Figure 1.9. The red dot represents the movement starting position.

We discretize kernel (4.4) by applying it to the points of the trajectory in Figure 4.14. This first step identifies the affinity matrix represented in 4.15. The eigenvector analysis of the matrix leads, as in previous tests, to a segmentation of the global trajectory near the maxima and minima of the velocity profile. Clustering in eigenvectors corresponds to sub-trajectories, each of which encodes a phase of acceleration or deceleration and a constant direction of movement (see the blocks of the affinity matrix and Figure 4.16).
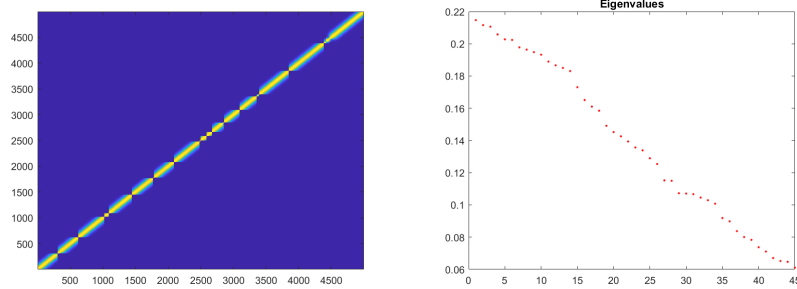
Figure 4.15: Affinity matrix (4.5) and eigenvalues plot.

After this step, we perform a second spectral clustering based on the distance $d^{\mathcal{M}}$ in the sub-trajectory space, using the variables (θ, a) only. In agreement with the neural states caught from article [95], the decomposition obtained (see Figure 4.17) codes for

transitions occurring in proximity to speed extrema, and the eigenvectors are associated with either accelerating or decelerating segments coupled with similar directional selectivity. To facilitate the comparison, we used the same color-coding of Figure 1.9. In this second grouping, the first eigenvector (orange-colored) embodies deceleration states for movements which go "down to the right". The green-colored eigenvector encodes for acceleration phases with movements still "down to the right" directed. The third eigenvector (violet-colored) codes for accelerating phases with movement directions which are mostly "up to the left" directed, belonging to the second quadrant. The blue-colored eigenvector retains deceleration phases with movement paths belonging to the second quadrant.
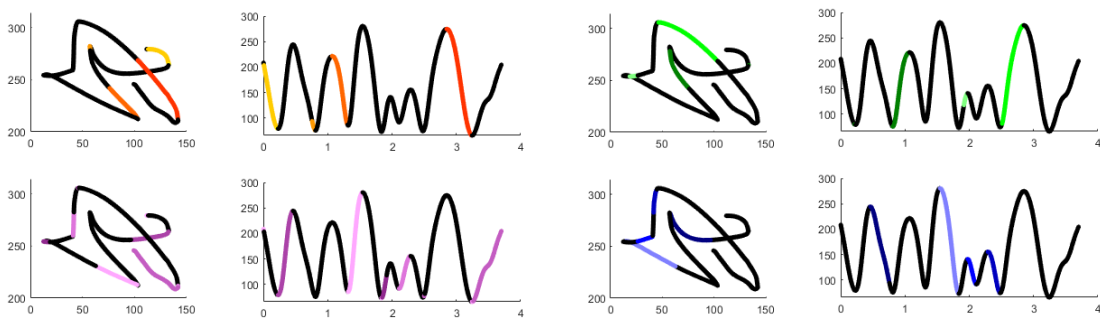
Figure 4.16: Eigenvectors projections over the reaching trajectory. Distinct colors are used to represent the sub-trajectories extracted from the first clustering. The subdivision of sub-trajectories into four groups comes from the second clustering based on distance $d^{\mathcal{M}}$ over the (θ, a) variables.
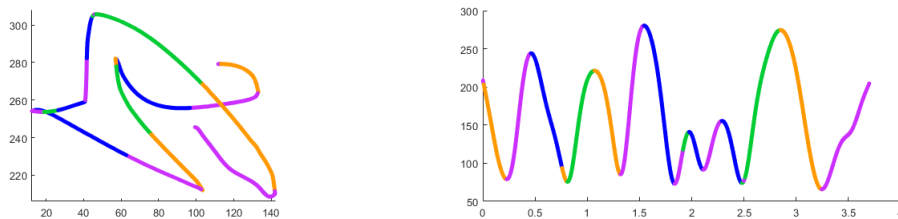
Figure 4.17: Global path and speed decomposition using distance $d^{\mathcal{M}}$ across the clustering steps. The clusters of movement fragments are shown in orange, green, violet and blue as representatives of the groups depicted in Figure 4.16. See Figure 1.9 for a direct comparison.

These clustering steps allow us to classify movement fragments based on a choice of a space of kinematic variables that are encoded in the cortex and a connectivity kernel. In particular, we emphasize that by working only on kinematic variables we recover

the same neural classification acquired by electrode array. Hence, we argue that the distance $d^{\mathcal{M}}$ is adequate, not only because of the properties of the kinematic space, but also because of the classification in sub-trajectory fragments given by the clustering algorithm, which has a neural foundation. We emphasize how instead the distances tested in the paper [95] (see the list recalled in 1.3.1) did not justify the classification results into movement trajectories. We therefore introduced a distance that allows to perform a kernel component analysis which is the phenomenological counterpart of the neural PCAs provided by Kadmon Harpaz et al [95].

Chapter 5

A model of reaching via sub-Riemannian geodesics

In this Chapter, we propose a model of arm reaching movements expressed in terms of geodesics in the subriemannian space we set up in Chapter 3. We will choose a set of kinematic variables to which motor cortical cells are selective with the purpose of modelling the specific task of reaching. Minimizing trajectories will be recovered as suitable geodesics of the geometric spaces arising from the selective behaviour of M1 neurons. We will then extend this model by including the direction of arm movement. On this set, we will define a suitable sub-Riemannian metric able to provide a geometric interpretation of two-dimensional task-dependent arm reaching movements.

The structure of the Chapter is the following. In section 5.1 we develop our model of reaching through the analysis of admissible geodesics. Section 5.2 presents part of the results where we provide a geometric interpretation of some task-dependent arm reaching movements.

5.1 Admissible geodesics for reaching tasks

The goal of this section is to develop a model inspired by the neurogeometrical and phenomenological frames recalled in Chapter 1 (sections 1.2, 1.4) and Chapter 3 to describe reaching tasks. Starting from optimal arm reaching trajectories of Flash and Hogan model (recalled in section 1.4.2), we will lift the problem in the higher dimensional geometric structure introduced in 3.2 and 3.3. In this setting, the functional (1.15) will become an energy functional, whose minima coincide with geodesics. In section 5.1.2, we will refer to the sub-Riemannian geometry set in section 3.3 by analyzing a special case of the associated geodesics problem. These curves will allow a wider variety of reaching movements to be represented.

5.1.1 Kinematic model of 1D motions

In this section, we express the functional introduced by Flash and Hogan in terms of the sub-Riemannian jet space introduced in section 3.2. Minima of functional (1.15) will coincide with geodesics in this space. We will be interested in curves which are lifting of mono-dimensional trajectories. This property will lead to consider only curves in the family of horizontal ones having a non vanishing component along the vector field X_1. We also refer to [12] for a similar nonholonomic system for modelling human locomotion.

We will then define admissible curves, as follows

Definition 5.1. A curve $\gamma : [0,T] \to \mathcal{J}^2$ is called admissible if it is of the form

$$\dot{\gamma}(t) = X_1 + j(t) X_2. \tag{5.1}$$

Here, the function $t \mapsto j(t)$ represents the magnitude of jerk, the rate of change of acceleration.
If we choose a metric on the distribution D which makes X_1 and X_2 orthonormal, the length functional on admissible curves reduces to

$$l(\gamma) = \int_0^T \sqrt{1 + j^2(t)}\, dt. \tag{5.2}$$

We propose here this new functional as a good model for voluntary arm reaching movements, since it provides the same solutions as the one presented in [60]. Indeed, its associated energy functional is

$$E(\gamma) = \frac{1}{2} \int_0^T \left(1 + j^2(t)\right) dt. \tag{5.3}$$

Since $j(t) = \dddot{x}(t)$ on a lifted curve, there is a strong relation between this functional and the one proposed by Flash and Hogan (1.15). In order to be able to compare, we will give some geometric properties of the model.

Remark 5.1. As outlined in section 2.3.2, there could exist minimizers of the length functional which are not solution of the associated hamiltonian system. Sussmann in [144] provided a technique for producing abnormal extremals of arbitrary sub-Riemannian structures on four-dimensional manifolds having a two-dimensional bracket-generating distribution. This result can be applied to our settings, implying that integral curves of the vector field X_2 are singular geodesics. Also Byant and Hsu (see [29], Propositions 2.1 and 3.2) explicitly computed their non regularity in the Engel group. Moreover, integral curves of X_2 are the only singular curves that can be found. Consequently, admissible geodesics on this setting are non singular.

5.1.1.1 Normal geodesics in the two-jets bundle

Below we will look at some properties of normal geodesics that will be useful in analyzing the admissible ones. Since we are in a Lie group, it is not restrictive to consider geodesics starting from the origin, and obtain all the others by applying the action of the group.

Proposition 5.1. *A normal geodesic γ starting from 0 is a solution of the following ODE:*

$$\gamma' = \left(vp_x + a(-p_x t + p_v(0)) + p_t \right) X_1 + \left(p_x \frac{t^2}{2} - p_v(0)t + p_a(0) \right) X_2 = \qquad (5.4)$$

$$= p_t X_1 + p_a(0) X_2 + p_v(0)(aX_1 - tX_2) + p_x \left(vX_1 - atX_1 + \frac{t^2}{2} X_2 \right),$$

for suitable real constants $p_t, p_x, p_v(0), p_a(0)$.

Proof. As recalled in Proposition 2.7, normal geodesics solve a ODE system expressed in terms of the cotangent coordinates $(t, x, v, a, p_t, p_x, p_v, p_a) \in T^* \mathcal{J}^2$. Since we chose a metric which makes X_1, X_2 orthonormal, the Hamiltonian governing the sub-Riemannian geodesic flow on $\mathcal{J}^2$ is

$$H = \frac{1}{2} \left((vp_x + ap_v + p_t)^2 + p_a^2 \right), \qquad (5.5)$$

whose normal geodesic equations are expressed by

$$\begin{cases} p_t' = & 0 \\ p_x' = & 0 \\ p_v' = & -p_x \left(vp_x + ap_v + p_t \right) \\ p_a' = & -p_v \left(vp_x + ap_v + p_t \right) \\ t' = & vp_x + ap_v + p_t \\ x' = & v \left(vp_x + ap_v + p_t \right) \\ v' = & a \left(vp_x + ap_v + p_t \right) \\ a' = & p_a. \end{cases} \qquad (5.6)$$

In this way, for the dual variables it holds

$$p_t = p_t(0), \quad p_x = p_x(0), \quad p_v' = -p_x t', \quad p_a' = -p_v t' = p_x t t' - p_v(0)t',$$

so that

$$p_v = -p_x t + p_v(0), \quad p_a = p_x \frac{t^2}{2} - p_v(0)t + p_a(0). \qquad (5.7)$$

In addition,

$$vp_x + ap_v + p_t = vp_x + a(-p_x t + p_v(0)) + p_t. \tag{5.8}$$

As a consequence, the equation satisfied by the observed variables reduces to

$$\gamma' = (vp_x + ap_v + p_t) X_1 + p_a X_2 =$$

$$\left(vp_x + a\left(-p_x t + p_v(0)\right) + p_t \right) X_1 + \left(p_x \frac{t^2}{2} - p_v(0)t + p_a(0) \right) X_2.$$

$\square$

Proposition 5.2. *A geodesic γ starting from 0 solution of ODE (5.6) is a horizontal curve. If we call α_1 and α_2 the coefficients of X_1 and X_2, respectively, we have*

$$\gamma' = \alpha_1 X_1 + \alpha_2 X_2,$$

with $\alpha_1^2 + \alpha_2^2 = C$, where C is a strictly positive constant.

Proof. Starting from geodesics equation (5.4) we immediately obtain that

$$\frac{d\alpha_1^2}{ds} = 2\alpha_1 \alpha_1' = 2\alpha_1 (v'p_x + a'p_v + ap_v') = 2\alpha_1 p_a p_v = -2p_a p_a' = -\frac{d\alpha_2^2}{ds}.$$

$\square$

Proposition 5.3. *If a geodesic γ connecting two points 0 and ξ_1 in the interval $[0, T]$ is represented as in the previous proposition, then*

$$l(\gamma) = T\sqrt{(\alpha_1^2 + \alpha_2^2)}.$$

5.1.1.2   Admissible geodesics for center-out movements

The kinematic properties of one dimensional motions do not depend on the movement direction. Here, we propose how one dimensional movements, which can accordingly reflect a center-out reaching task, are realized by means of admissible geodesics in the 2-jet structure considered.

Therefore, we need to restrict the study of geodesics which are admissible curves. In particular, it is no more clear if the connectivity property still holds true. We will fix an initial value set to the origin, $t(0) = x(0) = v(0) = a(0) = 0$, arbitrary final values $(x_1, v_1, a_1) \neq (0, 0, 0)$ and we will show the existence of an admissible curve γ connecting them. We remark that the time T defined in the functional (5.2) is free a priori. However, in the case of connecting two points of the space with an admissible curve, the arrival time is automatically fixed. Therefore, below we will assume to fix the final time and, without loss of generality, set it equal to 1.

Proposition 5.4. *If we fix the initial value $\xi_0 = (t_0, x_0, v_0, a_0) = \vec{0}$ and an arbitrary final value $\xi_1 = (1, x_1, v_1, a_1)$, then there exist coefficients e_0, e_1, e_2 such that*

$$\dot{\gamma}(t) = X_1 + (e_0 + e_1 t + e_2 \frac{t^2}{2})X_2$$

satisfies $\gamma(0) = \xi_0$ and $\gamma(1) = \xi_1$.

Proof. It is a direct computation that the expression

$$\gamma'(s) = X_1(\gamma(s)) + \left(e_0 + e_1 t(s) + e_2 \frac{t^2(s)}{2} \right) X_2(\gamma(s))$$

implies $t' = 1$, so that we can identify the evolution parameter s with the time parameter t and replace the tangent vector γ' with the classical $\dot{\gamma}$. For the other components of $\dot{\gamma}$ it holds

$$\begin{cases} \dot{x} = & v \\ \dot{v} = & a \\ \dot{a} = & e_0 + e_1 t + e_2 \frac{t^2}{2}. \end{cases} \tag{5.9}$$

By integrating (5.9) and imposing the boundary conditions $\gamma(0) = 0$ and $\gamma(1) = \xi_1$, the matrix of coefficients D of the linear integrated system (5.9) is invertible, hence proving a direct connectivity result.

$\square$

Consequently, it is possible to define a distance referred to admissible curves:

$$d_a(\xi_0, \xi_1) = \inf \{l(\gamma) : \gamma \text{ is an admissible curve connecting } \xi_0 \text{ and } \xi_1\}, \tag{5.10}$$

where $(\xi_0, \xi_1) = ((0, 0, 0, 0), (1, x_1, v_1, a_1))$.

Let us first estimate this distance in terms of the classical Carnot Carathéodory distance d:

Proposition 5.5. *If $(\xi_0, \xi_1) = ((0, 0, 0, 0), (1, x_1, v_1, a_1))$, then*

$$d(\xi_0, \xi_1) \leqslant d_a(\xi_0, \xi_1). \tag{5.11}$$

In addition, $d_a(0, \xi_1) \leqslant k \|D^{-1}\| |\xi_1|$, where k is an absolute constant and D is the matrix associated to the integrated system (5.9).

Proof. The first assertion immediately follows from the definition, whereas for the second one we have

$$d_a(0, \xi_1) \leqslant \int_0^1 \sqrt{1 + \left(e_0 + e_1 t + e_2 \frac{t^2}{2} \right)^2} \, dt \leqslant k \|D^{-1}\| (1 + |a_1| + |v_1| + |x_1|).$$

$\square$

Of course it is not clear if the minimum is achieved or not. However, it exists at any time a (horizontal) curve which is admissible.

In the following, we will prove that the minimum is attained.

Remark 5.2. A common strategy to show the existence of minimum for the length functional is to study the same problem for the associated energy functional. Indeed, from Montgomery [114], it is proved that for a fixed time T, length functional minimizers parameterized with constant speed coincide with those of the energy functional. However, in this context we cannot directly apply this proposition, since the set on which the minimum is computed is different (see Equation 5.10).

Proposition 5.6. *In a compact neighbourhood of the origin, there exists a minimal admissible curve (i.e. an admissible geodesic) connecting two points 0 and $\xi_1 = (1, x_1, v_1, a_1)$.*

Proof. Let us consider the length functional $l(\gamma) = \int_0^1 \sqrt{1 + j(t)^2}\, dt$ with boundary values $\gamma(0) = 0$, $\gamma(1) = \xi_1$ and take a minimizing succession γ_n connecting 0 and ξ_1 such that $l(\gamma_n) \to \inf l$. As the functional is uniformly bounded, by Ascoli-Arzelà theorem there exists a sub-succession γ_{n_j} which uniformly converges to a curve γ joining 0 and ξ_1. Hence, by the semi-continuity of the length integral it holds $l(\gamma) \leqslant \liminf_j l(\gamma_j)$, from which it follows that the minimum is attained. $\qquad\square$

Remark 5.3. Admissible curves are regular (see Remark 5.1) and hence normal (see Theorem 2.10), this means that we can search for admissible geodesics through system (5.6). Moreover, it is possible to explicitly find admissible curves solutions of (5.6) in a neighbourhood of the origin.

Let us assume that $t(0) = x(0) = v(0) = a(0) = 0$. For every $p_t > 0$, there exist a $\delta > 0$ and $T > 0$ such that, for every p_x, p_v, p_a satisfying $|p_x|, |p_v|, |p_a| \leqslant \delta$, the geodesic found in Proposition 5.1 is an admissible geodesic for every $t \leqslant T$.

Since we are assuming $v(0) = a(0) = 0$ and p_t is a strictly positive constant, the function h defined by $h(s) = p_t + v(s)\, p_x + a(s)\, p_v(s)$ is different from 0 in a neighbourhood of the origin. Following the approach used in [24] for the study of geodesics in jet spaces, we make a reparameterization of system (5.6) by considering the change of variable $\frac{\mathrm{d}}{\mathrm{d}t} = \frac{1}{h(s)} \frac{\mathrm{d}}{\mathrm{d}s}$, so that

$$\dot{p}_a := \frac{\mathrm{d}p_a}{\mathrm{d}t} = -p_v, \quad \dot{p}_v = -p_x, \quad \dot{p}_x = 0, \quad \dot{p}_t = 0. \tag{5.12}$$

It is therefore immediate that p_a is a polynomial of degree two in the variable t. Moreover, since

$$\dot{h} = \frac{p_a p_v}{h} = -\frac{p_a \dot{p}_a}{h}, \quad \text{we get that} \quad (\dot{h^2}) = -(\dot{p_a^2}).$$

In this way, $h^2 + p_a^2 = p_t^2 + p_a(0)^2$ in a neighbourhood of the origin. As a consequence, we can express h as a function of p_a, for every t such that $p_t^2 + p_a(0)^2 - p_a(t)^2 \geqslant 0$, which

means for every t such that

$$p_t^2 + p_a(0)^2 - (p_x \frac{t^2}{2} - p_v(0)t + p_a(0))^2 \geqslant 0. \tag{5.13}$$

We will choose T as the largest value of t for which (5.13) is satisfied. For such values of t, we can express h as $h(t) = \sqrt{p_t^2 + p_a(0)^2 - p_a^2(t)}$. We therefore obtain

$$\dot{a} := \frac{\mathrm{d}a}{\mathrm{d}t} = \frac{p_a(t)}{\sqrt{p_t^2 + p_a(0)^2 - p_a^2(t)}}. \tag{5.14}$$

Through (5.12) and (5.14), system (5.6) is integrable and the associated solution is an admissible curve.

Remark 5.4. If we fix the same boundary conditions expressed in Flash and Hogan model (see Figure 1.13 in 1.4.2), from a qualitative study of (5.14), we can already have a representation of the computed trajectories (see e.g. Figure 5.1). Indeed, by considering a movement which starts and ends at null velocity and acceleration, since the sign of $\dot{a}$ solely depends on p_a which is a polynomial of degree 2, we get an acceleration profile which has three distinct zeros and one sign change. Hence the bell-shaped speed profile is recovered.

Proposition 5.7. *The energy functional E defined in (5.3) attains its infimum on the set of minimal admissible geodesics.*

Proof. Following the same approach used for example in [114], if we call σ an admissible curve between 0 and ξ_1, by Cauchy-Schwarz inequality we get

$$l(\sigma)^2 = \left(\int_0^1 1 \cdot \|\dot{\sigma}(t)\| \, dt \right)^2 \leqslant \int_0^1 \|\dot{\sigma}(t)\|^2 \, dt = 2E(\sigma), \tag{5.15}$$

where equality holds if and only if $\|\dot{\sigma}(t)\|$ is constant. From Proposition 5.6, we know there exists a minimal admissible geodesic γ joining 0 and ξ_1, from which we obtain that

$$E(\gamma) = \frac{l(\gamma)^2}{2} \leqslant \frac{l(\sigma)^2}{2} \leqslant E(\sigma).$$

Therefore, for every minimizing admissible geodesic γ and any admissible curve σ, we get $E(\sigma) \geqslant E(\gamma)$. The equality $l(\gamma)^2 = l(\sigma)^2$ can hold if and only if σ is also a geodesic. So, unless σ is also an admissible geodesic, we have $E(\gamma) < E(\sigma)$. Finally, since admissible geodesics are normal, it holds $E(\gamma) = \frac{l(\gamma)^2}{2}$ proving that E really attains the infimum in $\frac{d_a^2}{2}$. $\qquad\square$

We have proved that the length and energy functionals have (up to a constant) the same minima also for the family of admissible curves. In this way, we are truly reduced to analyze the functional studied by Flash and Hogan.

We modelled as admissible geodesics those center-out movements whose kinematic properties are in accordance with the ones experimentally observed in the physical space. Moreover, singular geodesics would exactly interpret those "non-admissible" physical reaching trajectories, since they would be obtained by varying arm's acceleration without changing arm's velocity, nor position.

5.1.2   Kinematic model of 2D motions

We now refer to the geometrical setting described in section 3.3, from which we will extend the previous model of reaching by including two-dimensional movement trajectories. Let us now arrange the Hamiltonian setting which allows to analyze the set of normal geodesics.

Definition 5.2. Let $(X_i)_{i=1}^3$ be the vector fields (3.20). The fiber-linear functions on the cotangent bundle $P_{X_i} : T^*\mathcal{M} \to \mathbb{R}$ defined by $P_{X_i}(\eta, p) = p(X_i(\eta))$ are called the momentum functions for X_i.

In terms of cotangent coordinates $(x, y, t, \theta, v, a, p_x, p_y, p_t, p_v, p_\theta, p_a) \in T^*\mathcal{M}$ we can write

$$P_{X_1} = v \cos \theta p_x + v \sin \theta p_y + a p_v + p_t, \quad P_{X_2} = p_\theta, \quad P_{X_3} = p_a. \qquad (5.16)$$

Since we have selected on the distribution $D^\mathcal{M}$ the metric $g^\mathcal{M}$ which makes $(X_i)_{i=1}^3$ orthonormal, the Hamiltonian function (see Proposition 2.7) simply reduces to the sum of squares of the momentum functions relative to the frame $(X_i)_{i=1}^3$. We therefore enunciate the following

Proposition 5.8. ([114]). *The Hamiltonian governing the sub-Riemannian geodesic*

flow on $\mathcal{M}$ is $H = \frac{1}{2}\left(P_{X_1}^2 + P_{X_2}^2 + P_{X_3}^2\right)$ and the normal geodesic equations are given by

$$
\begin{cases}
p'_x & = 0 \\
p'_y & = 0 \\
p'_t & = 0 \\
p'_v & = -\left(\cos\theta p_x + \sin\theta p_y\right)\left(v\left(\cos\theta p_x + \sin\theta p_y\right) + ap_v + p_t\right) \\
p'_\theta & = v\left(\sin\theta p_x - \cos\theta p_y\right)\left(v\left(\cos\theta p_x + \sin\theta p_y\right) + ap_v + p_t\right) \\
p'_a & = -p_v\left(v\left(\cos\theta p_x + \sin\theta p_y\right) + ap_v + p_t\right) \\
x' & = v\cos\theta\left(v\left(\cos\theta p_x + \sin\theta p_y\right) + ap_v + p_t\right) \\
y' & = v\sin\theta\left(v\left(\cos\theta p_x + \sin\theta p_y\right) + ap_v + p_t\right) \\
t' & = \left(v\left(\cos\theta p_x + \sin\theta p_y\right) + ap_v + p_t\right) \\
v' & = a\left(v\left(\cos\theta p_x + \sin\theta p_y\right) + ap_v + p_t\right) \\
\theta' & = p_\theta \\
a' & = p_a.
\end{cases}
\tag{5.17}
$$

Our purpose will be to identify suitable subsets of normal geodesics in order to provide a phenomenological description for some relevant task-reaching movements.

5.1.2.1 Admissible geodesics: reaching targets with prescribed directions

In this section we will model a cognitive reaching task in which it is required to grasp a target in a specific hand orientation, knowing the initial hand configuration. We claim that the lifted curves of the space could represent the arm reaching trajectories, and, as we did for center-out reaching movements, we will consider integral curves of the horizontal distribution with a non vanishing component along the vector field X_1.

We will then look for admissible curves, as follows

Definition 5.3. A curve $\gamma : [0,1] \rightarrow \mathcal{M}$ is called admissible if it is of the form

$$
\dot{\gamma}(t) = X_1 + k\left(t\right)X_2 + j\left(t\right)X_3.
\tag{5.18}
$$

Here, the function $t \mapsto k\left(t\right)$ represents the Euclidean curvature over the path (x,y), whereas the function $t \mapsto j\left(t\right)$ describes the rate of change of acceleration.

We then search for admissible curves joining arbitrary couples of points in the cortical feature space $\mathcal{M}$.

Proposition 5.9. *If we fix a constant $k \in \mathbb{R}$ and we consider arbitrary values $(\eta_0, \eta_1) = ((0, x_0, y_0, \theta_0, v_0, a_0), (1, x_1, y_1, \theta_1, v_1, a_1)) \in \mathcal{M}$, then there exist constant coefficients j_0, j_1, j_2, j_3 such that*

$$\dot{\gamma}(t) = X_1 + kX_2 + \left(j_0 + tj_1 + j_2\frac{t^2}{2} + j_3\frac{t^3}{3!}\right)X_3 \qquad (5.19)$$

satisfies $\gamma(0) = \eta_0$ *and* $\gamma(1) = \eta_1$.

Proof. Analogously to Proposition 5.4, equation (5.19) sets up system

$$\begin{cases} \dot{x} & = v(t)\cos(\theta(t)) \\ \dot{y} & = v(t)\sin(\theta(t)) \\ \dot{\theta} & = k \\ \dot{v} & = a(t) \\ \dot{a} & = j_0 + j_1 t + j_2\frac{t^2}{2} + j_3\frac{t^3}{3!} \end{cases} \qquad (5.20)$$

which can be explicitly integrated. By imposing initial and final conditions for the joining of points η_0, η_1, the integrated equations give rise to a linear system in the variables $(j_i)_{i=0}^3$. It is a direct computation to verify that the matrix associated to the integrated system is invertible and hence to prove the existence of coefficients $(j_i)_{i=0}^3$ for equation of (5.19). □

Thanks the connectivity property above exposed, it is possible to define a distance referred to admissible curves in the connected space $\mathcal{M}$:

$$d_a^{\mathcal{M}}(\eta_0, \eta_1) = \inf\{l(\gamma) : \gamma \text{ is an admissible curve connecting } \eta_0 \text{ and } \eta_1\}, \qquad (5.21)$$

where $(\eta_0, \eta_1) = ((0, x_0, y_0, \theta_0, v_0, a_0), (1, x_1, y_1, \theta_1, v_1, a_1)) \in \mathcal{M}$ and the length l is given by

$$l(\gamma) = \int_0^1 \sqrt{1 + k^2(t) + j^2(t)}\, dt, \qquad (5.22)$$

with γ solution of (5.18).

For reader convenience, we outline that the energy functional on admissible curves in $\mathcal{M}$ reduces to

$$E(\gamma) = \frac{1}{2}\int_0^1 \left(1 + k^2(t) + j^2(t)\right) dt. \qquad (5.23)$$

We can directly observe that for constant movement directions, the functional (5.23) reduces to the functional (5.3) of Flash and Hogan.

Now we will show that admissible curves can be found as solutions of system (5.17). To do so, we will prove that admissible curves are regular, in the sense of Definition 2.27.

As recalled in section 2.3.2, L. Hsu gave a characterization for a curve to be regular by means of the holonomy map (see Definition 2.26) and G. Giovannardi proved a criterion for identifying singular curves (Theorem 2.9). By applying these results to our case, we verify that even if we considered the whole sub-Riemannian setting, integral curves of X_2 or X_3 (those whose directions point along the fiber) are singular (see Remark 5.5 and 5.6 for the computations). We prove the regularity of admissible curves in Remark 5.7.

Remark 5.5. Let $\gamma : [0, 1] \to \mathcal{M}$ be an integral curve of the vector field X_3. Then γ is singular.

Proof. After splitting X_3 along γ in its horizontal and vertical part

$$X_{3_H} = \sum_{i=1}^{3} v_{H_i} X_i \quad , \quad X_{3_V} = \sum_{j=4}^{6} v_{V_j} X_j, \tag{5.24}$$

a direct computation shows that the admissibility system expressed through the matrix form (2.14) is given by

$$V_V'(s) = -A(s) \begin{pmatrix} v_{H_1}(s) \\ v_{H_2}(s) \\ v_{H_3}(s) \end{pmatrix}, \quad \text{where} \quad A = \begin{pmatrix} 0 & 0 & 0 \\ 1 & 0 & 0 \\ 0 & 0 & 0 \end{pmatrix} \tag{5.25}$$

for $v_{H_1}, v_{H_2}, v_{H_3} \in C_0^1((0, 1))$. Then the image of the holonomy map (2.26) is equal to

$$V_V(1) = \begin{pmatrix} 0 \\ -\int_0^1 v_{H_1}(s)\, ds \\ 0 \end{pmatrix}, \tag{5.26}$$

from which we deduce that the holonomy map is not surjective. Hence γ is singular. $\square$

Remark 5.6. A horizontal curve $\gamma : [0, 1] \to \mathcal{M}$ solution of $\gamma' = k(s) X_2 + j(s) X_3$, where k and j are different from zero, is singular.

Proof. As before, a straightforward computation reveals that the matrices A and B of the admissibility system (2.14) are given by

$$A = \begin{pmatrix} -k(s) & 0 & 0 \\ j(s) & 0 & 0 \\ 0 & 0 & 0 \end{pmatrix} \quad B = \begin{pmatrix} 0 & 0 & -\frac{k(s)}{v(s)} \\ 0 & 0 & 0 \\ k(s)\, v(s) & 0 & 0 \end{pmatrix}. \tag{5.27}$$

To prove the singularity of γ, we will apply Theorem 2.9. We will verify if there exists a row vector field $\Lambda(s) \neq 0$ for all $s \in [0, 1]$ that solves system (2.15). Since it must hold $\Lambda A = 0$, if Λ is of the form $\Lambda(s) = (\lambda_1(s), \lambda_2(s), \lambda_3(s))$, then

$$-k(s)\lambda_1(s) + j(s)\lambda_2(s) = 0. \tag{5.28}$$

Hence,

$$\Lambda B = \begin{pmatrix} \lambda_1, & \lambda_2, & \lambda_3 \end{pmatrix} \begin{pmatrix} 0 & 0 & -\frac{k(s)}{v(s)} \\ 0 & 0 & 0 \\ k(s)\, v(s) & 0 & 0 \end{pmatrix} = \begin{pmatrix} \lambda_3 k(s)\, v(s), & 0, & -\lambda_1 \frac{k(s)}{v(s)} \end{pmatrix}, \tag{5.29}$$

which implies that

$$\begin{cases} \lambda_1'(s) &= \lambda_3(s)\,k(s)\,v(s) \\ \lambda_2'(s) &= 0 \\ \lambda_3'(s) &= -\lambda_1(s)\,\frac{k(s)}{v(s)}. \end{cases} \qquad (5.30)$$

Consequently, λ_2 is constant and from (5.28) and (5.30) we can integrate λ_3. Therefore, for any choice of $\lambda_2 \neq 0$, we find a row vector Λ solution of (2.15) whose components are not null. The curve γ is therefore singular. $\qquad\square$

Remark 5.7. The admissible curve $\gamma : [0,1] \to \mathcal{M}$ solution of $\gamma' = X_1 + k(s)X_2 + j(s)X_3$ is regular.

Proof. In this case, the matrices of system (2.14) are

$$A = \begin{pmatrix} -k(s) & 1 & 0 \\ j(s) & 0 & 1 \\ 0 & 0 & 0 \end{pmatrix} \quad B = \begin{pmatrix} \frac{a(s)}{v(s)} & 0 & -\frac{k(s)}{v(s)} \\ 0 & 0 & 0 \\ k(s)\,v(s) & -1 & 0 \end{pmatrix}.$$

Then, as in the previous remark, we look for a row vector field $\Lambda \neq 0$ which solves system (2.15). Since it must be $\Lambda A = 0$, we have that Λ is of the form $\Lambda(s) = (0,0,\lambda(s))$. Hence,

$$\Lambda B = \begin{pmatrix} 0, & 0, & \lambda(s) \end{pmatrix} \begin{pmatrix} \frac{a(s)}{v(s)} & 0 & -\frac{k(s)}{v(s)} \\ 0 & 0 & 0 \\ k(s)\,v(s) & -1 & 0 \end{pmatrix} = \begin{pmatrix} \lambda(s)\,k(s)\,v(s), & -\lambda(s), & 0 \end{pmatrix}.$$

This means that $\lambda'(s) = 0$ and $\lambda(s) = 0$, therefore the unique solution to system (2.15) is $\Lambda \equiv 0$. This enables to conclude that admissible curves are regular. $\qquad\square$

Through Remark 5.7 we have proved that admissible curves are regular, therefore solutions of the hamiltonian system (5.17), as stated by Theorem 2.10. As we did in Remark 5.3 in section 5.1.1.2, we can explicitly represent solutions of (5.6) which are admissible in a neighbourhood of the origin (see Remark 5.8).

Remark 5.8. Let us assume that $\eta_0 = \vec{0} \in \mathcal{M}$. For every $p_t > 0$, there exist a constant k, a $\delta > 0$ and $T > 0$ such that, for every $p_x, p_y, p_\theta, p_v, p_a$ satisfying $|p_x|, |p_y|, |p_\theta|, |p_v|, |p_a| \leqslant \delta$, the solution of system (5.17) is an admissible geodesic for every $t \leqslant T$. We define the function $\psi(s) = v(s)\,(\cos(\theta(s))\,p_x + \sin(\theta(s))\,p_y) + a(s)\,p_v(s) + p_t$ and we parameterize the equations with respect to t by setting $\frac{\mathrm{d}}{\mathrm{d}t} = \frac{1}{\psi(s)}\frac{\mathrm{d}}{\mathrm{d}s}$. Since we assumed $v(0) = a(0) = \theta(0) = 0$ and $p_t > 0$, the function ψ is strictly positive and $p_\theta \sim k$ in a neighbourhood of the origin. Hence, the function p_a is a polynomial of degree two in the variable t in a neighbourhood of η_0. Moreover, since $\dot\psi = -\frac{1}{\psi}(p_\theta \dot p_\theta + p_a \dot p_a)$, we obtain that

$\psi^2 + p_\theta^2 + p_a^2 = p_t^2 + k^2 + p_a(0)$. We can therefore express ψ as a function of p_θ, p_a for every t such that

$$p_t^2 + k^2 + p_a(0)^2 - p_\theta(t)^2 - p_a(t)^2 \geqslant 0. \tag{5.31}$$

By choosing T as the largest value of t for which 5.31 is satisfied, we can express ψ as $\psi(t) = \sqrt{p_t^2 + k^2 + p_a(0)^2 - p_\theta(t)^2 - p_a(t)^2}$, for every $t \leqslant T$. We therefore obtain

$$\dot{\theta}(t) = \frac{p_\theta(t)}{\sqrt{p_t^2 + k^2 + p_a(0)^2 - p_\theta(t)^2 - p_a(t)^2}}, \; \dot{a}(t) = \frac{p_a(t)}{\sqrt{p_t^2 + k^2 + p_a(0)^2 - p_\theta(t)^2 - p_a(t)^2}}.$$

Remark 5.9. The same techniques used in 5.1.1.2 (see Proposition 5.6 and 5.7) can be applied to prove that the inf in (5.21) is a minimum and that minimizing sets for the energy and length functional coincide. In this way, it is still possible to consider admissible geodesics for the space $\mathcal{M}$.

Admissible curves in the fiber bundle structure are those that allow to move from one fiber to another. We point out how the choice of variables is based on neurophysiological and physiological findings. Indeed, θ and a are the variables engrafted in the motor cortex, while the kinematic variables describe movement in the external world space.

5.1.2.2   Geodesics between sets

In this section, we will analyze a more general situation. Indeed, we would like to model the circumstance where the object to be reached does not require a particular orientation with which to be grasped, or it is indifferent how to grasp it in terms of acceleration. In this case we will impose that the second extreme of the geodesic belong to a set. As a result the movement trajectory will be defined as the minimizing geodesic between two a priori known sets, obtained by fixing the $(x, y, t, v) \in \mathbb{R}^4$ components and by varying the directions and accelerations $(\theta, a) \in S^1 \times \mathbb{R}$ variables. This method is the same adopted by B. Franceschiello in [62] for the modeling of illusory contours in the visual system. Below we will show the main definitions and statements.

Definition 5.4. Let $F_0 \subset \mathcal{M}$ be a compact and non empty set. We define the distance function from F_0 as

$$d_a^{\mathcal{M}, F_0}(\eta) = \inf_{\eta_0 \in F_0} d_a^{\mathcal{M}}(\eta_0, \eta), \tag{5.32}$$

where $d_a^{\mathcal{M}}(\eta_0, \eta)$ is the distance referred to admissible curves (see 5.21) in the cortical space $\mathcal{M}$.

Definition 5.5. Let $F_0, F_1 \subset \mathcal{M}$ be compact and non empty sets. We define the distance function between F_0, F_1 as

$$d_a^{\mathcal{M}}(F_0, F_1) = \inf_{\eta_1 \in F_1} d_a^{\mathcal{M}, F_0}(\eta_1), \tag{5.33}$$

where $d_a^{\mathcal{M}, F_0}$ is the distance function from F_0 defined in (5.32).

Remark 5.10. It is clear that if F_0 and F_1 respectively reduce to $\{\eta_0\}$ and $\{\eta_1\}$, then distance $d_a^{\mathcal{M}}(F_0, F_1)$ turns out to be $d_a^{\mathcal{M}}(\eta_0, \eta_1)$, for which we outline the existence of a minimum in Remark 5.9.

Definition 5.6. In the same conditions of Definition 5.5, we call admissible geodesic with extrema in the sets F_0 and F_1 the admissible curve $\gamma : [0,1] \to \mathcal{M}$ such that $\gamma(0) \in F_0$, $\gamma(1) \in F_1$ and which realizes the minimum in (5.33).

Due to the compactness of F_0 and F_1, it is immediate to prove the following

Proposition 5.10. *In the same conditions of Definition 5.5, there exists an admissible curve with extrema in F_0 and F_1 for which the minimum in (5.33) is attained*

Proof. We can find two sequences, respectively $(\eta_0)_n$ in F_0 and $(\eta_1)_n$ in F_1, such that $d_a^{\mathcal{M}}((\eta_0)_n, (\eta_1)_n)$ tends to $d_a^{\mathcal{M}}(F_0, F_1)$. Since $(\eta_0)_n$ and $(\eta_1)_n$ are bounded in a compact set, there exist two sub-successions $(\eta_0)_{n_j}$, $(\eta_1)_{n_j}$ in F_0 and F_1 which uniformly converges to η_0 and η_1, respectively. A geodesic between (η_0, η_1) exists, as recalled in Remark 5.10, and attains its minimum in (5.33). $\qquad\square$

5.2   Results

This section is dedicated to some experimental simulations for the solution of systems (5.6) and (5.17). Our goal is to provide a neurogeometrical interpretation of some task-dependent arm reaching movements using properties of geodesics established in 5.1.1.2, 5.1.2.1 and 5.1.2.2. As we have already observed, system (5.17) contains the solutions of system (5.6) as particular cases. In general, we always consider the most general possible system, but when considering movement gestures such as center-out, we can also reduce to the solutions of the system (5.6). For each of the cases we analyze, we will assume a fixed initial and final position, together with a null velocity at the beginning and at the end of the movement. First of all, in section 5.2.1, we recognized that solutions of (5.6) and (5.17) projected on the 2D plane coincide with the Flash and Hogan functional, introduced on the basis of experimental evidence (see [60] and [2, 117]). In order to fall in the assumptions adopted in Flash and Hogan model, we will impose to the equations for the 2D case (5.17) the constraint $\theta' = 0$. A reaching problem can indeed require a specific direction of grasping the target object, not necessarily coincident with the one at the beginning of the movement. For the last mentioned analysis, we will assume that the object can be reached with an arbitrary direction of the hand. Hence, from the set of geodesics connecting each couple of points, we will detect the minimimun path according to Definition 5.4. In section 5.2.2.2, we will consider an interval of possible directions also for the starting position. The mimimum path will be modelled as the geodesics between the sets representing the conditions at the extremes (this concept is formally expressed in Definition 5.6).

Numerically we solve the geodesics problem by the use of a shooting method (see [120] for further details), as follows.

(SHM) We want to solve Hamilton's equations (represented in (5.6) and (5.17)) with boundary conditions

$$(\gamma_i(0))_{i=1,\dots,k} = \alpha_0 \quad , \quad (\gamma_i(T))_{i=k+1,\dots,n} = \alpha_1. \tag{5.34}$$

We search for a vector $\beta_0 \in \mathbb{R}^{n-k}$, which is the vector of unknown initial conditions, such that, the γ_{β_0} is a solution of the hamiltonian system, (5.6) or (5.17), with initial conditions

$$(\gamma_{i,\beta_0}(0))_{i=1,\dots,n} = (\alpha_0, \beta_0) \quad \text{satisfies} \quad (\gamma_{i,\beta_0}(T))_{i=k+1,\dots,n} = \alpha_1. \tag{5.35}$$

Finding the initial condition β_0 is equivalent of finding the zeros of a function of the variable β_0

$$G(\beta_0) = (\gamma_{i,\beta_0}(T))_{i=k+1,\dots,n} - \alpha_1. \tag{5.36}$$

Remark 5.11. In the tests that follow, we consider an interval $[0, T]$ where we chose properly the extremum T so that the functions $s \mapsto h(s) = p_t + v(s) p_x + a(s) p_v(s)$ and $s \mapsto \psi(s) = v(s)(\cos(\theta(s)) p_x + \sin(\theta(s)) p_y) + a(s) p_v(s) + p_t$ together with their derivatives were not null. Therefore, we are truly reduced to analyze geodesics of the space in accordance to their definition of admissibility, as expressed in 5.1 and 5.3. Moreover, in this way the solution of the initial value problem is regular, without singularities. A different problem, which is the largest interval on which the solution are regular, has been investigated by U. Boscain et al. in [21] in the context of the SE(2) group.

5.2.1 Comparison with Flash and Hogan model

We analyze a task for which a final target is assumed to be achieved in a smooth way starting at zero speed and acceleration. Conditions at the extremes relative to velocity and acceleration match the ones analyzed by Flash and Hogan model. Hence, in the same notations of problem (SHM) and referring to geodesics equations (5.6), we assume

$$\alpha_0 = (t_0, x_0, v_0, a_0) = (0, x_0, 0, 0) \quad \text{and} \quad \alpha_1 = (t_1, x_1, v_1, a_1) = (1, x_1, 0, 0). \tag{5.37}$$

In the above conditions (5.37), an admissible curve exists (see Proposition 5.4) and has a bell-shaped speed profile (see Remark 5.4). In the left part of Figure 5.1, a representation concerning the trajectory, speed and acceleration profiles is shown.

Analogously for the two-dimensional case, by considering system (5.17) with constraint $\theta' = 0$ and boundary values

$$\tilde{\alpha}_0 = (t_0, x_0, y_0, \theta_0, v_0, a_0) = (0, 0, 0, \theta_0, 0, 0) \ , \ \tilde{\alpha}_1 = (t_1, x_1, y_1, v_1, a_1) = (1, x_1, y_1, 0, 0). \tag{5.38}$$
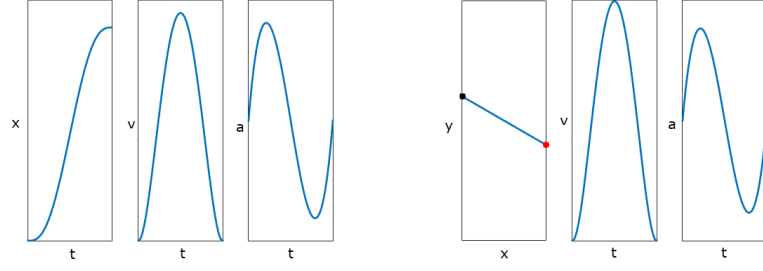
Figure 5.1: Left. Solution's projection of system (5.6) over the (t, x), (t, v), (t, a) planes, with extremes conditions (5.37). Right. Solution's projection of system (5.17) over the (x, y), (t, v), (t, a) planes, with extremes conditions (5.38) and movement direction $\theta = \frac{5}{6}\pi$. Red and black dots respectively denote initial and final hand's position.

we obviously find the same curves of the predicted paths and trajectories of Flash and Hogan model (see Figures 5.1 and 1.13 for a direct comparison).

Our setting allows to take into account even more general situations. For instance, we can consider a movement which does not require to start or end with a fixed acceleration. In the same conditions as before, we can replace $\tilde{\alpha}_0$ with $\bar{\alpha}_0 := (t_0, x_0, y_0, \theta_0, v_0, \bar{a}_0) = (0, 0, 0, \theta_0, 0, \bar{a}_0)$, where $\bar{a}_0$ is supposed to be varying over an interval $[a_0^1, a_0^2]$, so that it is possible to analyze a range of possible initial accelerations. Then, for any choices of $\bar{a}_0$, we solve through (SHM) problem (5.17) with initial value $\bar{\alpha}_0$ and final value $\tilde{\alpha}_1$ and, from the set of solutions, we select the geodesic with minimum length according to distance (5.32). In this context, the fiber of possible choices is assumed to be the one represented by the vector field X_3. In the same way, we could also think of replacing $\tilde{\alpha}_1$ with $\bar{\alpha}_1 := (t_1, x_1, y_1, v_1, \bar{a}_1) = (1, x_1, y_1, 0, \bar{a}_1)$, where $\bar{a}_1 \in [a_1^1, a_1^2]$. In Figure 5.2 a representation example of these situations is shown. The red-colored curve represents the geodesic from a point to a set as in Definition 5.4. In this case, it clearly appears how the geodesic results to be the curve which minimizes the rate of change of acceleration over the whole speed profile. This is due to the fact that the curvature over the path (x, y) is constantly null, therefore formula (5.22) measures the length of a path only by taking into account the the tangent over the velocity function $t \mapsto v(t)$.

5.2.2   Task-dependent boundary conditions

In this section, we generalize the class of center-out movements by exploring a set of reaching tasks which include a temporal change on the movement direction variable. We refer to subsections 5.1.2.1 and 5.1.2.2 for the formal arrangement of the problem.
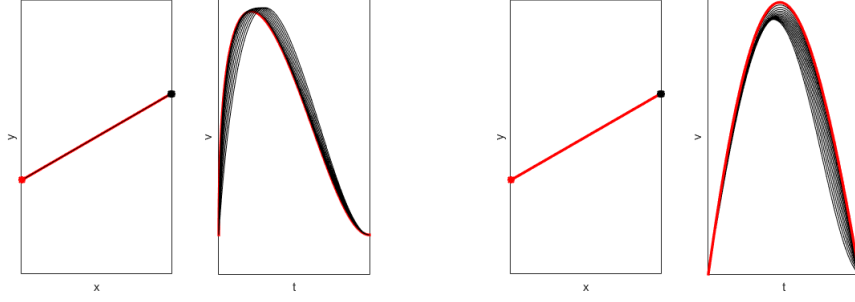
Figure 5.2: Solutions projections referred to system (5.17) with constraint $\theta' = 0$ over the (x, y) and (t, v) planes. The red-colored path represents the geodesic with minimum length according to (5.32). **Left.** Initial conditions are given by $\bar{\alpha}_0 = \left(0, 0, 0, \frac{\pi}{6}, 0, \bar{a}_0\right)$, where $\bar{a}_0 \in \left[\frac{3\pi}{10}, \frac{2\pi}{5}\right]$; final condition is assumed to be fixed at point $\tilde{\alpha}_1$, as in (5.38). **Right.** Initial condition is represented by $\tilde{\alpha}_0 = \left(0, 0, 0, \frac{\pi}{6}, 0, \frac{3\pi}{8}\right)$; final conditions are $\bar{\alpha}_1 = (1, x_1, y_1, 0, \bar{a}_1)$, where $\bar{a}_1$ varies over the interval $\left[-\frac{2\pi}{5}, -\frac{3\pi}{10}\right]$.

5.2.2.1   Reaching targets with prescribed directions

The simulations we present aim at computing reaching movements in which the final target is assumed to be grasped with a certain orientation θ_1. Moreover, an initial hand orientation θ_0 is assumed to be given. As we did in section 5.2.1, we set up (SHM) by considering system (5.17) and conditions at the extremes represented by

$$\hat{\alpha}_0 = (t_0, x_0, y_0, \theta_0, v_0, a_0) = (0, x_0, y_0, \theta_0, 0, a_0) \ , \ \hat{\alpha}_1 = (1, x_1, y_1, \theta_1, 0, a_1) . \qquad (5.39)$$

Proposition 5.9 ensures that an admissible curve connecting $\hat{\alpha}_0, \hat{\alpha}_1$ exists, therefore we look for the missing initial conditions $\hat{\beta}_0 = (p_{t_0}, p_{x_0}, p_{y_0}, p_{\theta_0}, p_{v_0}, p_{a_0})$ which solve the initial value problem (5.17) with $\left(\hat{\alpha}_0, \hat{\beta}_0\right)$ as initial datum and which satisfy equation (5.36). Some examples representing the paths and velocity profiles are shown in Figure 5.3.

Even in this context, we can discuss upon the choice of initial and final accelerations. For instance, if we want to grasp an object by slowly decelerating, we loose something in terms of optimal length. Indeed, if there is a choice in terms of final accelerations in order to reach a target, the minimum path will not be the one with the smoothest features in the (t, v) plane. As it is shown in Figure 5.2.2.1, if we compare those velocity profiles with increasingly steeping final accelerations, we see that those with a_1 more close to the $t-$axis provide smoother and longer curves. Referring to the (x, y) plane, the minimum path highlighted in red is associated with a euclidean length greater than the others. This is due to the high speeds reached which, given a fixed window of times, determine a longer path to be taken. The same reasoning also apply for an interval of choices referred to initial accelerations.
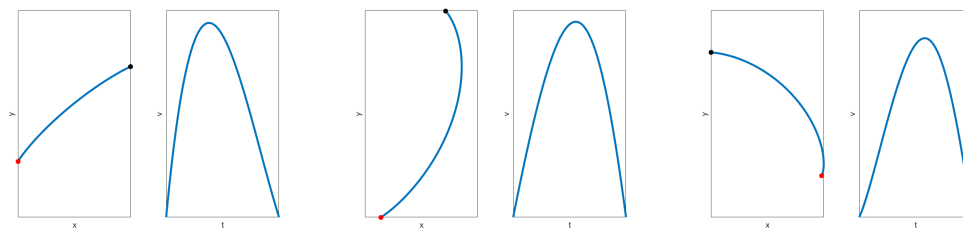
Figure 5.3: Reaching paths and speed profiles with boundary conditions 5.39. From left to right, the assumed extreme conditions for hand's orientations (θ_0, θ_1) are $\left(\frac{\pi}{3}, \frac{\pi}{8}\right)$, $\left(\frac{\pi}{6}, \frac{3\pi}{4}\right)$, $\left(\frac{\pi}{4}, \pi\right)$. Accelerations couple (a_0, a_1), from left to right, are $\left(\frac{\pi}{3}, -\frac{9\pi}{20}\right)$, $\left(\frac{\pi}{3}, -\frac{\pi}{4}\right)$, $\left(\frac{9\pi}{20}, -\frac{\pi}{3}\right)$.
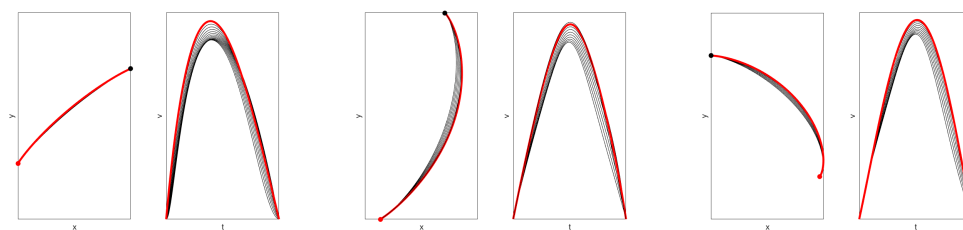

Figure 5.4: Reaching paths and speed profiles with boundary conditions as in Figure 5.3, with final acceleration varying in intervals $\left[-\frac{7\pi}{16}, -\frac{\pi}{3}\right]$, $\left[-\frac{\pi}{3}, -\frac{\pi}{6}\right]$, $\left[-\frac{3\pi}{8}, -\frac{\pi}{4}\right]$. The red-colored path represents the geodesic with minimum length according to (5.32).

5.2.2.2 Reaching targets with arbitrary directions

In this section, we will continue the analysis by focusing on the variation of parameters with respect to the movement direction. We point out that if we make varying both initial and final conditions it means that we are looking for a geodesic between sets, as well as if we fix an extremum and we study an interval of choice for the other boundary condition, we are searching for a geodesic from a set. We are formally considering Definitions 5.5 and 5.4 analyzed in section 5.1.2.2. In a first case, we consider the cognitive situation in which there exists a range of possible movement directions in order to achieve the final target. Hence, we assume the following conditions at the extremes

$$\hat{\alpha}_0 = (0, x_0, y_0, \theta_0, 0, a_0) \quad , \quad \hat{\alpha}_1^\theta = (1, x_1, y_1, \theta_1, 0, a_1) , \quad \theta_1 \in \left[\theta^a, \theta^b\right] . \quad (5.40)$$
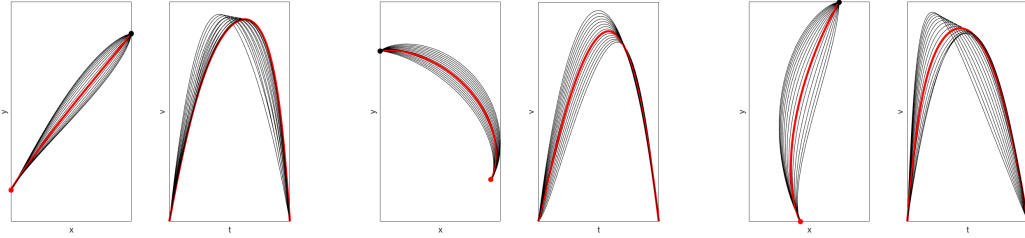

Figure 5.5: Reaching paths and speed profiles with boundary conditions 5.40. The initial movement directions θ_0 are, from left to right, $\frac{\pi}{3}, \frac{\pi}{4}, \frac{2\pi}{3}$, whereas the final ones θ_1 vary on intervals $\left[0, \frac{\pi}{2}\right], \left[\pi, \frac{5\pi}{4}\right], \left[0, \frac{\pi}{2}\right]$. The assumed extreme conditions for hand's accelerations (a_0, a_1) are $\left(\frac{3\pi}{8}, -\frac{3\pi}{8}\right)$, $\left(\frac{\pi}{3}, -\frac{3\pi}{8}\right)$, $\left(\frac{\pi}{3}, -\frac{3\pi}{8}\right)$. The red colored path is the geodesic with minimum length according to (5.32).

For any choice of $\theta_1 \in \left[\theta^a, \theta^b\right]$, we solve through (SHM) the Hamiltoniam system (5.17) and we find out the geodesic connecting each couple of points given by $\hat{\alpha}_0$ and $\hat{\alpha}_1^\theta$. Finally, we apply (5.32) in order to catch the minimum path from the interval $\left[\theta^a, \theta^b\right]$. Some examples are represented in Figure 5.5, where the geodesics found according to Definition 5.4 are red-colored. The geodesics account for a combination of minimum cost in terms of the spreading of curvature over the (x, y) and (t, v) planes, as it is inherited from Definition 5.22. As we can expect, if we assume a freedom of choice even for the initial movement directions, as in the following boundary conditions

$$\hat{\alpha}_0^\theta = (0, x_0, y_0, \theta_0, 0, a_0) \ , \ \hat{\alpha}_1^\theta = (1, x_1, y_1, \theta_1, 0, a_1) , \quad \theta_0 \in \left[\theta^a, \theta^b\right] , \ \theta_1 \in \left[\theta^c, \theta^d\right] , \quad (5.41)$$

the resulting geodesics turn out to be curves near to be straight paths which account for the minimum difference between the starting and ending directions, as it is shown in Figure 5.6.
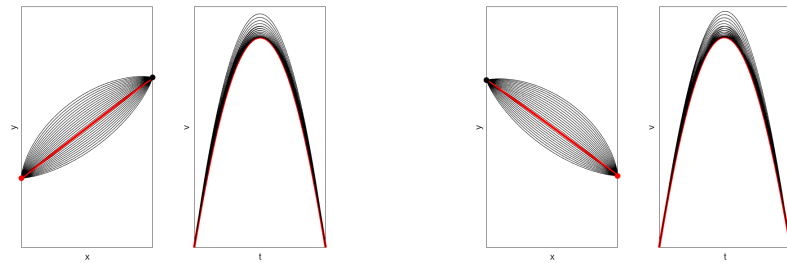
Figure 5.6: Reaching paths and speed profiles with boundary conditions (5.41). Initial and final hands movement directions θ_0, θ_1 are assumed to be varying in $\left[0, \frac{\pi}{2}\right], \left[-\frac{\pi}{12}, \frac{5\pi}{12}\right]$ and $\left[\frac{\pi}{2}, \pi\right], \left[\frac{11\pi}{18}, \frac{10\pi}{9}\right]$. Accelerations $(a_0, a_1) = \left(\frac{3\pi}{8}, -\frac{3\pi}{8}\right)$. The highlighted path is the minimum in length according to (5.33).

Conclusions

In this work, we proposed a geometric setting to explain the neural behaviour of the motor arm area M1. By getting inspiration from Georgopoulos neural models [70, 68], we provided a fiber bundle structure which is able to describe the hypercolumnar organization of the cortical area and the position-direction selectivity of motor cortical cells. On this structure, we extended the selective tuning of M1 neurons of kinematic variables by especially focusing on their temporal behaviour ([81], [38]). In fact, primary motor cells do not encode single "static" movement parameters, but entire movement trajectories that evolve over time, expressed as fragments of movement, as attested by the experimental data of Hatsopoulos et al. [81] and Churchland et al. [38]. This led to consider a higher dimensional geometric structure whose elements represent movement fragments: these are described as integral curves of the geometric setting with sub-Riemannian metrics. The distance we defined in this space is used to characterize a kernel which models the cortical connectivity between selective kinematic variables of the neurons. Such connectivity kernel allowed to recover a set of hand movement trajectories by means of a spectral clustering algorithm. The eigenvectors found from the affinity matrix decompose movement trajectories into movement fragments of acceleration or deceleration with a specific plane direction. These trajectories are well in accordance with the motor patterns measured in Kadmon Harpaz et al. [95] and Hatsopoulos et al. [81]. Therefore, in this work, we showed how it is possible to obtain these same trajectory patterns through a connectivity kernel with sub-Riemannian distance. Hence, we provided a purely kinematic classification that identifies coherent patterns of movement fragments. However, for the purpose of neural modelling, it must be taken into account that each neuron is active for a certain time window and that its response is temporally ([81]) and spatially ([95]) invariant. In this thesis, we bypass this problem by adding a clustering step to group together sub-trajectories having similar trend in movement direction and acceleration variables. This procedure is very simple and performs correct grouping in terms of movement fragments, nonetheless this mechanism has no neural foundation. In perspective, to model a neural structure, it should be involved the complete space of trajectory fragments, also by taking into account the time windows for which each neuron is selective. In this way, the grouping algorithm should be obtained through a distance realized in terms of a space of trajectory fragments.

In a second part of the work, we exploited the neurogeometrical model of functional architecture of M1 to propose a model of arm reaching movements. The work took Flash and Hogan's phenomenological model as a point of reference. Their model is based on the selection of a cost function whose minima are found to be in good agreement with the simplest and smoothest motion trajectories. In this thesis, we recovered the minimizing trajectories found by Flash and Hogan as geodesics in an Engel-type manifold. Specifically we considered only a specific class of curves, called admissible, which are lifting of mono-dimensional paths. For these curves, we provided a connectivity property and the existence of length minimizers. Admissible geodesics represent our model for center-out type movements. We then extended the previous model by considering admissible curves into a new non-nilpotent subriemannian structure. In this second part, we proved the same results of connectivity property and questioned the existence of abnormal minimizers, showing that admissible geodesics are regular, hence normal. Finally, we presented a qualitative analysis on how admissible geodesics allow to recover a broader variety of reaching tasks.

Our model, both for the predominantly neural and phenomenological parts, gradually leads to a shift from a space mainly described by kinematic points to a space of movement trajectories. In the future, we believe it would be interesting to expand the model to a space of movement trajectories, where admissible distances and variations can be defined. This could be of neural support, as it could better explain the data presented in Hatsopoulos et al. [81], Churchland et al. [38], Hocherman et al. [82], Kadmon Harpaz et al. [95] that strongly support the role of movement trajectories in motor encoding.

Bibliography

[1] Samaneh Abbasi-Sureshjani, Marta Favali, Giovanna Citti, Alessandro Sarti, and Bart M ter Haar Romeny. Curvature integration in a 5d kernel for extracting vessel connections in retinal images. IEEE Transactions on Image Processing, 27(2):606–621, 2017.

[2] William Abend, Emilio Bizzi, and Pietro Morasso. Human arm trajectory formation. Brain: a journal of neurology, 105(Pt 2):331–348, 1982.

[3] Tyson N Aflalo and Michael SA Graziano. Partial tuning of motor cortex neurons to final posture in a free-moving paradigm. Proceedings of the National Academy of Sciences, 103(8):2909–2914, 2006.

[4] Tyson N Aflalo and Michael SA Graziano. Possible origins of the complex topographic organization of motor cortex: reduction of a multidimensional space onto a two-dimensional array. Journal of Neuroscience, 26(23):6288–6297, 2006.

[5] Andrei Agrachev, Davide Barilari, and Ugo Boscain. A comprehensive introduction to sub-Riemannian geometry, volume 181. Cambridge University Press, 2019.

[6] Robert Ajemian, Daniel Bullock, and Stephen Grossberg. A model of movement coordinates in the motor cortex: posture-dependent changes in the gain and direction of single cell tuning curves. Cerebral Cortex, 11(12):1124–1135, 2001.

[7] Bagrat Amirikian and Apostolos P Georgopoulos. Modular organization of directionally tuned cells in the motor cortex: is there a short-range order? Proceedings of the National Academy of Sciences, 100(21):12474–12479, 2003.

[8] Andrei A Ardentov and Yurii L Sachkov. Extremal trajectories in a nilpotent sub-riemannian problem on the engel group. Sbornik: Mathematics, 202(11):1593, 2011.

[9] Gustavo Arechavaleta, Jean-Paul Laumond, Halim Hicheur, and Alain Berthoz. Optimizing principles underlying the shape of trajectories in goal oriented locomotion for humans. In 2006 6th IEEE-RAS International Conference on Humanoid Robots, pages 131–136. IEEE, 2006.

[10] Gustavo Arechavaleta, Jean-Paul Laumond, Halim Hicheur, and Alain Berthoz. An optimality principle governing human walking. IEEE Transactions on Robotics, 24(1):5–14, 2008.

[11] James Ashe and Apostolos P Georgopoulos. Movement parameters and neural activity in motor cortex and area 5. Cerebral cortex, 4(6):590–600, 1994.

[12] Térence Bayen, Yacine Chitour, Frédéric Jean, and Paolo Mason. Asymptotic analysis of an optimal control problem connected to the human locomotion. In Proceedings of the 48h IEEE Conference on Decision and Control (CDC) held jointly with 2009 28th Chinese Control Conference, pages 2248–2253. IEEE, 2009.

[13] Richard Beals, Bernard Gaveau, and Peter C Greiner. Hamilton–jacobi theory and the heat kernel on heisenberg groups. Journal de mathématiques pures et appliquées, 79(7):633–689, 2000.

[14] Mark Bear, Barry Connors, and Michael A Paradiso. Neuroscience: Exploring the Brain, Enhanced Edition: Exploring the Brain. Jones & Bartlett Learning, 2020.

[15] Mikhail Belkin and Partha Niyogi. Laplacian eigenmaps for dimensionality reduction and data representation. Neural computation, 15(6):1373–1396, 2003.

[16] Bastien Berret, Christian Darlot, Frédéric Jean, Thierry Pozzo, Charalambos Papaxanthis, and Jean Paul Gauthier. The inactivation principle: mathematical solutions minimizing the absolute work and biological implications for the planning of arm movements. PLoS computational biology, 4(10):e1000194, 2008.

[17] Ivan Beschastnyi and Alexandr Medvedev. Left-invariant sub-riemannian engel structures: abnormal geodesics and integrability. SIAM Journal on Control and Optimization, 56(5):3524–3537, 2018.

[18] Armin Biess, Dario G Liebermann, and Tamar Flash. A computational model for redundant human three-dimensional pointing movements: integration of independent spatial and temporal motor plans simplifies movement dynamics. Journal of Neuroscience, 27(48):13045–13064, 2007.

[19] Bernard Bonnard and Emmanuel Trélat. On the role of abnormal minimizers in sub-riemannian geometry. In Annales de la Faculté des sciences de Toulouse: Mathématiques, volume 10, pages 405–491, 2001.

[20] Ugo Boscain, Grégoire Charlot, and Francesco Rossi. Existence of planar curves minimizing length and curvature. Proceedings of the Steklov institute of mathematics, 270(1):43–56, 2010.

[21] Ugo Boscain, Remco Duits, Francesco Rossi, and Yuri Sachkov. Optimal control for reconstruction of curves without cusps. In 2012 IEEE 51st IEEE Conference on Decision and Control (CDC), pages 7679–7684. IEEE, 2012.

[22] Ugo Boscain, Remco Duits, Francesco Rossi, and Yuri Sachkov. Curve cuspless reconstruction via sub-riemannian geometry∗∗∗. ESAIM: Control, Optimisation and Calculus of Variations, 20(3):748–770, 2014.

[23] William H Bosking, Ying Zhang, Brett Schofield, and David Fitzpatrick. Orientation selectivity and the arrangement of horizontal connections in tree shrew striate cortex. Journal of neuroscience, 17(6):2112–2127, 1997.

[24] Alejandro Bravo-Doddoli. Higher elastica: Geodesics in the jet space. arXiv preprint arXiv:2003.08022, 2020.

[25] Alejandro Bravo-Doddoli and Richard Montgomery. Geodesics in jet space. Regular and Chaotic Dynamics, 27(2):151–182, 2022.

[26] Paul C Bressloff and Jack D Cowan. The visual cortex as a crystal. Physica D: Nonlinear Phenomena, 173(3-4):226–258, 2002.

[27] Paul C Bressloff and Jack D Cowan. The functional geometry of local and horizontal connections in a model of v1. Journal of Physiology-Paris, 97(2-3):221–236, 2003.

[28] Paul C Bressloff, Jack D Cowan, Martin Golubitsky, Peter J Thomas, and Matthew C Wiener. What geometric visual hallucinations tell us about the visual cortex. Neural computation, 14(3):473–491, 2002.

[29] Robert L Bryant and Lucas Hsu. Rigidity of integral curves of rank 2 distributions. Inventiones mathematicae, 114(1):435–461, 1993.

[30] Steve Butler, Fan Chung, et al. Spectral graph theory. Handbook of linear algebra, page 47, 2006.

[31] Roberto Caminiti, Paul B Johnson, and Antonio Urbano. Making arm movements within different parts of space: dynamic aspects in the primate motor cortex. Journal of Neuroscience, 10(7):2039–2058, 1990.

[32] Roger Carpenter and Benjamin Reddi. Neurophysiology: a conceptual approach. CRC Press, 2012.

[33] Yacine Chitour, Francesca Chittaro, Frédéric Jean, and Paolo Mason. Analysis of optimal control models for the human locomotion. In 49th IEEE Conference on Decision and Control (CDC), pages 3415–3420. IEEE, 2010.

[34] Yacine Chitour, Frédéric Jean, and Paolo Mason. Optimal control models of goal-oriented human locomotion. *SIAM Journal on Control and Optimization*, 50(1):147–170, 2012.

[35] Yacine Chitour, Frédéric Jean, and Emmanuel Trélat. Genericity results for singular curves. *Journal of differential Geometry*, 73(1):45–73, 2006.

[36] Wei-Liang Chow. Über systeme von linearen partiellen differential-gleichungen erster ordnung. In *The Collected Papers Of Wei-Liang Chow*, pages 47–54. World Scientific, 2002.

[37] Fan RK Chung. *Spectral graph theory*, volume 92. American Mathematical Soc., 1997.

[38] Mark M Churchland and Krishna V Shenoy. Temporal complexity and heterogeneity of single-neuron activity in premotor and motor cortex. *Journal of neurophysiology*, 97(6):4235–4257, 2007.

[39] Giovanna Citti, Gianmarco Giovannardi, and Manuel Ritoré. Variational formulas for curves of fixed degree. *arXiv preprint arXiv:1902.04015*, 2019.

[40] Giovanna Citti, Gianmarco Giovannardi, and Manuel Ritoré. Variational formulas for curves of fixed degree. *Advances in Differential Equations*, 27(5/6):333–384, 2022.

[41] Giovanna Citti and Alessandro Sarti. A cortical based model of perceptual completion in the roto-translation space. *Journal of Mathematical Imaging and Vision*, 24(3):307–326, 2006.

[42] Giovanna Citti and Alessandro Sarti. *Neuromathematics of vision*, volume 32. Springer, 2014.

[43] Giacomo Cocci. Spatio-temporal models of the functional architecture of the visual cortex. 2014.

[44] Giacomo Cocci, Davide Barbieri, Giovanna Citti, and Alessandro Sarti. Cortical spatiotemporal dimensionality reduction for visual grouping. *Neural computation*, 27(6):1252–1293, 2015.

[45] Ronald R Coifman and Stéphane Lafon. Diffusion maps. *Applied and computational harmonic analysis*, 21(1):5–30, 2006.

[46] John G Daugman. Uncertainty relation for resolution in space, spatial frequency, and orientation optimized by two-dimensional visual cortical filters. *JOSA A*, 2(7):1160–1169, 1985.

[47] Gregory C DeAngelis, Izumi Ohzawa, and Ralph D Freeman. Receptive-field dynamics in the central visual pathways. Trends in neurosciences, 18(10):451–458, 1995.

[48] Gregory C DeAngelis, Izumi Ohzawa, and RD Freeman. Spatiotemporal organization of simple-cell receptive fields in the cat's striate cortex. i. general characteristics and postnatal development. Journal of neurophysiology, 69(4):1091–1117, 1993.

[49] S Diomedi, FE Vaccari, C Galletti, K Hadjidimitrakis, and P Fattori. Motor-like neural dynamics in two parietal areas during arm reaching. Progress in Neurobiology, 205:102116, 2021.

[50] Remco Duits, Ugo Boscain, Francesco Rossi, and Yuri Sachkov. Association fields via cuspless sub-riemannian geodesics in se (2). Journal of mathematical imaging and vision, 49(2):384–417, 2014.

[51] Remco Duits, Arpan Ghosh, Tom Dela Haije, and Yuri Sachkov. Cuspless sub-riemannian geodesics within the euclidean motion group se (d). In Neuromathematics of Vision, pages 173–215. Springer, 2014.

[52] Michael N Economo, Sarada Viswanathan, Bosiljka Tasic, Erhan Bas, Johan Winnubst, Vilas Menon, Lucas T Graybuck, Thuc Nghi Nguyen, Kimberly A Smith, Zizhen Yao, et al. Distinct descending motor cortex pathways and their roles in movement. Nature, 563(7729):79–84, 2018.

[53] G Bard Ermentrout and JD Cowan. Large scale spatially organized activity in neural nets. SIAM Journal on Applied Mathematics, 38(1):1–21, 1980.

[54] Eo Vo Evarts. Representation of movements and muscles by pyramidal tract neurons of the precentral motor cortex, 1967.

[55] Olivier Faugeras, Romain Veltz, and François Grimbert. Persistent neural states: stationary localized activity patterns in nonlinear continuous n-population, q-dimensional neural networks. Neural computation, 21(1):147–187, 2009.

[56] Marta Favali, Giovanna Citti, and Alessandro Sarti. Local and global gestalt laws: A neurally based spectral approach. Neural computation, 29(2):394–422, 2017.

[57] Tamar Flash and Amir A Handzel. Affine differential geometry analysis of human arm movements. Biological cybernetics, 96(6):577–601, 2007.

[58] Tamar Flash, Ealan Henis, Rivka Inzelberg, and AD Korczyn. Timing and sequencing of human arm trajectories: normal and abnormal motor behaviour. Human movement science, 11(1-2):83–100, 1992.

[59] Tamar Flash and Binyamin Hochner. Motor primitives in vertebrates and invertebrates. Current opinion in neurobiology, 15(6):660–666, 2005.

[60] Tamar Flash and Neville Hogan. The coordination of arm movements: an experimentally confirmed mathematical model. Journal of neuroscience, 5(7):1688–1703, 1985.

[61] Tamar Flash and Terrence J Sejnowski. Computational approaches to motor control. Current opinion in neurobiology, 11(6):655–662, 2001.

[62] Benedetta Franceschiello, Alexey Mashtakov, Giovanna Citti, and Alessandro Sarti. Geometrical optical illusion via sub-riemannian geodesics in the roto-translation group. Differential Geometry and its Applications, 65:55–77, 2019.

[63] AP Georgopoulos. The representation of movement direction in the motor cotex: Single cell and population studies. Dynamic aspects of neocortical function, pages 501–524, 1984.

[64] AP Georgopoulos, R Caminiti, and JF Kalaska. Static spatial effects in motor cortex and area 5: quantitative relations in a two-dimensional space. Experimental Brain Research, 54(3):446–454, 1984.

[65] AP Georgopoulos, JF Kalaska, R Caminiti, and JT Massey. Interruption of motor cortical discharge subserving aimed arm movements. Experimental Brain Research, 49(3):327–340, 1983.

[66] Apostolos P Georgopoulos. Neural integration of movement: role of motor cortex in reaching. The FASEB Journal, 2(13):2849–2857, 1988.

[67] Apostolos P Georgopoulos. Spatial coding of visually guided arm movements in primate motor cortex. Canadian journal of physiology and pharmacology, 66(4):518–526, 1988.

[68] Apostolos P Georgopoulos. Columnar organization of the motor cortex: direction of movement. In Recent Advances on the Modular Organization of the Cortex, pages 123–141. Springer, 2015.

[69] Apostolos P Georgopoulos, James Ashe, Nikolaos Smyrnis, and Masato Taira. The motor cortex and the coding of force. Science, 256(5064):1692–1695, 1992.

[70] Apostolos P Georgopoulos, John F Kalaska, Roberto Caminiti, and Joe T Massey. On the relations between the direction of two-dimensional arm movements and cell discharge in primate motor cortex. Journal of Neuroscience, 2(11):1527–1537, 1982.

[71] Apostolos P Georgopoulos, Ronald E Kettner, and Andrew B Schwartz. Primate motor cortex and free arm movements to visual targets in three-dimensional space. ii. coding of the direction of movement by a neuronal population. Journal of Neuroscience, 8(8):2928–2937, 1988.

[72] Apostolos P Georgopoulos, Hugo Merchant, Thomas Naselaris, and Bagrat Amirikian. Mapping of the preferred direction in the motor cortex. Proceedings of the National Academy of Sciences, 104(26):11068–11072, 2007.

[73] Apostolos P Georgopoulos, Andrew B Schwartz, and Ronald E Kettner. Neuronal population coding of movement direction. Science, 233(4771):1416–1419, 1986.

[74] Gianmarco Giovannardi et al. Variations for submanifolds of fixed degree. 2020.

[75] Michael Graziano. The intelligent movement machine: An ethological perspective on the primate motor system. Oxford University Press, 2008.

[76] Michael SA Graziano and Tyson N Aflalo. Mapping behavioral repertoire onto the cortex. Neuron, 56(2):239–251, 2007.

[77] Michael SA Graziano, Charlotte SR Taylor, Tirin Moore, and Dylan F Cooke. The cortical control of movement revisited. Neuron, 36(3):349–362, 2002.

[78] Michael SA Graziano, Charlotte SR Taylor, Tirin Moore, and Dylan F Cooke. The cortical control of movement revisited. Neuron, 36(3):349–362, 2002.

[79] Duane E Haines. Neuroanatomy: an atlas of structures, sections, and systems, volume 153. Lippincott Williams & Wilkins, 2004.

[80] Thomas C Harrison and Timothy H Murphy. Towards a circuit mechanism for movement tuning in motor cortex. Frontiers in neural circuits, 6:127, 2013.

[81] Nicholas G Hatsopoulos, Qingqing Xu, and Yali Amit. Encoding of movement fragments in the motor cortex. Journal of Neuroscience, 27(19):5105–5114, 2007.

[82] S Hocherman and SP Wise. Effects of hand movement path on motor cortical activity in awake, behaving rhesus monkeys. Experimental brain research, 83(2):285–302, 1991.

[83] William C Hoffman. Higher visual perception as prolongation of the basic lie transformation group. Mathematical Biosciences, 6:437–471, 1970.

[84] Neville Hogan. An organizing principle for a class of voluntary movements. Journal of neuroscience, 4(11):2745–2754, 1984.

[85] RN Holdefer and LE Miller. Primary motor cortical neurons encode functional muscle synergies. Experimental Brain Research, 146(2):233–243, 2002.

[86] Lucas Hsu. Calculus of variations via the griffiths formalism. J. Differential Geom., 36(3):551–589, 1992.

[87] David H Hubel. Eye, brain, and vision. Scientific American Library/Scientific American Books, 1995.

[88] David H Hubel and TN Wiesel. Shape and arrangement of columns in cat's striate cortex. The Journal of physiology, 165(3):559–568, 1963.

[89] David H Hubel and Torsten N Wiesel. Receptive fields, binocular interaction and functional architecture in the cat's visual cortex. The Journal of physiology, 160(1):106–154, 1962.

[90] DH HubelandT and N Wiesel. Functionalarchitectureofmacaquemonkeyvisual cortex. Proc. Roy. Soc. Lond. B, 198(1-59), 1977.

[91] Frédéric JEAn. Optimal control models of the goal-oriented human locomotion. In Talk given at the "Workshop on Nonlinear Control and Singularities", Porquerolles, France, pages 24–28, 2010.

[92] Frédéric Jean. Control of nonholonomic systems: from sub-Riemannian geometry to motion planning. Springer, 2014.

[93] Robert Jones. The evaluation and grading of placement performance. Teaching Public Administration, 7(1):31–43, 1987.

[94] Jürgen Jost and Jeurgen Jost. Riemannian geometry and geometric analysis, volume 42005. Springer, 2008.

[95] Naama Kadmon Harpaz, David Ungarish, Nicholas G Hatsopoulos, and Tamar Flash. Movement decomposition in the primary motor cortex. Cerebral cortex, 29(4):1619–1633, 2019.

[96] John F Kalaska. From intention to action: motor cortex and the control of reaching movements. Progress in Motor Control, pages 139–178, 2009.

[97] Eric R Kandel, James H Schwartz, Thomas M Jessell, Steven Siegelbaum, A James Hudspeth, Sarah Mack, et al. Principles of neural science, volume 4. McGraw-hill New York, 2000.

[98] Ravi Kannan, Santosh Vempala, and Adrian Vetta. On clusterings: Good, bad and spectral. Journal of the ACM (JACM), 51(3):497–515, 2004.

[99] Maeda Kawato, Y Maeda, Y Uno, and R Suzuki. Trajectory formation of arm movement by cascade neural network model based on minimum torque-change criterion. Biological cybernetics, 62(4):275–288, 1990.

[100] Ronald E Kettner, Andrew B Schwartz, and Apostolos P Georgopoulos. Primate motor cortex and free arm movements to visual targets in three-dimensional space. iii. positional gradients and population coding of movement direction from various movement origins. Journal of Neuroscience, 8(8):2938–2947, 1988.

[101] Kurt Koffka. Principles of Gestalt psychology. Routledge, 2013.

[102] K Krishna and M Narasimha Murty. Genetic k-means algorithm. IEEE Transactions on Systems, Man, and Cybernetics, Part B (Cybernetics), 29(3):433–439, 1999.

[103] Stephane Lafon and Ann B Lee. Diffusion maps and coarse-graining: A unified framework for dimensionality reduction, graph partitioning, and data set parameterization. IEEE transactions on pattern analysis and machine intelligence, 28(9):1393–1403, 2006.

[104] Enrico Le Donne. Lecture notes on sub-riemannian geometry. preprint, 2010.

[105] John Lee. Introduction to topological manifolds, volume 202. Springer Science & Business Media, 2010.

[106] John M Lee. Smooth manifolds. In Introduction to smooth manifolds, pages 1–31. Springer, 2013.

[107] Tai Sing Lee. Image representation using 2d gabor wavelets. IEEE Transactions on pattern analysis and machine intelligence, 18(10):959–971, 1996.

[108] Wensheng Liu and HJ Sussmann. Shortest paths for sub-riemannian metrics on rank-two distributions. Mem. Amer. Math. Soc, 118(564):1–104, 1996.

[109] Marina Meilă and Jianbo Shi. A random walks view of spectral segmentation. In International Workshop on Artificial Intelligence and Statistics, pages 203–208. PMLR, 2001.

[110] Igor Moiseev and Yuri L Sachkov. Maxwell strata in sub-riemannian problem on the group of motions of a plane. ESAIM: Control, Optimisation and Calculus of Variations, 16(2):380–399, 2010.

[111] Richard Montgomery. Abnormal minimizers. Siam Journal on control and optimization, 32(6):1605–1620, 1994.

[112] Richard Montgomery. Singular extremals on lie groups. Mathematics of Control, Signals and Systems, 7(3):217–234, 1994.

[113] Richard Montgomery. Engel deformations and contact structures. Translations of the American Mathematical Society-Series 2, 196:103–118, 1999.

[114] Richard Montgomery. A Tour of Subriemannian Geometries, Their Geodesics and Applications. Mathematical Surveys and Monographs 91. American Mathematical Society, 2006.

[115] Roberto Monti. A family of nonminimizing abnormal curves. Annali di Matematica Pura ed Applicata (1923-), 193(6):1577–1593, 2014.

[116] Daniel W Moran and Andrew B Schwartz. Motor cortical representation of speed and direction during reaching. Journal of neurophysiology, 82(5):2676–2692, 1999.

[117] Pietro Morasso. Spatial control of arm movements. Experimental brain research, 42(2):223–227, 1981.

[118] Vernon B Mountcastle. The columnar organization of the neocortex. Brain: a journal of neurology, 120(4):701–722, 1997.

[119] Ferdinando A Mussa-Ivaldi and Sara A Solla. Neural primitives for motion control. IEEE Journal of Oceanic Engineering, 29(3):640–650, 2004.

[120] Tsung Yen Na. Computational methods in engineering boundary value problems. Academic press, 1980.

[121] Alexander Nagel, Elias M Stein, and Stephen Wainger. Balls and metrics defined by vector fields i: Basic properties. Acta Mathematica, 155:103–147, 1985.

[122] Thomas Naselaris, Hugo Merchant, Bagrat Amirikian, and Apostolos P Georgopoulos. Large-scale organization of preferred directions in the motor cortex. ii. analysis of local distributions. Journal of neurophysiology, 96(6):3237–3247, 2006.

[123] Andrew Ng, Michael Jordan, and Yair Weiss. On spectral clustering: Analysis and an algorithm. Advances in neural information processing systems, 14, 2001.

[124] Mohsen Omrani, Matthew T Kaufman, Nicholas G Hatsopoulos, and Paul D Cheney. Perspectives on classical controversies about the motor cortex. Journal of neurophysiology, 118(3):1828–1848, 2017.

[125] Liam Paninski, Matthew R Fellows, Nicholas G Hatsopoulos, and John P Donoghue. Spatiotemporal tuning of motor cortical neurons for hand position and velocity. Journal of neurophysiology, 91(1):515–532, 2004.

[126] Pietro Perona and William Freeman. A factorization approach to grouping. In European Conference on Computer Vision, pages 655–670. Springer, 1998.

[127] Jean Petitot. The neurogeometry of pinwheels as a sub-riemannian contact structure. Journal of Physiology-Paris, 97(2-3):265–309, 2003.

[128] Jean Petitot. Neurogéométrie de la vision: modeles mathematiques et physiques des architectures fonctionnelles. Editions Ecole Polytechnique, 2008.

[129] Jean Petitot. Neurogéométrie de la vision. Springer, 2017.

[130] Jean Petitot, Petitot, and Hiripi. Elements of neurogeometry. Springer, 2017.

[131] Jean Petitot and Yannick Tondut. Vers une neurogéométrie. fibrations corticales, structures de contact et contours subjectifs modaux. Mathématiques et sciences humaines, 145:5–101, 1999.

[132] Lev Semenovich Pontryagin. Mathematical theory of optimal processes. CRC press, 1987.

[133] Jacob Reimer and Nicholas G Hatsopoulos. The problem of parametric neural coding in the motor system. In Progress in motor control, pages 243–259. Springer, 2009.

[134] Sam T Roweis and Lawrence K Saul. Nonlinear dimensionality reduction by locally linear embedding. science, 290(5500):2323–2326, 2000.

[135] Alessandro Sarti and Giovanna Citti. The constitution of visual perceptual units in the functional architecture of v1. Journal of computational neuroscience, 38(2):285–300, 2015.

[136] Andrew B Schwartz. Useful signals from motor cortex. The Journal of physiology, 579(3):581–601, 2007.

[137] Andrew B Schwartz, Ronald E Kettner, and Apostolos P Georgopoulos. Primate motor cortex and free arm movements to visual targets in three-dimensional space. i. relations between single cell discharge and direction of movement. Journal of Neuroscience, 8(8):2913–2927, 1988.

[138] Stephen H Scott. Optimal feedback control and the neural basis of volitional motor control. Nature Reviews Neuroscience, 5(7):532–545, 2004.

[139] Stephen H Scott. 6 conceptual frameworks for interpreting motor cortical function: New insights from multiple-joint paradigm. 2005.

[140] Stephen H Scott and John F Kalaska. Reaching movements with similar hand paths but different arm orientations. i. activity of individual cells in motor cortex. Journal of neurophysiology, 77(2):826–852, 1997.

[141] Lauren E Sergio and John F Kalaska. Changes in the temporal pattern of primary motor cortex activity in a directional isometric force versus limb movement task. Journal of neurophysiology, 80(3):1577–1583, 1998.

[142] Jianbo Shi and Jitendra Malik. Normalized cuts and image segmentation. IEEE Transactions on pattern analysis and machine intelligence, 22(8):888–905, 2000.

[143] Eran Stark, Rotem Drori, and Moshe Abeles. Motor cortical activity related to movement kinematics exhibits local spatial organization. Cortex, 45(3):418–431, 2009.

[144] Héctor J Sussmann. A cornucopia of four-dimensional abnormal sub-riemannian minimizers. In Sub-Riemannian Geometry, pages 341–364. Springer, 1996.

[145] Hirokazu Tanaka and Terrence J Sejnowski. Motor adaptation and generalization of reaching movements using motor primitives based on spatial coordinates. Journal of neurophysiology, 113(4):1217–1233, 2015.

[146] Wondimu W Teka, Khaldoun C Hamade, William H Barnett, Taegyo Kim, Sergey N Markin, Ilya A Rybak, and Yaroslav I Molkov. From the motor cortex to the movement and back again. PloS one, 12(6):e0179288, 2017.

[147] Emanuel Todorov. Direct cortical control of muscle activation in voluntary arm movements: a model. Nature neuroscience, 3(4):391–398, 2000.

[148] Emanuel Todorov. Optimal control theory. Bayesian brain: probabilistic approaches to neural coding, pages 268–298, 2006.

[149] Emanuel Todorov and Michael I Jordan. Optimal feedback control as a theory of motor coordination. Nature neuroscience, 5(11):1226–1235, 2002.

[150] Wilson Truccolo, Gerhard M Friehs, John P Donoghue, and Leigh R Hochberg. Primary motor cortex tuning to intended movement kinematics in humans with tetraplegia. Journal of Neuroscience, 28(5):1163–1178, 2008.

[151] Loring W Tu. Manifolds. In An Introduction to Manifolds, pages 47–83. Springer, 2011.

[152] Yoji Uno, Mitsuo Kawato, and Rika Suzuki. Formation and control of optimal trajectory in human multijoint arm movement. Biological cybernetics, 61(2):89–101, 1989.

[153] Ulrike Von Luxburg. A tutorial on spectral clustering. Statistics and computing, 17(4):395–416, 2007.

[154] Wei Wang, Sherwin S Chan, Dustin A Heldman, and Daniel W Moran. Motor cortical representation of position and velocity during reaching. Journal of neurophysiology, 97(6):4258–4270, 2007.

[155] Yair Weiss. Segmentation using eigenvectors: a unifying view. In Proceedings of the seventh IEEE international conference on computer vision, volume 2, pages 975–982. IEEE, 1999.

[156] Hugh R Wilson and Jack D Cowan. A mathematical theory of the functional dynamics of cortical and thalamic nervous tissue. Kybernetik, 13(2):55–80, 1973.

[157] S.P. Wise. Motor cortex. In Neil J. Smelser and Paul B. Baltes, editors, International Encyclopedia of the Social & Behavioral Sciences, pages 10137–10140. Pergamon, Oxford, 2001.